UNIVERSITY OF OKLAHOMA

GRADUATE COLLEGE

# ANALYSIS OF FAULTING AND EARTHQUAKE PROCESSES: FROM LABORATORY EXPERIMENTS TO CRUSTAL-SCALE INVESTIGATIONS

A DISSERTATION

SUBMITTED TO THE GRADUATE FACULTY

in partial fulfillment of the requirements for the

Degree of

DOCTOR OF PHILOSOPHY

By

JEFFERSON CASTILLO CHANG
Norman, Oklahoma
2017

# ANALYSIS OF FAULTING AND EARTHQUAKE PROCESSES: FROM LABORATORY EXPERIMENTS TO CRUSTAL-SCALE INVESTIGATIONS

A DISSERTATION APPROVED FOR THE
CONOCOPHILLIPS SCHOOL OF GEOLOGY AND GEOPHYSICS

BY

Dr. Kurt J. Marfurt, Co-Chair

Dr. Ze'ev Reches, Co-Chair

Dr. G. Randy Keller, Co-Chair

Dr. R. Douglas Elmore

Dr. Shannon Dulin

Dr. Deepak Devegowda

To my mother, Helen, for fanning the flames of my childhood curiosity.

To my wife, Julie, for being my unwavering pillar of strength throughout the years.

To my children, Arizona and November, for inspiring me to better myself every day.

# Acknowledgements

I would like to thank my research advisors, Dr. Ze'ev Reches and Dr. Randy Keller, for their time, guidance, and support. You both have shown me that the details in observations add up to the scientific big picture. I am forever in debt for your patience with me.

I would also like to thank Dr. Kurt Marfurt for making sure my writing was coherent and focused.

The laboratory research was supported by NSF Geosciences awards 0732715 and 1045414, and NEHRP2011 award G11AP20008. The China project was supported by SinoProbe and China NSF grants 40830316, and US NSF PIRE grant 0730154. Part of the Oklahoma seismicity project was funded by NSF RAPID grants (1636715, 1664265, and 1664329) and RPSEA project 12122-91.

## Table of Contents

Acknowledgements iv

List of Tables x

List of Figures xi

Abstract xiv

Chapter 1: Introduction 1

- Summary 1
- Dissertation Organization 1
  - Chapter 2: Earthquake-Like Slip Events 2
  - Chapter 3: Seismic Tomography of Tangshan, China 3
  - Chapter 4: Seismological Observations in Oklahoma 2010-2017 4
  - Chapter 5: Realizing the Potential of the Full Gravity Method 4

Chapter 2: Earthquake-Like Slip-Events 5

- Preamble 5
- Abstract 5
- Experimental Simulations of Earthquakes 6
- Present Experiments 10
  - Loading System 10
  - Control System 12
  - Samples Composition 12
  - Experimental Procedure 12
  - Loading Procedures 13
  - Data Monitoring and Analysis 15

Wear Measurement and Wear-Rate Calculations 17
Experimental Energy Density 18
Experimental Strength Evolution 19
ELSE procedure as earthquake proxy 25
Implications to Large Earthquakes 26
Fault Strength 26
Total Potential Energy and Relations to Large Earthquakes 26
Slip-Weakening Distance 29
Impact Loading and Fault Weakening 30
Summary 37
Chapter 3: Seismic Tomography of Tangshan, China 39
Preface 39
Abstract 39
Introduction 41
Field Operations 43
Data Processing 44
3D Modeling 46
2D Modeling 47
Visualization 49
Synthesis: Subsurface Structures and Fault Zones 49
Discussion 52
Geologic Implication of the Tomography Results 52
Structural Complexity 52

Implications with Respect to Earthquake Hazard 53
Summary 53
Chapter 4: Seismological Observations in Oklahoma 2010-2017 55
Preamble 55
Abstract 55
Introduction 56
Tectonic Setting 56
Seismic Activity and Probabilistic Hazard 56
Induced vs. Tectonic Seismicity 59
This Study 59
Oklahoma Regional Seismic Network 62
Network and Data Description 62
Data Acquisition 64
Magnitude Calculation 66
Oklahoma Seismicity 67
Seismicity Trends 2010-2017 67
Hypocenters 69
Focal Mechanisms 75
The 03 September 2016 M5.8 Pawnee Earthquake 76
Mainshock 78
Aftershocks 79
Long-term Deformation 81
Discussion 81

Spatiotemporal Correlations of Earthquakes with Oil and Gas Activity ........... 81

Anomalous Seismicity and Aseismicity ........... 83

Seismicity and its Relationship to Mapped Faults ........... 83

Inducing Seismicity ........... 85

The M5.8 Pawnee Earthquake as a Possibly Induced Earthquake ........... 85

Summary ........... 86

Chapter 5: Realizing the Potential of the Full Gravity Field ........... 88

Preamble ........... 88

Abstract ........... 88

Introduction ........... 89

Current Gravity Modeling ........... 89

Mass Approximation Methods ........... 90

This Study ........... 91

Theory ........... 92

Vertical Line Mass Approximation ........... 92

Methodology ........... 92

Highly Parallel Processing ........... 95

Advantages and Disadvantages of Using Vertical Line Elements ........... 95

Numerical Implementation ........... 96

Gravitational Potential of a Point Source ........... 96

Volume and Mass from a Vertical Line ........... 99

Quadtree Method in SIGMA ........... 99

Application ........... 102

Case 1: Gravity Effect of a Sphere ............ 102

Case 2: Modeling a Gravity High in Osage, Oklahoma ............ 105

Case 3: Full-Field Modeling ............ 111

Conclusions ............ 123

Dissertation Summary ............ 124

References ............ 125

Appendix A: Collaborative Contributions in Journal Publications ............ 133

Induced Seismicity in Central Oklahoma ............ 133

Fluid Injection, Earthquake, and Fault Interactions in Pawnee, Oklahoma ............ 134

Potentially Induced Earthquakes are Indistinguishable from Tectonic Earthquakes ............ 135

Slip-Model of the Pawnee M5.8 Earthquake from Geodetic Observations ............ 137

Earthquake Propagation from Slip-Pulse Models ............ 138

Fault-Surface Evolution with Respect to Fault-Wear ............ 139

# List of Tables

Table 1. Fault Patch vs. ELSE Experiment........................................................14

Table 2. Seismic and Energy Data........................................................29

Table 3. Oklahoma Seismicity from 1970 to 2017........................................................59

Table 4. Seismic Velocity Profile for Oklahoma........................................................66

# List of Figures

Figure 1. Schematic Diagram of Earthquake Rupture Propagation 8

Figure 2. Stress and Energy on a Fault Patch During an Earthquake 9

Figure 3. The Rotary Shear Apparatus 11

Figure 4. Friction and Velocity Evolution in ELSE Experiments 21

Figure 5. Sierra White Granite Friction and Velocity vs. Slip-Distance 22

Figure 6. Kasota Dolomite Friction and Velocity vs. Slip-Distance 23

Figure 7. Energy, Slip-Distance, and Friction Strength During ELSE Experiments 24

Figure 8. ELSE vs. Steady-State Experiments 32

Figure 9. Slip-Acceleration and Fault-Wear 34

Figure 10. The 28 July 1976 M7.5 Tangshan Earthquake 40

Figure 11. Modified Mercalli Intensity for the Tangshan Earthquake 42

Figure 12. Tangshan 3D Seismic Survey Geometry 43

Figure 13. Typical Seismic Data from the Tangshan Survey 46

Figure 14. 2D Forward Raytracing Model Across the Study Area 47

Figure 15. Horizontal Depth Slices of the Tomography Volume 48

Figure 16. Fault Interpretation from the Tomography Model 51

Figure 17. Oklahoma Seismicity from 1970 to 2017 58

Figure 18. Legacy Seismic Monitoring Stations in Oklahoma 60

Figure 19. Current Seismic Monitoring Stations in Oklahoma 61

Figure 20. Regional Seismic Monitoring Network 62

Figure 21. Monthly Seismicity in Oklahoma 68

Figure 22. Oklahoma Seismicity Map: 1882-2009 70

Figure 23. Oklahoma Seismicity Map: 2010 .... 70
Figure 24. Oklahoma Seismicity Map: 2011 .... 71
Figure 25. Oklahoma Seismicity Map: 2012 .... 71
Figure 26. Oklahoma Seismicity Map: 2013 .... 73
Figure 27. Oklahoma Seismicity Map: 2014 .... 73
Figure 28. Oklahoma Seismicity Map: 2015 .... 74
Figure 29. Oklahoma Seismicity Map: 2016 .... 74
Figure 30. Oklahoma Seismicity Map: 2017 .... 75
Figure 31. Oklahoma Focal Plane Solutions .... 76
Figure 32. Sand Blows near the M5.8 Pawnee Epicenter .... 77
Figure 33. Fissure near the M5.8 Pawnee Epicenter .... 78
Figure 34. Seismicity Map of the Pawnee Aftershocks .... 80
Figure 35. Oklahoma Fault Map .... 84
Figure 36. Seismogenic Faults from this Study .... 84
Figure 37. Underground Mass Body Represented by Prisms .... 91
Figure 38. Semi-infinite Vertical Line Elements .... 94
Figure 39. Errors from Using Vertical Line Mass Elements (from Hammer, 1974) .... 96
Figure 40. Visualization of the Quadtree Division in SIGMA .... 101
Figure 41. Standard Test Sphere for Gravity Calculations .... 102
Figure 42. Analytical vs. SIGMA Results .... 104
Figure 43. Free Air Anomaly Maps .... 107
Figure 44. Osage Anomaly Density Model .... 109
Figure 45. Monoscopic vs. Periscopic Vision .... 114

Figure 46. Ambiguity in Gravity Observations ........................................................ 115

Figure 47. Classical Mass Bodies from a Different Perspective ................................ 116

Figure 48. Using Different Gravity Observations to Delineate Mass Bodies.............. 117

Figure 49. Schematic Diagram the Synthetic Survey Design...................................... 119

Figure 50. Synthetic Survey Design .......................................................................... 120

Figure 51. 2D slices through density volumes........................................................... 122

# Abstract

This dissertation encompasses a wide range of scale that investigates the tectonic processes in the crust with respect to faulting and earthquakes. of tectonic and earthquake processes in the crust. I present in four chapters: (1) rotary shear experiments in the laboratory that simulate earthquakes of $M_W$4-8, which I define the Coulomb Energy Density as a new unit to quantify seismic energy that is proportional to slip-distance of an earthquake patch; (2) a 3D seismic tomography to delineate the basin thickness underlying Tanghsan, China, which is a densely populated city with a history of catastrophic seismicity; (3) seismic observations from Oklahoma 2010-2017, where a sudden increase from less than three felt earthquakes per year prior to 2010 to over 900 felt events in 2015, points to the involvement of wastewater disposal wells and hydraulic fracturing stimulations as likely triggers; and (4) I created a fast and accurate method of calculating gravity effects of mass, which was used to model crustal structures to investigate Oklahoma seismicity.

# Chapter 1: Introduction

## Summary

The dissertation incorporates studies of tectonic and earthquake processes in the crust. The study includes selected topics that span in scale from small scale laboratory experiments to regional scale seismic monitoring and analysis to larger scale earthquake hazard analysis. (1) Experimental studies of Earthquake-Like-Slip-Events (ELSE): the project is based on a suite of laboratory experiments, conducted with a high-velocity rotary-shear apparatus, and aims at deriving constitutive relations with regards to earthquake processes. The present experiments use a unique clutch-flywheel configuration that allows better simulation of the rupture processes of large earthquakes. (2) Oklahoma seismicity from 2010-2017: the chapter encapsulates the recent rise in earthquake occurrences in Oklahoma and largest moment releases in its instrumented history. (3) A three-dimensional (3D) Seismic Tomography investigation of the Tangshan area of China: the project develops a new 3D survey design for working around a major urban area with a population of over 7.5 million people. (4) A new method to utilize gravity data using a Semi-Infinite Gravity Modeling Algorithm (SIGMA)

## Dissertation Organization

My dissertation includes four research chapters. Chapter 2 presents experimental analysis and numerical models of earthquake physics focus on friction and dynamic weakening of faults. We developed a new method for studying experimental slip, using a rotary-shear apparatus in OU that we refer to as Earthquake-Like-Slip-Events (ELSE). Chapter 3 reports the seismic tomography investigation Tangshan, China. We followed the 1976 earthquake in Tangshan, China that ranks as the deadliest earthquake in the 20th century. The presented three-dimensional (3D) tomographic survey aims to elucidate the vertical and lateral extent of the sedimentary fill, and to delineate subsurface structures to correlate them with known surficial geology. Chapter 4 presents seismological observations in Oklahoma 2010-2017 that were recorded in the Oklahoma Geological Survey (OGS) earthquake catalog. Part of the results are focused on local areas of interest that surround significant seismicity, e.g., the M5.8 Pawnee earthquake. Chapter 5 outlines a new approach to model gravity data. I developed a new algorithm to calculate (1) gravity and (2) six components of gravity gradiometry from mass approximations using vertical line elements. This program was used in the OGS seismicity reports, when crustal models were used.

## *Chapter 2: Earthquake-Like Slip Events*

Experimental studies and numerical models of earthquake physics focus on friction and dynamic weakening of faults. Constitutive relationships between traditional experiments are conducted on (1) direct-shear apparatuses, with two or three solid blocks (Okubo and Dieterich, 1981), (2) rotary-shear apparati, with cylinders presses against each other (Tsutsumi and Shimamoto, 1997), or (3) a high-velocity impactor, with a stationary sample being loaded by a projectile (Yuan and Prakash, 2008). The direct-shear method is capable of high normal stresses, but limited to low velocity and short slip-distances. The rotary-shear method is capable of high slip-velocities, and virtually unlimited slip-distances, but limited to low normal stresses. The impactor design reaches high velocity during a short slip-distance, with a finite amount of energy delivered to the sample. We developed a new method for studying experimental slip, using a rotary-shear apparatus in OU that we refer to as Earthquake-Like-Slip-Events (ELSE).

We propose a new measure of energy, the Coulomb energy density ($E_C$), which takes into account the normal stress on a fault and is more relevant when dealing with fracture energy ($E_G$). Another derivation from this study is the effect of loading rate an history on the system, since we can compare ELSE friction-velocity history with the conventional constant-velocity, steady-state experiments from previous studies (Reches and Lockner, 2010). These results will further the understanding of fault behavior during earthquakes. This work was published in Science (Chang *et al.*, 2012).

### *Chapter 3: Seismic Tomography of Tangshan, China*

The 1976 earthquake in Tangshan, China ranks as the deadliest earthquake in the 20th century, with over a quarter of a million people perished (Fang, 1979). The high casualty level for the Mw 7.5 event is due to poor housing construction, and the amplification of ground motion by thick sediment fill in the basin underlying the city. The city of Tangshan has since been rebuilt, but hazards associated with the subsurface geology are still poorly mapped. Our three-dimensional (3D) tomographic survey aims to elucidate the vertical and lateral extent of the sedimentary fill, and to delineate subsurface structures to correlate them with known surficial geology. This study was done with the support and collaboration of the Chinese Earthquake Administration and the results will be used to model predicted ground motion and mitigate the hazards of future earthquakes. A report of the study was filed with the China Earthquake Administration.

### *Chapter 4: Seismological Observations in Oklahoma 2010-2017*

This report comprises seismic events that were recorded in the Oklahoma Geological Survey (OGS) earthquake catalog. The OGS catalog is continually being refined, but this document synthesizes the events from 2010 to 2017. Any future modifications of the OGS catalog will have minimal effect on this report. The report was submitted and published as an OGS Open File Report, and part of the results were used in different peer-review publications, which focused on local areas of interest that surround significant seismicity, e.g., the M5.8 Pawnee earthquake.

### *Chapter 5: Realizing the Potential of the Full Gravity Method*

A multi-disciplinary project of the Oklahoma Geological Survey (OGS) to understand Oklahoma seismicity and crustal structure required a detailed 3D velocity and density model of the crystalline basement, which is where most of the hypocenters are located. Conventional 3D gravity modeling at this scale (10º latitude x 10º longitude) and desired resolution (meters) would have taken months of dedicated computer time per iterations or petabytes of computer memory by GM-SYS (a commercial modeling software run on desktop workstations). To address these challenges, I developed a new algorithm to calculate (1) gravity and (2) six components of gravity gradiometry from mass approximations using vertical line elements. The new algorithm is thousands of times faster than conventional approaches, and can theoretically produce unique solutions to inverse problems, which is considered an impossibility in geophysical potential methods. This program was used in the OGS seismicity reports, when crustal models were used.

# Chapter 2: Earthquake-Like Slip-Events[1]

## Preamble

The text and figures in this chapter are from my first-authored publication in Science, in 2012, with my co-authors Dr. Ze'ev Reches and Dr. David A. Lockner (cf., Appendix A). Here, I combine the published work with its online supplementary materials to provide a more comprehensible body of work for the dissertation, since the main article in Science is informationally dense. I inject supplementary texts and figures where the main article refers to the online supplementary materials.

## Abstract

After nucleation, a large earthquake propagates as an expanding rupture front along a fault. This front activates countless fault patches that slip by consuming energy stored in Earth's crust. We simulated the slip of a fault patch by rapidly loading an experimental fault with energy stored in a spinning flywheel. The spontaneous evolution of strength, acceleration, and velocity indicates that our experiments are proxies of fault-patch behavior during earthquakes of moment magnitude ($M_W$) = 4 to 8. We show that seismically determined earthquake parameters (e.g., displacement, velocity, magnitude, or fracture energy) can be used to estimate the intensity of the energy release during an earthquake. Our experiments further indicate that high acceleration imposed by the earthquake's rupture front quickens dynamic weakening by intense wear of the fault zone.

---

[1] This chapter was published as: Chang, J.C., Lockner, D.A., and Reches, Z., 2012, Rapid Acceleration Leads to Rapid Weakening in Earthquake-Like Laboratory Experiments: Science, v. 338, n. 6103, p. 101-105.

## Experimental Simulations of Earthquakes

Large earthquakes initiate at a small nucleation area, and grow as propagating rupture-fronts (Heaton, 1990; Tinti *et al.*, 2005) (Fig. 1). The propagating front activates a multitude of fault-patches that undergo intense deformation (Ohnaka and Yamashita, 1989; Abercrombie and Rice, 2005; Andrews, 2005; Tinti *et al.*, 2005; Kanamori and Rivera, 2006) (Fig. 2A-B). Before the front arrives, the stress, $\mu$, on each patch is lower than its static strength, $\mu_s$, (both stress and strength are presented here as the friction coefficient, $\mu =$ [shear stress/normal stress]). Next, when the front approaches, the stress abruptly rises (1), and once the static strength is exceeded, the patch accelerates and its strength drops by dynamic weakening (Fig. 2A). As the patch slips, it releases elastic energy stored in the surrounding rock, and eventually decelerates and stops. While this earthquake model is widely accepted (Okubo and Dieterich, 1981; Lockner and Okubo, 1983; Ohnaka and Yamashita, 1989; Heaton, 1990; Abercrombie and Rice, 2005; Andrews, 2005; Tinti *et al.*, 2005; Kanamori and Rivera, 2006), the details of the evolution of strength, velocity and energy partitioning are poorly constraint (Tinti *et al.*, 2005; Kanamori and Rivera, 2006).

In stick-slip experiments (Okubo and Dieterich, 1981; Ohnaka and Yamashita, 1989), the above earthquake sequence was simulated by loading two rock blocks until the experimental fault failed spontaneously to generate an earthquake-like event (Okubo and Dieterich, 1981) (Fig. 2A). However, due to experimental constraints, the stick-slip displacements were in the order of tens of microns or less (Fig. 2A) (Okubo and Dieterich, 1981; Lockner and Okubo, 1983; Ohnaka and Yamashita, 1989), some five orders of magnitude less than displacements of large earthquakes. To circumvent this limitation, earthquake modelers have relied on constitutive equations, like rate- and state-dependent friction (Dieterich, 1981), based on low-velocity, nearly steady-state rock friction data.

The objective here is to experimentally simulate fault-patch slip during large earthquakes. We employ one central concept: abruptly deliver a finite amount of potential energy to an experimental fault-patch, which spontaneously dissipates the energy without operator intervention. We use a rotary-shear apparatus, in which a ring-shaped fault slips at velocities of 0.001 to 2 m/s, under normal stresses of up to 35 MPa (Reches and Lockner, 2010). The raised-ring design of the experimental fault-blocks have a small (14%) velocity difference between the outer and inner diameters that does not require velocity corrections, which are needed for solid cylinder blocks. We continuously monitor, at frequencies of up to 5 kHz, the velocity ($v$), normal stress ($\sigma_n$), shear stress ($\tau$), fault-parallel displacement (slip-distance), fault-normal displacement (U; dilation $< 0 <$ closure), and sample-temperature at 3 and 6 mm from the slip-surface.

Each experiment starts by accelerating a massive disk-shaped flywheel (moment of inertia = 40.5 kg $m^2$) to a prescribed angular velocity, $\omega$; during this stage, the sample is disengaged from the flywheel and remains stationary. Then, the flywheel simultaneously disengages from the drive motor and engages to the rock sample, transferring its potential energy to the experimental fault-patch. The patch spontaneously dissipates the flywheel energy by rapid acceleration followed by decelerating slip. We refer to this experiment as an "earthquake-like slip-event" (ELSE).

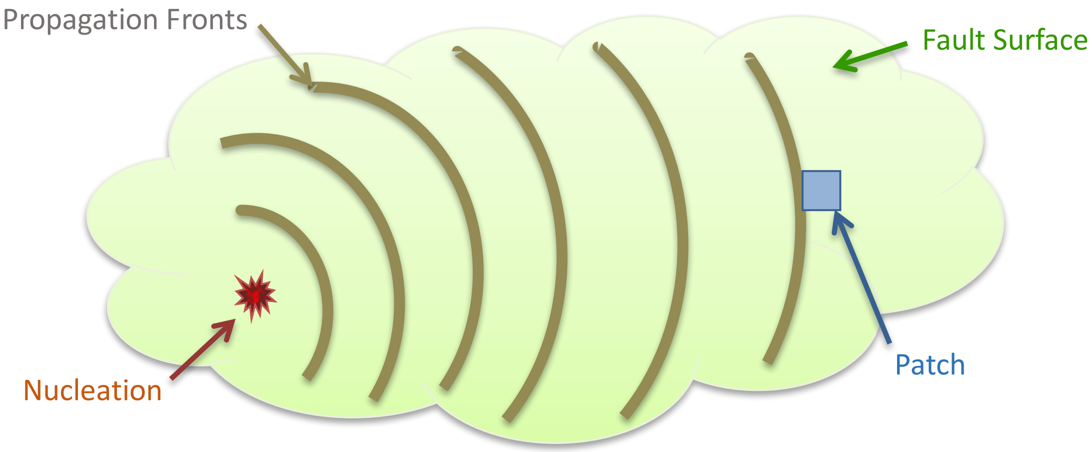

**Figure 1. Schematic Diagram of Earthquake Rupture Propagation**
Schematic representation of an earthquake. Rupture nucleates somewhere on the fault, and propagates via slip of numerous fault patches.

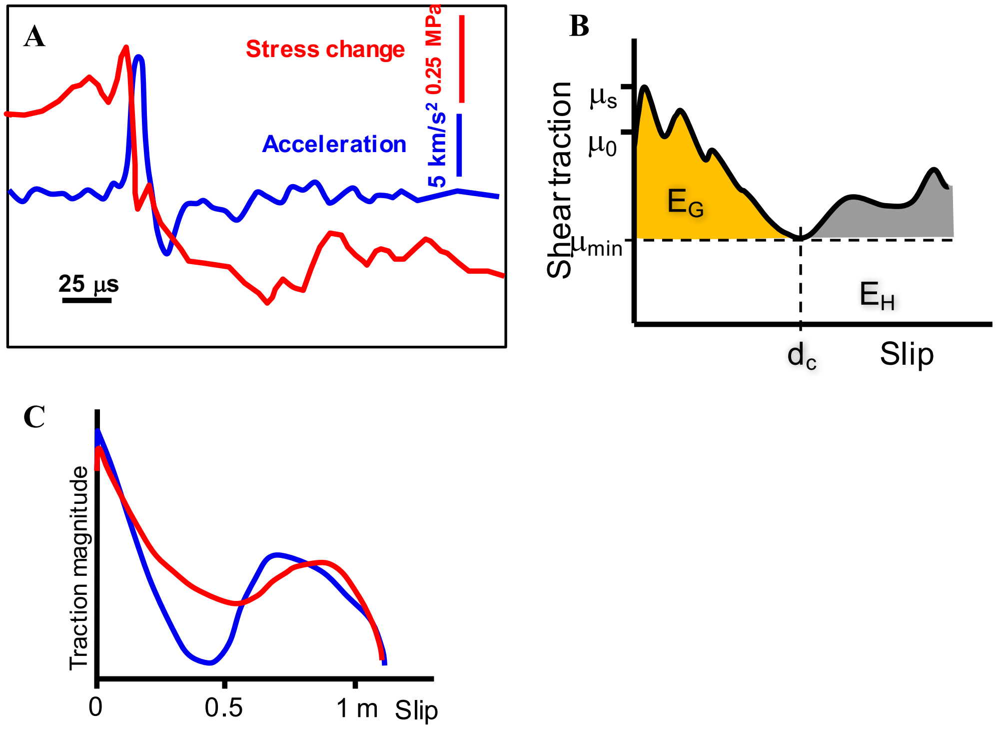

**Figure 2. Stress and Energy on a Fault Patch During an Earthquake**
(A) Shear stress and slip acceleration during a spontaneous stick-slip event along experimentally loaded granite fault (3); total slip ~ 4 $\boldsymbol{\mu}$m. (B) Conceptual evolution of shear traction on a fault patch during an earthquake (Tinti *et al.*, 2005); $d_C$ is the critical distance of dynamic slip weakening, $E_G$, $E_H$ and $E_R$ are the energies per unit area attributed to fracture, heat and radiation respectively. (C) Seismically calculated traction evolution of two fault patches during the Landers earthquake (Tinti *et al.*, 2005); relative scale of the shear traction axis. Note that $d_C$ appears early (blue patch) or late (red patch).

## Present Experiments

### *Loading System*

The apparatus frame is 1.8 m tall with two massive decks (Fig. 3A-C). The decks are connected to each other by four rectangle legs. The tested sample is placed between the two decks, and it is loaded by the rotary train from below and by normal stress from above (Fig. 3). The power system includes:

(1) A 100 HP three-phase electric motor (Reliance) and controller (Baldor) that provides torque of up to 3,000 Nm at any velocity from 0 RPM to 3300 RPM, and which can accelerate to full rotation speed in 0.1 s. The motor velocity is monitored and controlled through an 8192 sector encoder.

(2) The main rotary shaft is powered by the motor with 1:6 velocity reduction sprockets.

(3) A 225 kg flywheel with its own clutch.

(4) An electromagnetic clutch (Ogura) with full engagement in 30 ms.

(5) A hydraulic piston system (Enerpac) with axial load up to 9,500 N.

(6) Torque monitoring system (Fig. 3A-B) designed to measure to shear stress along the experimental fault.

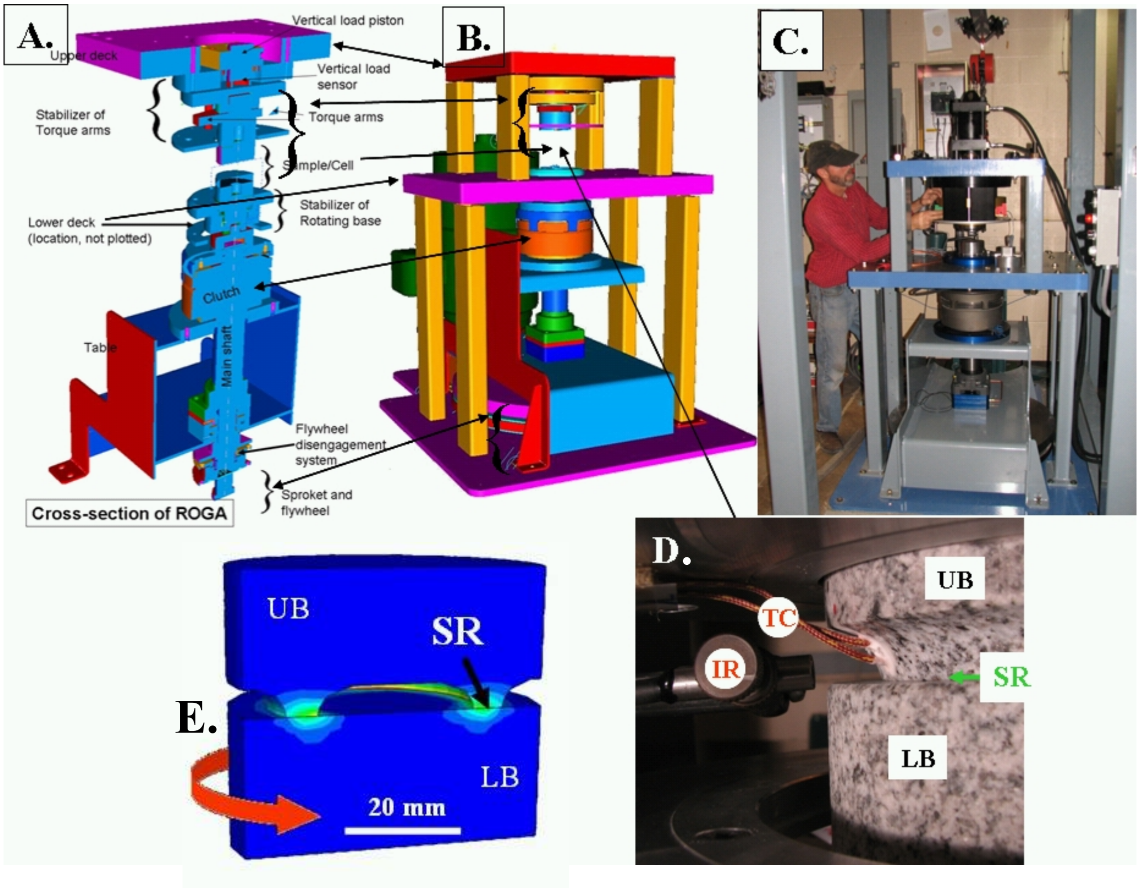

**Figure 3. The Rotary Shear Apparatus**
(A) Generalized cross section displaying power train. (B) 3D view of the assembled apparatus. (C) The apparatus with builder Joel Young. (D) Sample blocks assembled in the loading frame. LB-lower block; UB-upper block; SR-sliding ring; TC-thermocouple wires; IR-infra red sensor. (E) Sample design shown as vertical cut-through of two cylindrical blocks of solid granite rock. The colors indicate temperature distribution due to frictional heating calculated using a finite-element model.

### *Control System*

The control system is based on National Instruments components, and it includes a SCXI-1100 with modules 1124 (analog control) 1161 (relay control), 1520 (load cell/strain gage), and 1600 (data acquisition and multiplexer), as well as a USB-6210 (sample encoder measurement). The system operations are control by a dedicated LabView (NI) program. Monitoring devices are described below.

### *Samples Composition*

Sierra White Granite (SWG): Electron-microprobe (EMP) modal analysis shows that this rock is comprised of six main minerals: plagioclase (48%), quartz (38%), alkali-feldspar (5%), ferromagnesian- mica (5%), and muscovite (5%). Mean grain size is about 0.3 mm; mean void space in EMP images is ~4%.

Kasota Dolomite (KD): The samples of Kasota Dolomite were supplied by Cold Spring Granite, Texas. It is quarried at Mankato, Minnesota, and it is supplied under the commercial name “Kasota valley limestone”. X-ray diffraction (XRD) analysis indicates that our samples are 97.3% dolomite, 2.6% quartz, with traces amounts of plagioclase.

### *Experimental Procedure*

A key requirement in our earthquake simulation is that the time-histories of both, friction and slip-velocity, will be determined by the sample response and not programmed by the operator. To achieve this requirement, we utilize the massive (225 kg) flywheel of our system. The flywheel is linked to the power axis with two clutches. Clutch #1 connects/separates the flywheel to/from the motor; it is a “dog clutch” that engages by four interlocking cogs on each side. It is engaged manually before the experiment, and disengaged by the controlling program during the experiment. Clutch #2 connects/separates the flywheel to/from the sample. It is an electromagnetic clutch that is fully engaged within 30 ms, and is engaged/disengaged by the controlling program.

### *Loading Procedures*

An entire ELSE run generically proceeds as follows, which is a proxy for what are generally accepted stages of large earthquake cycles (Tbl. 1). (1) The rock samples are placed into the sample cell and placed under a normal load. During this time, the flywheel is connected to the motor, and disengaged to the sample; this guarantees no shear loading on the sample during the energy accumulation (Stage I). (2) The flywheel rotates, via the motor, to a prescribed angular velocity (Stage II and III). (3) Once the flywheel is rotating at the prescribed angular velocity, the flywheel simultaneously (within 30ms) disconnects from the motor and engages the sample. This step abruptly loads the experimental fault-patch with the potential energy built-up from the rotating flywheel (Stage IV). (4a) If the potential energy of the rotating flywheel is not enough to overcome the static strength of the loaded sample, the flywheel stops without the sample slipping. This ends the ELSE run at Stage V (Tbl. 1). (4b) If the potential energy of the rotating flywheel is enough to overcome the static strength of the loaded sample, the sample slips for a finite distance, D, until the energy from the flywheel is completely consumed or the stress drops below the patch-strength (Stages V-VII).

| Step | Fault patch during an earthquake | Flywheel-controlled ELSE experiment |
|---|---|---|
| I | Locked patch on a fault-zone in the crust. | A two-block sample (=experimental fault) is loaded to a selected normal stress; clutch #1 is engaged, clutch #2 is disengaged. |
| II | Interseismic period: increase of crustal elastic strain energy (=potential energy) around the fault. The shear/normal stress ratio reaches $\mu_o$. | The flywheel is rotated to a prescribed velocity (=storing potential energy); clutch #1 is engaged, clutch #2 is disengaged. |
| III | Earthquake nucleation on the fault-zone away from the patch (Fig. 1). | No sample-slip. |
| IV | Earthquake rupture front arrives at the patch (Fig. 1); shear/normal stress increases. | Clutch #1 is disengaged & clutch #2 is engaged ⇒ flywheel energy is transferred to sample |
| | | ⇒ shear stress on sample rises. |
| V | The shear/normal ratio increases to $\mu$. If $\mu < \mu_S$ (static strength) ⇒ patch remains locked, and if $\mu > \mu_S$ ⇒ patch slips (Fig. 2B). | If shear/normal stress ratio $< \mu_S$ (static strength) ⇒ patch remains locked; |
| | | If shear/normal stress ratio $> \mu_S$ ⇒ patch slips |
| VI | Patch may undergo dynamic weakening or hardening, generating, or not, an instability | Experimental patch may dynamically weaken or strengthen, generating, or not, an instability |
| VII | Patch slips distance D; slip terminates when there is no more available energy or stresses drop below patch strength. | Sample slips for distance D; slip terminates when there is no more available energy or stresses drop below patch strength. |

**Table 1. Fault Patch vs. ELSE Experiment**
The steps of the earthquake rupture process on a fault-patch, and the experimental procedure used here for flywheel-controlled ELSE experiments.

## *Data Monitoring and Analysis*

### ***Equipment***

The monitored parameters are:

- Sample normal load is measured with Honeywell load-cell installed below the axial load piston.
- Sample torque is measured with a 1250-lb load cell made by Transducer Techniques, which is installed against a 0.1524 m arm connected to the upper, stationary block.
- Displacement normal to the fault surface is measured with four eddy-current sensors made by Lion's Precision (± 1 micron accuracy).
- Sample temperature is measured with two K thermocouples (Omega) that are embedded 3 and 5 mm from the sliding surfaces (Fig. 3).
- Sample angular velocity is measured with a Sick-Stegmann encoder (4096 sections per revolution) installed below the lower, rotating block. Both the encoder counts and its voltage output were recorded.
- Motor velocity is measured with a second, identical Sick-Stegmann encoder installed on the motor.
- Motor torque is a voltage value output of the Baldor controller.
- Data were recorded continuously at rate of either 5,000 samples/sec or 2,000 samples/sec.

### ***Data Filtering***

The recorded data were checked and filtered as follows:

1. Checking and correcting time-lag between the two monitoring units of SCXI-1100 (all volt data output) and the USB-6210 (counter data from the sample-encoder). Checking was done by comparing the timing between the encoder counting recorded on the USB-6210, and the encoder voltage recorded with the SCXI-1100, and the time-lag was corrected by shifting the time difference.
2. Slip-velocity was calculated in steps. First fitting a piece-wise polynomial curves (typically power of 10-20) to the encoder counter data. This operation smoothens the step-wise output of the encoder and eliminated artifacts of temporary velocity jumps (associated with the width of sections within the encoder). The velocity is then calculated from this fitted curve according to sample geometry.
3. Acceleration was calculated as the derivative of the velocity history, and filtered with an averaged running-window of 0.01 s width.
4. Friction coefficient (=frictional strength), $\mu$, is the calculated ratio of shear load (measured by the torque load cell) to normal load (measured by the axial load cell). The friction coefficient is filtered with an average-running-window of 0.01 s width.

### *Wear Measurement and Wear-Rate Calculations*

The common methods of wear measurements are (1) weighing wear products; (2) measuring displacement normal to the sliding surfaces; and (3) optical techniques. The weighing powder method is a time-consuming process that disrupts the structure of the fault, and thus makes it impossible to return to the previous stage after the measurement. Optical methods cannot be conducted continuously, and require an accurate reference surface. We determine wear by continuously monitoring the fault-normal displacement, U, with four eddy-current sensors (~1 $\mu$m accuracy) attached to the sample holders. Positive U is defined as fault-closure, and negative $U$ as fault-dilation. Fault-normal displacement has four contributors: (1) surface wear, W, indicated by fault-closure ($U > 0$); (2) thermal expansion due to frictional heating of the sample, results in fault-dilation ($U < 0$); (3) compaction ($U > 0$) or dilation ($U < 0$) of the gouge zone or the sample; and (4) elastic response of changes in the normal stress.

We calculated the time-dependent wear-rate in steps. First, the thermal contribution is determined by using the measured temperature from the thermocouple, embedded 3 mm away from the fault. The fault closure due to its cooling was monitored for a period of 10-120 s after the sample stopped slipping. During this period of post-slip cooling, the fault closure is nearly linear with the decrease in temperature, and this closure is used to calculated an empirical thermal closure-rate parameter, $T_G = dU/dT$, where T is the measured temperature during the cooling period. This coefficient varies between runs in the range of 0.2 to 1.6 micron/°C. The thermal contribution during slip is $\Delta U_T = T_G \cdot \Delta T$, where $\Delta T$ is the increase in temperature as measured with the same thermocouple used to calculate $T_G$. The value of $\Delta U_T$ is subtracted from the measured closure to obtain the thermally adjusted $U_t$. Once the gouge layer is established along the patch surface, its thickness is probably nearly constant as the excess gouge is free to be ejected from the sliding surface. Under this condition, the fault-wear is approximately equal to the thermally adjusted closure, $W \approx U_t$. Thus, this wear is the thermally corrected closure (in μm). Next, we corrected for the elastic response of the sample due to normal stress changes. The normal load is maintained constant by an air-pressure/oil actuator that controls the oil pressure in the loading hydraulic piston; this system displays typical short-term variations of 5-10%. We independently measured the elastic fault-normal displacement by using the eddy current sensors under a range of normal loads, and then used this displacement-load relationship to correct for $U_t$ during slip. Finally, we fit a polynomial curve (order of 5-13) to the wear data, and take the derivative of this fitted-curve with respect to fault-slip to obtain the dimensionless *wear-rate,* WR = ($d$W/$d$x), where x is fault-parallel slip.

There is no universal wear-rate unit, and we used a simple, pure geometric unit,

$$WR \equiv \frac{[volume\ of\ wear\ products]/[area\ of\ sliding\ surfaces]}{[slip\ distance]}$$

$$\equiv \frac{[thermally\ corrected\ closure]}{[slip\ distance]}$$

The wear-rate unit can be dimensionless [m/m], or [$10^{-6}$ m/m] = [μm/m]; we used the latter, which is more suitable for the range of our experimental results.

## Experimental Energy Density

We conducted 43 ELSE experiments on samples of SWG, and 23 experiments on KD samples. Slip-velocity, shear and normal stresses, fault displacements and temperature were recorded at 1 to 5 kHz. Only two controlling parameters were preselected for each experiment: the energy density $E_T$ = (total flywheel kinetic energy/patch area), and the normal stress on the patch, $\sigma_n$. During slip, the flywheel energy is dissipated by patch frictional work; the latter equals $\bar{\mu}\sigma_n D$, where $\bar{\mu}$ is the average friction coefficient, and D is total slip. Thus, the ratio $E_C = E_T/\sigma_n \sim \bar{\mu}D$ is an energy parameter that controls total slip. We define $E_C$ as the 'Coulomb energy density' (with units of meters). In the present experiments, $E_C$ ranges from $1.4 \cdot 10^{-6}$ to 2.6m (Tbl. 1).

## Experimental Strength Evolution

We first consider a typical run, in which a SWG sample (#733, Fig. 4A) sheared at $\sigma_n$ = 6.8 MPa, and $E_C$= 0.42 m. The patch spontaneously accelerated to a peak velocity of $V_p$ = 0.70 m/s and slipped for 0.86 m during 2.50 s. The initial patch strength was $\mu_s$ = 0.66, and strengthened to $\mu$ = 0.69 within the first 1.8 mm of slip. Then, the strength dropped to a minimum value of $\mu_{min}$ = 0.35 over an additional slip-distance of 45.5 mm. Finally, the patch strength recovered to $\mu$ = 0.81 as the sample decelerated (Fig. 4A). Similar patterns of strength evolution were observed for ELSE experiments (Figs. 5 and 6) with the following general characteristics:

1. Slip initiates when the stress exceeds the static frictional strength $\sigma_s$ (Fig. 2A-D).
2. Many experiments showed a brief strengthening stage (Fig. 2B), and with continued slip, the strength decreased to a minimum value, $\sigma_{min}$. In nearly all cases, re-strengthening appeared during deceleration (Fig. 2A-D).
3. Most ELSE runs (48 out of 66 experiments) displayed significant dynamic weakening (Figs. 5 and 6). The intensity of dynamic weakening appears to

primarily depend on the intensity of the Coulomb energy density (Tbl. 2): Five runs with $E_C < 0.001$ m did not slip, four runs with EC < 0.03 m slipped but did not reach weakening, and nine runs displayed negligible weakening ($\mu$-drop < 0.05).

4. SWG samples loaded by high energy density of $E_C > 0.1$ m displayed high-frequency stick-slip behavior; this mode was less common in KD samples.
5. The total slip distance during ELSE experiments, D, is proportional to the Coulomb energy density with the simple power relations of $E_C = 0.605 \cdot D^{0.933}$ for both granite and dolomite experiments, over almost four orders of magnitude (solid diamonds, Fig. 7A).

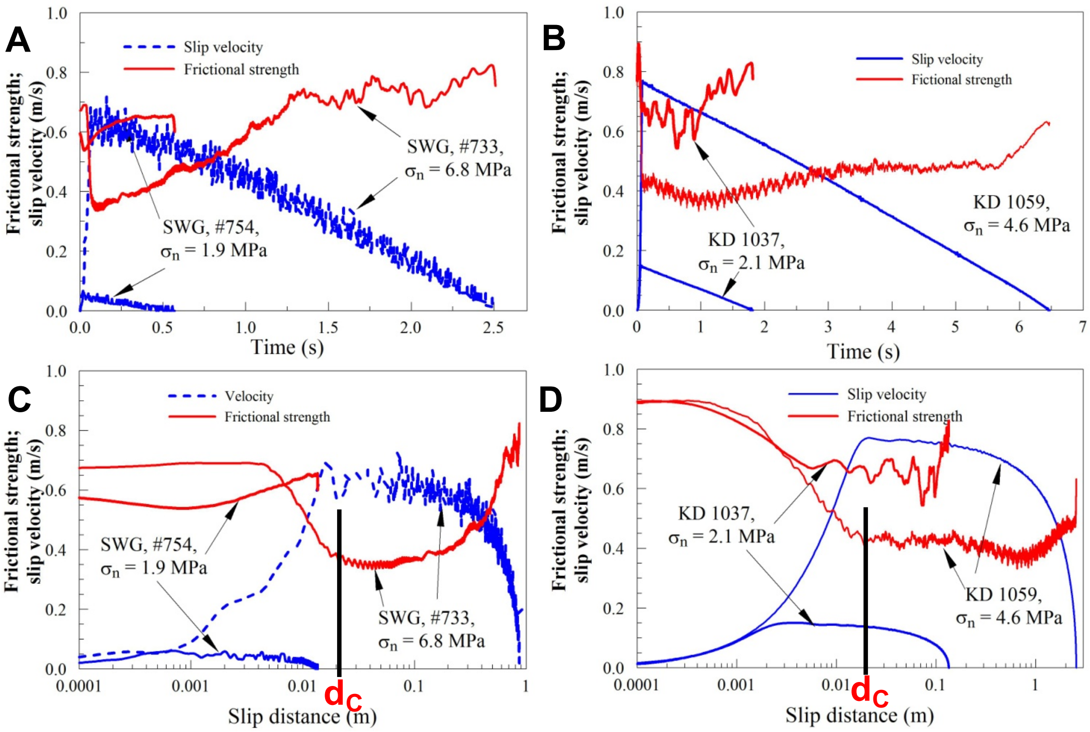

**Figure 4. Friction and Velocity Evolution in ELSE Experiments**

The evolution of frictional strength and slip velocity in ELSE experiments with respect to time (A, B), and slip distance (C, D). A and C: Two runs with Sierra White Granite loaded with potential energy density ($E_C = E_T/\sigma_n$) of $E_C = 0.007$ m (#754) and $E_C = 0.43$ m (#733). B and D: Two runs with Kasota Dolomite loaded with $E_C = 0.09$ m (#1037) and $E_C = 1.20$ m (#1059).

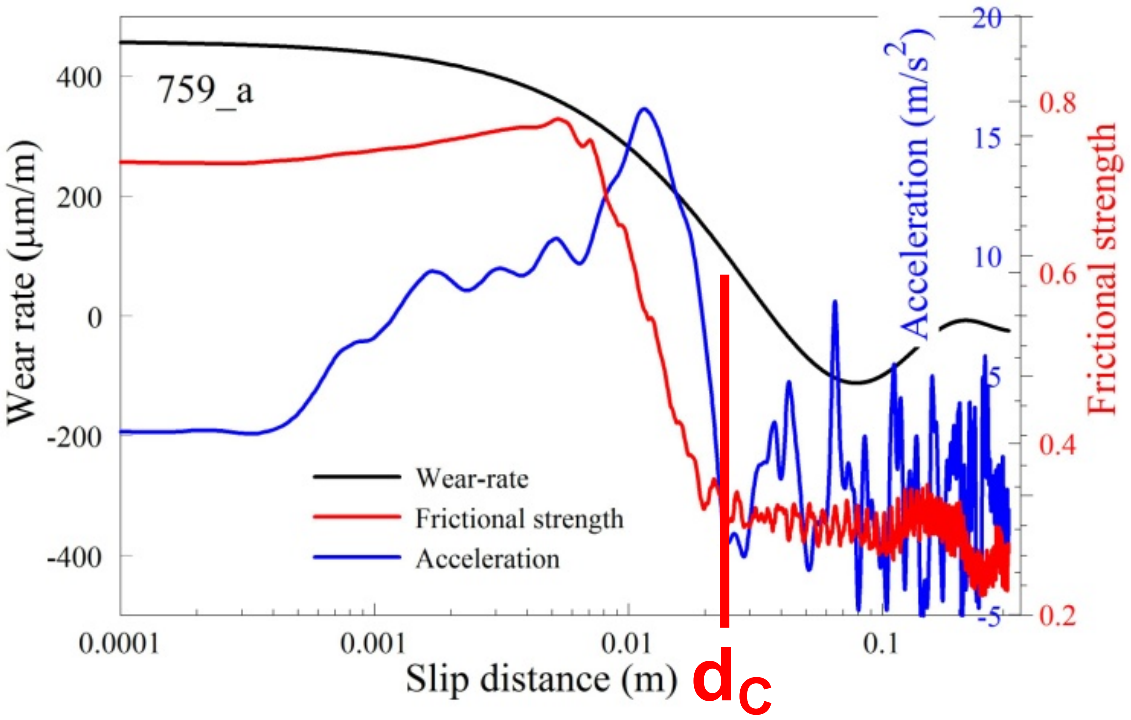

**Figure 5. Sierra White Granite Friction and Velocity vs. Slip-Distance**
Frictional strength (red) and slip velocity (blue) with respect to distance in selected Sierra White Granite experiments (similar to Fig. 4C). Same scales were used for all graphs. The plots are arranged in an increasing order of peak-velocity (from left to right, top to bottom). Note that most runs show an initial strengthening for ~1 cm, and that the five runs in the upper two rows, with slip velocity < 0.15 m/s show no or negligible weakening.

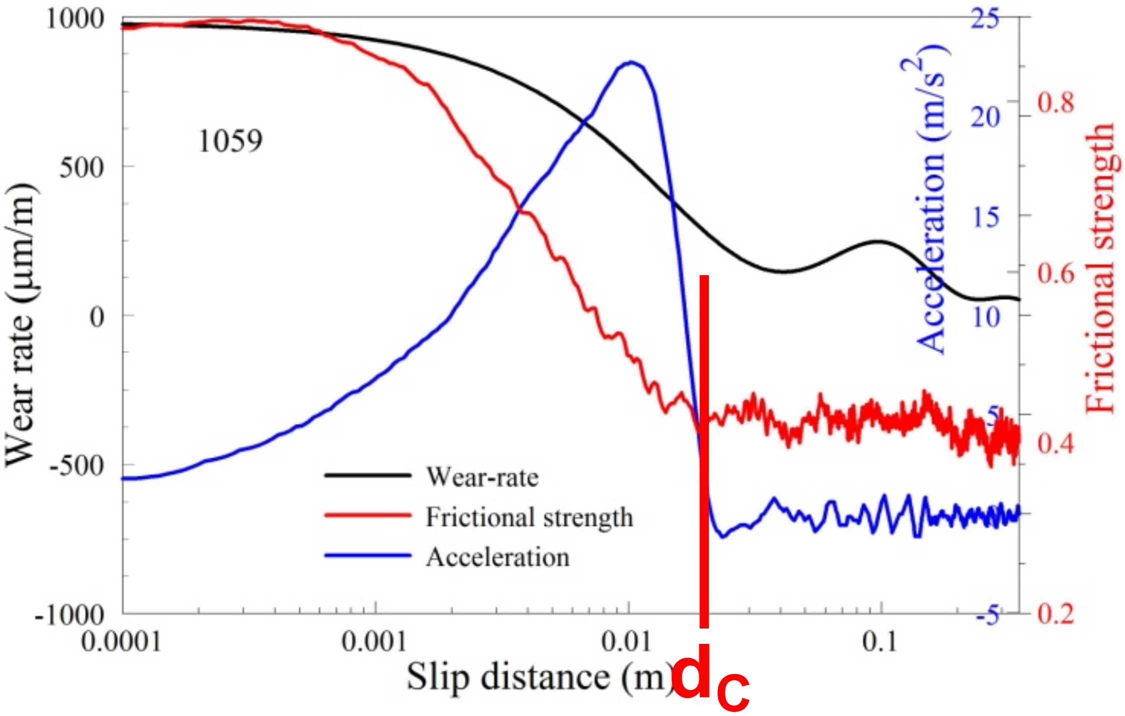

**Figure 6. Kasota Dolomite Friction and Velocity vs. Slip-Distance**
Frictional strength (red) and slip velocity (blue) with respect to distance in selected Kasota Dolomite experiments (similar to Fig. 4D). Same scales were used for all graphs. The plots are arranged in an increasing order of peak-velocity (from left to right, top to bottom). Note that only two runs show a short strengthening stage, and all run showed dynamic weakening.

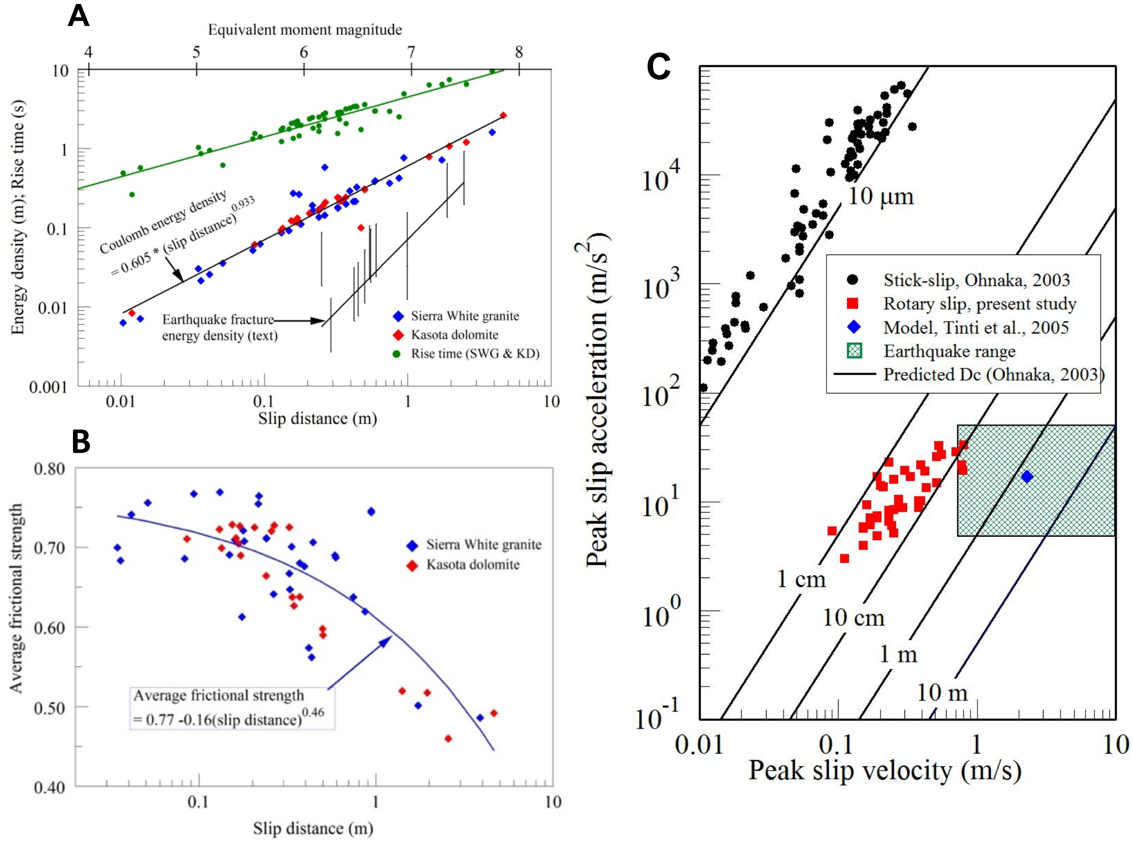

**Figure 7. Energy, Slip-Distance, and Friction Strength During ELSE Experiments**
**A**: The relations of potential energy density ($E_C = E_T/\sigma_n$), slip time (= rise-time, $R_t$), and total slip distance (D). The energy-distance relation of $E_C = 0.605 \cdot D^{0.933}$ (thick, black line) is calculated for both Sierra White Granite runs (blue diamond) and Kasota Dolomite runs (red diamonds). The upper x-axis is the equivalent moment-magnitude, $M_W$, of ELSE runs calculated by assuming that D is equivalent to the mean slip distance during an earthquake (11). Also plotted the normalized fracture energy, $E_G/\sigma_n$, (thin, vertical black lines) that were calculated from kinematic models of six earthquakes (Tinti *et al.*, 2005). **B**: Average frictional strength as function of total slip-distance the 57 ELSE runs with slip > 0.02 m. **C**: Frequency of the slip weakening distance, $d_C$, for all experiments that exhibit dynamic weakening; mean $d_C$ is 27 mm for 23 runs of Sierra White Granite and 12 mm for 23 runs of Kasota Dolomite.

## ELSE procedure as earthquake proxy

The strength-evolution in ELSE experiments (Fig. 4-6) is similar to the strength-evolution in earthquake models (Fig. 2B) (Tinti *et al.*, 2005; Kanamori and Rivera, 2006), stick-slip experiments (Fig. 2A), and seismic analyses (Fig. 2C). To quantify these similarities, we first assumed that the measured slip in ELSE experiments is equivalent to the average slip, $\overline{D}$, during an earthquake. Then, we used the empirical relationships [Wells and Coppersmith, 1994] between the moment-magnitude, $M_w$, and the earthquake average slip, $\overline{D},$ to find that ELSE experiments (D=0.003-4.6 m) correspond to earthquakes in moment-magnitude range of $M_w$=4-8 (upper axis, Fig. 7A). Further, two other experimental parameters, peak-velocity up to 1 m/s, and rise-time of $R_t$ =0.1-10 s (Fig. 7A), have values similar to the equivalent parameters of earthquakes in the same slip range (Gutteri and Spudich, 2000; Tinti *et al.*, 2005). Thus, it appears that ELSE experiments are similar to earthquakes in at least three ways: (1) slip is driven by the release of a finite amount of potential energy; (2) fault strength evolution (Figs. 2C and 4); and (3) seismically observed values, such as average slip, peak-velocity and rise-time (Fig. 7A). These similarities suggest that ELSE tests can be regarded as experimental proxies for fault-patch behavior during earthquakes of $M_w$ = 4-8, and lead us to apply ELSE results to three central questions of earthquake mechanics: fault-strength, total energy, and weakening distance.

## Implications to Large Earthquakes

### *Fault Strength*

Dynamic fault weakening to a minimum-strength, $\mu_{\min}$, is commonly regarded as the source of earthquake slip instability (Okubo and Dieterich, 1981). However, $\mu_{\min}$ is a transient property (Figs. 2B and C; 4A and C; 5; and 6), and thus cannot represent fault strength during the entire slip event. Further, $\mu_{\min}$ is not attained at a consistent displacement, if at all, in different slip events (Tinti *et al.*, 2005) (Figs. 2B and C; 4-6). We propose that the average frictional strength, $\bar{\mu}$, is a more relevant indicator of the dynamic-strength of the fault. In ELSE experiments, the average strength values (Fig. 7B) have simple relations to the total slip-distance, $\bar{\mu} = 0.77 - 0.16 \cdot \mathrm{D}^{0.46}$. This relationship indicates that during slip, average frictional strength decreases with increasing displacement (and energy density, Fig. 7A). Thus, if the strength-distance relations of Figure 7B are applicable to earthquakes, they can explain the better efficiency of large earthquakes (Kanamori and Rivera, 2006).

### *Total Potential Energy and Relations to Large Earthquakes*

Next, we examine if the Coulomb energy density ($E_C$) in ELSE experiments is a reasonable estimate of the total earthquake energy. The latter quantity cannot be determined from seismic data (Tinti *et al.*, 2005; Kanamori and Rivera, 2006), but the fracture energy, which is a fraction of the total energy, can be calculated from seismic data (Abercrombie and Rice, 2005; Tinti *et al.*, 2005; Kanamori and Rivera, 2006). To estimate this fraction, we compare the fracture (=breakdown) energy ($E_G$) determined for six earthquakes (Tinti *et al.*, 2005) to the experimental $E_C$. The earthquake magnitudes are in the range $M_W = 5.6$-$7.2$ (Tbl. 2). The breakdown strength of typical crystalline rock is proportional to the normal stress (Coulomb criterion), and consequently, the breakdown energy calculated for the six earthquakes (Tinti *et al.*, 2005), $E_G$, is also proportional to the associated normal stress. To account for this effect, we divided the seismic $E_G$ by the corresponding $\sigma_n$, and plotted the $E_G/\sigma_n$ ratio of the six earthquakes as a function of their slip distance (black, vertical lines in Fig. 7A). The plot indicates that the seismic $E_G/\sigma_n$ is a fraction (0.01-0.42) of the experimental energy $E_C$ (Fig. 7A). These fractional values fall in the expected range for [fracture energy]/[total earthquake energy] (Lockner and Okubo, 1983; Olgaard and Brace, 1983; Wilson *et al.*, 2005). We thus speculate that the experimental Coulomb energy density, $E_{C,}$ can provide a reasonable estimate of total earthquake energy, a quantity that cannot be determined from seismic data (Abercrombie and Rice, 2005; Kanamori and Rivera, 2006).

Here, we discuss the total energy in ELSE experiments and compare it to the fracture energy, $E_G$, that was determined from seismic data. We used the seismic analysis by Tinti *et al.* (2005), which they calculated the fracture energy associated with recent earthquakes in the moment-magnitude range of $M_W = 5.6\text{-}7.2$. They used slip- and velocity-histories of multiple sub-faults as determined from the inversion of strong ground motion, and applied crustal elastic properties to calculate (finite difference) the dynamic traction history for each of the sub-faults. The total earthquake work cannot be calculated from seismic data (Tinti *et al.*, 2005; Kanamori and Rivera, 2006), and Tinti *et al.* (2005) assumed an arbitrarily high ambient traction. They calculated the fracture energy (Kanamori and Rivera, 2006), $E_G$, (which they defined as 'breakdown work') as the surplus work done above the minimum shear traction, $\mu_{min}$, in their shear traction curves (Fig. 2B, C). Note that the minimum frictional strength in the work of Tinti *et al.* (2005) is defined similarly to $\mu_{min}$ in our analysis. The breakdown work (=fracture work), $W_b = E_G$, is the integrated value of [shear stress × slip velocity]; note that in our analysis MER = [shear stress × slip velocity]. The calculated breakdown work ranged $4 \cdot 10^5$ to $2 \cdot 10^7$ J/m$^2$ for analyzed earthquakes (Tinti *et al.*, 2005) (Tbl. 2).

Our analysis indicates that the total experimental slip, D, during an ELSE experiment, is proportional to the Coulomb energy density, $E_C = 0.605 \cdot D^{0.933}$, for both SWG and KD experiments (Fig. 7A). The seismic $W_b$ of Tinti *et al.* (2005) has to be divided by the relevant normal stress on the fault for two reasons: first, the breakdown strength of rocks is proportional to the normal stress (Coulomb criterion), and consequently, the breakdown energy calculated for the six earthquakes (Tinti *et al.*, 2005), $E_G$, is also proportional to the associated normal stress; second, we showed (Fig. 7A) that, the Coulomb energy density, $E_C=E_T/\sigma_n$, better represents the total energy for ELSE experiments. To calculate the $\sigma_n$ in the Tinti *et al.* (2005) analysis, we first assumed that the analyzed faults are vertical, and that the normal stress on them is controlled by the overburden weight of the rock column. Then, the earthquake's mean depth, h, is used to estimate the normal stress, $\sigma_n$, with two bounds (Tbl. 2). The upper bound is $\sigma_{nU}$ = [rock overburden pressure – groundwater pressure] = $(\rho_{rock} - \rho_{water}) \cdot g \cdot h$, where $\rho_{rock}$ and $\rho_{water}$ are the density of crustal rocks and water, respectively, and g is gravitational acceleration. The lower bound, $\sigma_{nL}$ is based on the Poisson's effect in which only part of the overburden is converted to normal stress on vertical plane, and $\sigma_{nL} = \sigma_{nU} \cdot (\nu/1-\nu)$ where $\nu$ is the Poisson's ratio. We plotted the ratios $W_b/\sigma_{nU}$ and $W_b/\sigma_{nL}$ (Tbl. 2), as the fracture energy ratio $E_G/\sigma_n$ as vertical black lines in Figure 7A.

| [a]Earthquake | [a]$W_b$ | [a]Average slip (m) | [b]Mean depth (km) | [b]Estimated normal stress | | [b]Normalized fracture energy (m) | |
|---|---|---|---|---|---|---|---|
| | (MJ/m$^2$) | | | $s_{nU}$ (MPa) | $s_{nL}$ (MPa) | $W_b/s_{nU}$ | $W_b/s_{nL}$ |
| **Imperial (1979)** | 1.82 | 0.6 | 5.25 | 89 | 27 | 2.00E-02 | 6.80E-02 |
| | 1.06 | 0.5 | 6.5 | 111 | 33 | 9.60E-03 | 3.20E-02 |
| **Landers (1992)** | 21.53 | 2.46 | 7.5 | 128 | 38 | 1.70E-01 | 5.60E-01 |
| | 14.91 | 1.88 | 7.5 | 128 | 38 | 1.20E-01 | 3.90E-01 |
| **Northridge (1994)** | 5.75 | 0.99 | 12 | 204 | 61 | 2.80E-02 | 9.40E-02 |
| **Morgan Hill (1984)** | 1.36 | 0.25 | 5 | 85 | 26 | 1.60E-02 | 5.30E-02 |
| **Western Tottori (2000)** | 1.69 | 0.99 | 9.25 | 157 | 47 | 1.10E-02 | 3.60E-02 |
| | 3.02 | 0.54 | 9.25 | 157 | 47 | 1.90E-02 | 6.40E-02 |
| | 2.73 | 0.55 | 9.25 | 157 | 47 | 1.70E-02 | 5.80E-02 |
| **Kobe (1995)** | 0.4 | 0.29 | 10 | 170 | 51 | 2.40E-03 | 7.80E-03 |
| | 0.97 | 0.42 | 10 | 170 | 51 | 5.70E-03 | 1.90E-02 |

**Table 2. Seismic and Energy Data**
Seismic and energy data for the six earthquakes analyzed by Tinti *et al.* (2005). Four of these earthquakes have more than one kinematic solution, and thus there are 11 separate solutions for their fracture energy. The presented values are the calculated averages for multiple sub-faults. The left three columns, marked by [a], are the original data from Tinti *et al.* (2005), and the right five columns, marked by [b], are calculated here as explained in text. The values of the fracture energy ratios (two right columns) are plotted versus the average slip (third column) in Figure 7A.

[a] After Tinti *et al.* (2005).

[b] This study.

### *Slip-Weakening Distance*

We now address the issue of critical slip-weakening distance, $d_C$, (Fig. 2B, C). In friction experiments, $d_C$ ranges from a few tens of microns in direct shear tests (Okubo and Dieterich, 1981) (Fig. 2A) to meters in rotary shear runs (Han *et al.*, 2010; Niemeijer et al, 2010; Reches and Lockner, 2010). Seismic analyses revealed that for large earthquakes, $d_C$ is on the order of meters (Ide and Takeo, 1997; Fukuyama *et al.*, 2003; Tinti *et al.*, 2005). In ELSE experiments, we identified $d_C$ as the first break in slope of the strength curve as marked in Figure 4C-D. The 49 ELSE runs that display significant dynamic-weakening reveal short $d_C$ (Fig. 7C), with mean values of 2.7 cm and 1.2 cm for SWG and KD, respectively ($d_C$ was not determined in runs with no or negligible weakening). These small $d_C$ values differ from previous analyses (Han et al., 2010; Niemeijer et al, 2010; Reches and Lockner, 2010) that reported $d_C > 1$ m for rotary-shear experiments and for seismic analyses (Ide and Takeo, 1997; Fukuyama *et al.*, 2003; Tinti *et al.*, 2005). Extremely intriguing is the fact that discrepancies between this study and the steady-state experiments by Reches and Lockner (2010) were conducted on the same rocks, on the same machine. We further discuss the source for this apparent discrepancy below.

## Impact Loading and Fault Weakening

The fault patch in ELSE experiments is loaded abruptly as it is connected to a spinning flywheel by a fast-acting clutch. We found that such impact loading has profound effects on fault-patch response. First, the friction-velocity relationships under impact loading differ from those relations under near-steady-state conditions. In ELSE experiments with SWG, the frictional strength is 0.6 to 0.8, for slip velocities below 0.1 m/s, and drops sharply to $\mu$ as low as 0.2 when $V > 0.1$ m/s (Fig. 8A). On the other hand, constant-velocity, steady-state experiments by Reches and Lockner (2010) exhibit fundamentally different friction-velocity relationships (Fig. 8B). This difference is particularly striking because both sets of experiments were conducted on the same rock samples with the same test apparatus. Thus, the dissimilarity in friction-velocity relations is attributed solely to the different loading mode. A few of the ELSE experiments did not undergo typical weakening and suggest that additional factors, such as starting fault surface condition, can contribute significantly to dynamic strength evolution. These effects will be examined in future experiments.

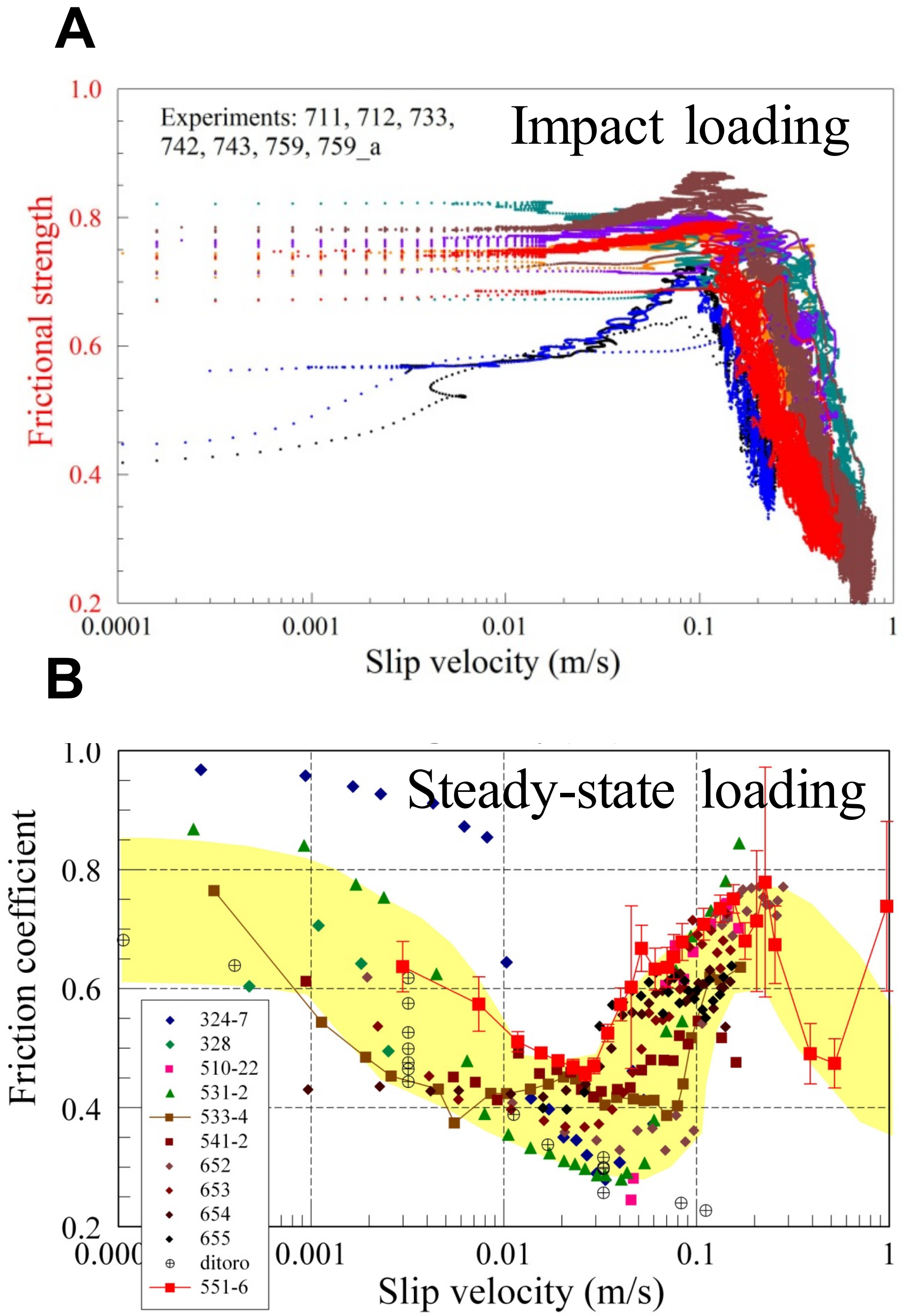

**Figure 8. ELSE vs. Steady-State Experiments**
Frictional strength relations to slip velocity in two sets of experiments that were conducted on the same samples of Sierra White Granite and on the same apparatus (Reches and Lockner, 2010). **A**: Friction-velocity relations for ELSE runs; note the fast weakening at $\boldsymbol{V > 0.1}$ m/s with friction drop of 0.1-0.3 per 0.1 m/s. **B**: Friction-velocity relations for steady-state experiments (10), that display weakening at V~ 0.01 m/s and distinct strengthening at V= 0.05-0.1 m/s. Note the striking difference with respect to the impact-loading relations in A.

Further, the slip acceleration during our impact-loading experiments varies systematically with the evolution of fault strength and wear rate (Figs. 9). The main features of these relations are:

1. The characteristic weakening distance, $d_C$, occurs within the initial acceleration spike, which has an amplitude of up to 25 $m/s^2$ and a duration of ~0.1 s;
2. A close temporal correlation appears between the evolution of acceleration (blue curve), strength (red curve), and wear-rate (black curve) (Fig. 9);
3. The dynamic weakening is restricted to the period of intense acceleration (Fig. 9).

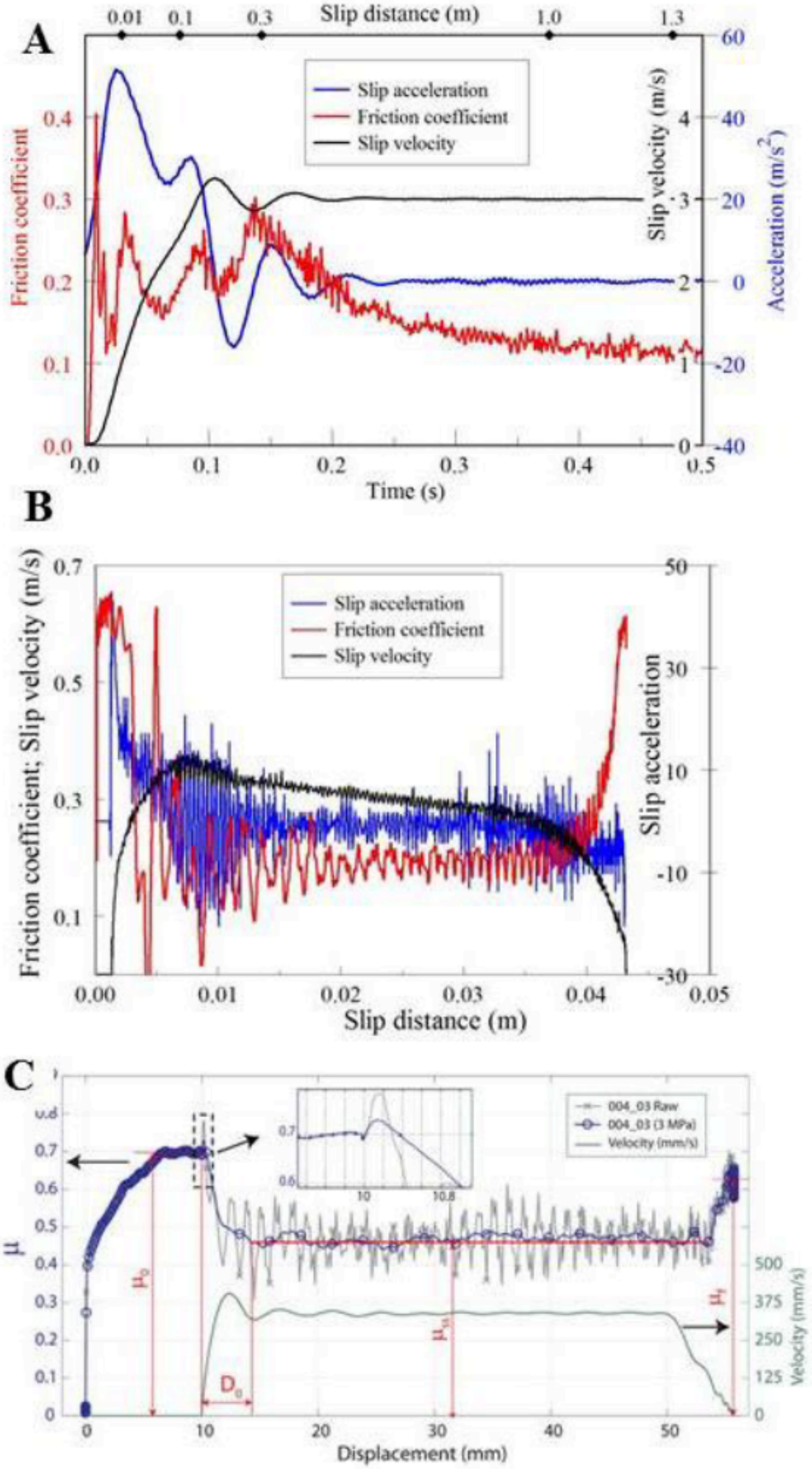

**Figure 9. Slip-Acceleration and Fault-Wear**
Slip acceleration (blue), strength evolution (red) and fault wear-rate (black) during the first 0.5 s of slip in one granite sample (A) and one dolomite sample (B).

These observations are not unique in ELSE experiments. Similar temporal associations between weakening and acceleration were reported in stick-slip experiments (Ohnaka and Yamashita, 1989) (Fig. 2A), rotary shear (Goldsby and Tullis, 2011) (Fig. 10), and impact shear experiments (Huang and Feng, 2006; Yuan and Prakash, 2008). These studies greatly differ from each other in apparatus, slip distance ($\mu$m to m), normal stress (a few to thousands of MPa), acceleration (a few m/s$^2$ to km/s$^2$), and slip-velocities (0.01 to 40 m/s). The outstanding commonality is impact loading that leads to intense slip acceleration.

What is the physical mechanism that could produce the weakening effect of slip acceleration? In ELSE experiments, the wear-rate during the initial few millimeters of slip was extremely high (Fig. 9), approaching $10^4$ $\mu$m/m in some runs. These wear-rates were probably activated by the high strain rates generated by the flywheel impact. The main reason is that high strain-rates significantly increase rock brittleness (Heard, 1963) and fracture tendency (Freund, 1990), and it was shown (Grady and Kipp, 1985; Reches and Dewers, 2005) that impact-loading generates extreme strain-rates of $\sim 10^4\ \mathrm{s}^{-1}$. The product of this intense wear is a layer of fine-grain powder (gouge) that reduces the fault strength by powder-lubrication (Heshmat, 1995; Wornyoh *et al.*, 2007; Han *et al.*, 2010; Reches and Lockner, 2010; Sammis *et al.*, 2011). Thus, impact loading accelerates fault-wear and gouge formation, and by doing so quickens weakening and shortens the weakening distance, $d_C$. However, while acceleration quickens the weakening, the acceleration intensity does not affect the value of the steady-state friction that follows the initial stage (Niemeijer *et al.*, 2010).

Another mechanism was recently proposed (Goldsby and Tullis, 2011) for rotary-shear experiments with accelerations < 40 m/s$^2$, and slip-velocities < 0.36 m/s. These experiments revealed similar acceleration-weakening relations to ELSE experiments (compare Fig. 9A), and similar friction-velocity relationships. The results were attributed (Goldsby and Tullis, 2011) to 'flash heating' at highly stressed contacting asperities (1-25 $\mu$m in size) with good fit to flash heating predictions (Yuan and Prakash, 2008; Goldsby and Tullis, 2011). Goldsby and Tullis (2011) also found "...that a very thin layer of gouge [≤30 μm thick] formed on the initially bare rock surface." We propose a different interpretation for these experiments. First, the ≤ 30 $\mu$m gouge thickness indicates an intense, average wear-rate of ≤ 700 $\mu$m/m, during the 43 mm of slip. We suspect that the wear-rate was much higher during the initial slip-acceleration (Figs. 8 and 9). Second, a ≤ 30 $\mu$m thick gouge layer would cover the initially contacting asperities along the bare surface, and thus decrease (or eliminate) their extreme high stress. Third, slip on the experimental fault is likely to be accommodated within the newly formed gouge layer, and not by shear between bordering asperities. We think that our model of the acceleration-driven wear-rate and associated powder-weakening better explains the observations in the work of Goldsby and Tullis (2011).

The process of accelerated weakening is likely to be active in natural earthquakes, in which fault-patches are intensely accelerated by the passing rupture front (Andrews, 2005; Reches and Dewers, 2005), and steady-state friction is not likely to be achieved (Tinti *et al.*, 2005; Reches and Lockner, 2010). Further, slip-acceleration can explain some puzzling observations. For example, tiny earthquakes ($\mathrm{M_W} = -2.7$ to

$-3.4$) have the seismic signature of large earthquakes (Boettcher *et al.*, 2009; Yabe *et al.*, 2009), but with only tens of microns slip, these earthquakes cannot reach the typical seismic $d_C$ (Tinti *et al.*, 2005). On the other hand, accelerated weakening can well-explain the instability of these tiny earthquakes.

## Summary

We propose that the ELSE approach is a reasonable simulation of fault-patch behavior during large earthquakes. In terms of loading, the experiments and earthquakes are analogous: in both cases, a finite amount of energy density (kinetic or elastic) is applied abruptly (flywheel engagement or rupture front) to a fault patch. In the experiments, however, the energy is directly related to the flywheel velocity, which controls the resulting peak-velocity of the experimental patch, whereas earthquake slip-velocity has a non-trivial relationship to the released elastic energy (Andrews, 2005). Simulating the latter condition was achieved in stick-slip experiments (Okubo and Dieterich, 1981; Lockner and Okubo, 1983; Ohnaka and Yamashita, 1989; Huang and Feng, 2006); however, those experiments were limited to very small slip, equivalent to $M_W < -4$. Those slip events may simulate earthquake nucleation, but fall short of the mechanical power (Di Toro *et al.*, 2011) and slip-magnitude of larger earthquakes. Currently, the ELSE approach is the only method to experimentally simulate large earthquakes.

Our experimental analysis suggests that large earthquakes have the following properties: (1) steady-state friction or velocity is not likely to be attained (Fig. 4); (2) the total slip along a fault-patch can serve as a good estimator for its average dynamic strength (Fig. 7B); (3) the average slip during an earthquake is a good estimate of the earthquake energy density (divided by normal stress) (Fig. 7A); (4) the rapid acceleration associated with the earthquake rupture intensifies slip-weakening and shortens the weakening-distance (Fig. 7C and 9).

# Chapter 3: Seismic Tomography of Tangshan, China

## Preface

This chapter is part of a research project led by Dr. Randy Keller, Dr. Steven Harder, and a team of Chinese colleagues to determine the 3D structure of the Tangshan basin. My part included leading the group from University of Oklahoma, and training the OU participants and our other colleagues on field deployment and data collection. I processed, analyzed, modeled, interpreted the data, and prepared this report.

## Abstract

On 28 July 1976, Tangshan, China had a M7.5 earthquake that caused widespread devastation in city and surrounding areas, and upwards of 250,000 fatalities. Today, 7.5 million people reside in this seismically active area, yet the geology beneath the Tangshan region is poorly known. Thus, we conducted a 3D refraction seismic investigation that covered a 40 x 60 km area centered on the city. Our tomographic analysis shows that most of Tangshan area is underlain by a large basin, approximately 1.5 km deep, with smaller fault-bound sub-basins that subside 0.5 km deeper than the major basin. The analysis also suggests that a zone of multiple major faults, which is about 20 km wide could underlie the city.

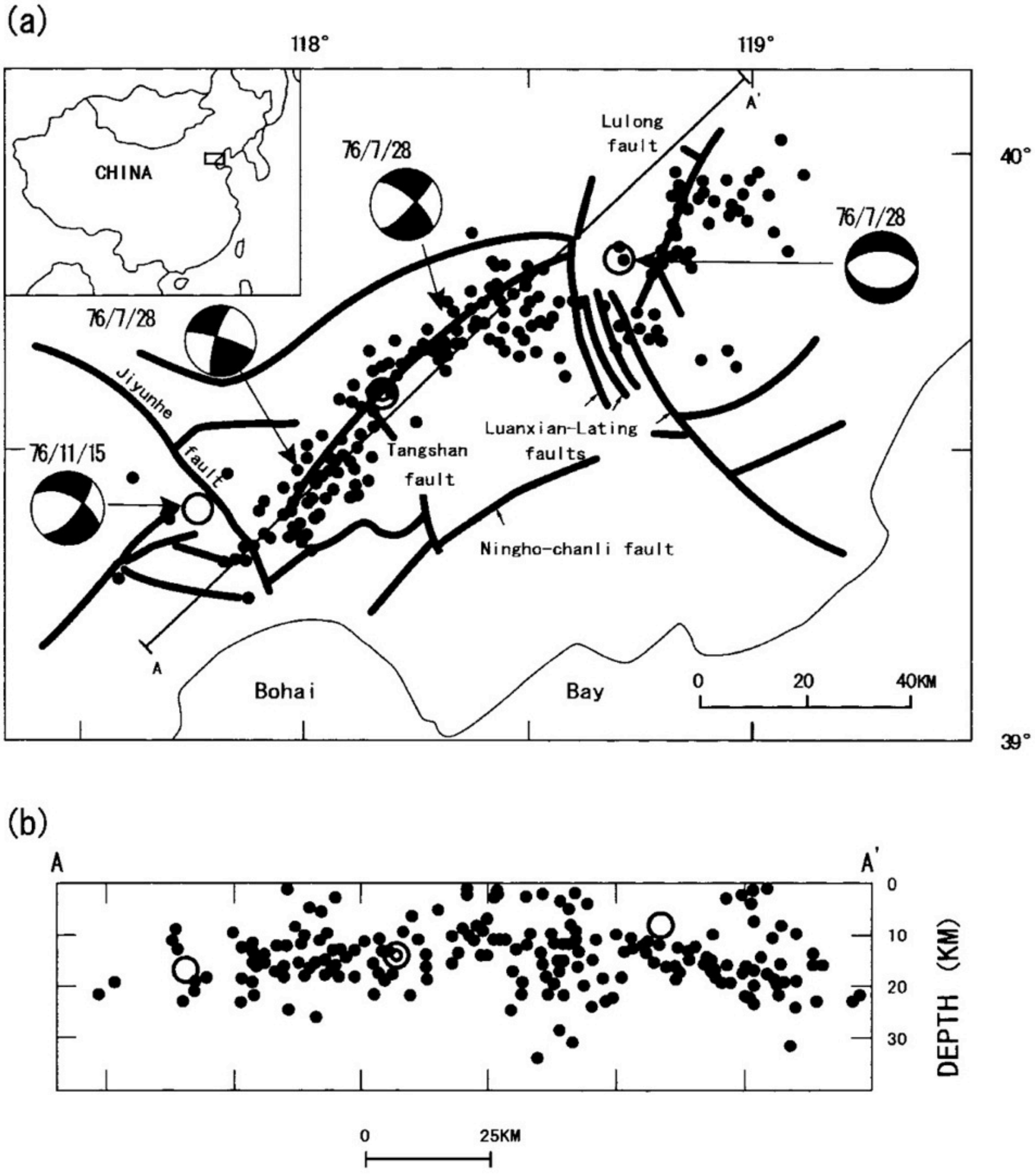

**Figure 10. The 28 July 1976 M7.5 Tangshan Earthquake**
Historic regional seismicity of Tangshan, China (from Huang, 1997). (a) Inset map shows the location of the main map (black box). Map shows the mainshock from the M7.5 Tangshan earthquake (concentric circles), two large aftershocks (open circles), the epicentral distribution of aftershocks (black dots), and faults (thick black lines), along with focal mechanisms from events in the sequence. (b) Cross-section view from A-A' drawn on Figure 10a, and shows the depth distribution of the seismicity using the same symbology as the map.

## Introduction

The major city of Tangshan is located in a seismically active area of northeast China, near the northern edge of the Bohai Bay basin (Fig. 10). The region has experienced, both, Cenozoic extension and strike-slip tectonism (Allen *et al.*, 1998), which is exhibited by the 1976 Tangshan earthquake sequence. Right-lateral faulting produced the $M_W$ 7.5 mainshock, which occurred in the morning of 28 July 1976 along the Tangshan fault, and was followed by several large aftershocks that lasted until December 1976. Strong shaking (Modified Mercalli Intensity > VI) from the main earthquake occurred over hundreds of kilometers away from the epicenter. Two prominent aftershocks that slipped along conjugate strands of the Tangshan fault system, an extensional $M_W$ 7.0 later that day, and a transtensional $M_W$ 6.4 on 15 November 1976, further devastated the region. The 1976 earthquake in Tangshan, China ranks as one of the deadliest earthquakes in the 20th century, with over a quarter of a million people fatalities. The casualty level is high for an earthquake of $M_W$ 7.5 and reflects poor housing construction and the possible amplification of ground motion by thick sediment fill in the basin underlying the city (Fig. 9).

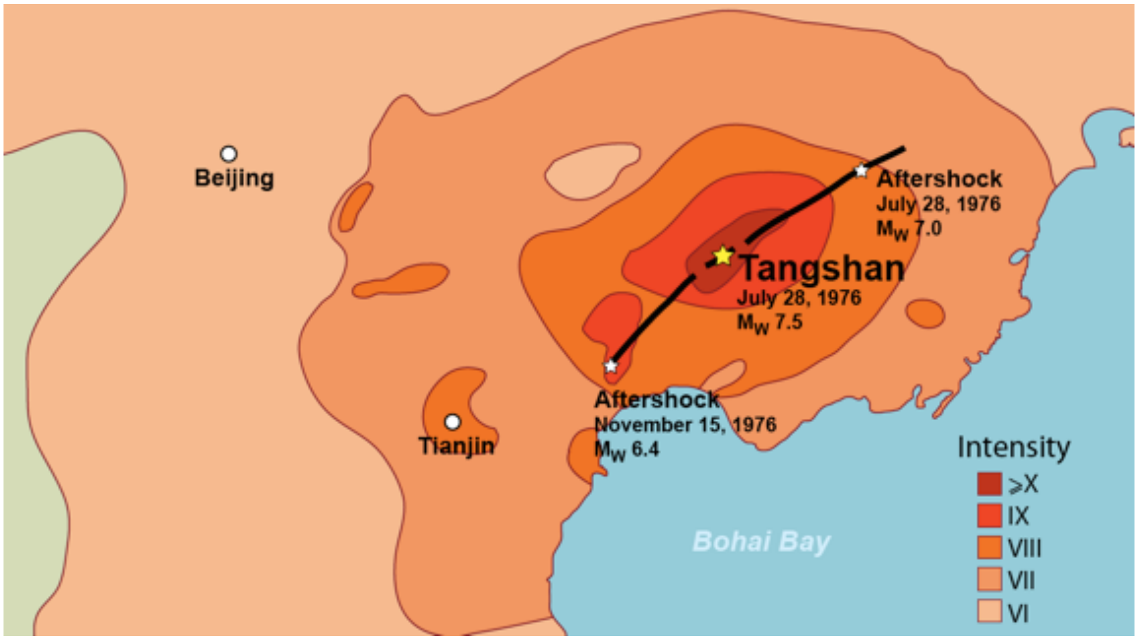

**Figure 11. Modified Mercalli Intensity for the Tangshan Earthquake**
Estimated Modified Mercalli Intensity (MMI) distribution from the M7.5 Tangshan earthquake. Modified from Fang (1979).

The city of Tangshan has since been rebuilt, but the subsurface geology is still poorly mapped. To address this issue, we deployed a three-dimensional (3D) tomographic survey (Fig. 12) to elucidate the vertical and lateral extent of the sedimentary fill, and to delineate subsurface structures, which might correlate them with known surficial geology. This study was done with the support and collaboration of the Chinese Earthquake Administration and the results will be used to model predicted ground motion and mitigate the hazards of future earthquakes. The goal is to image the subsurface structures beneath Tangshan.

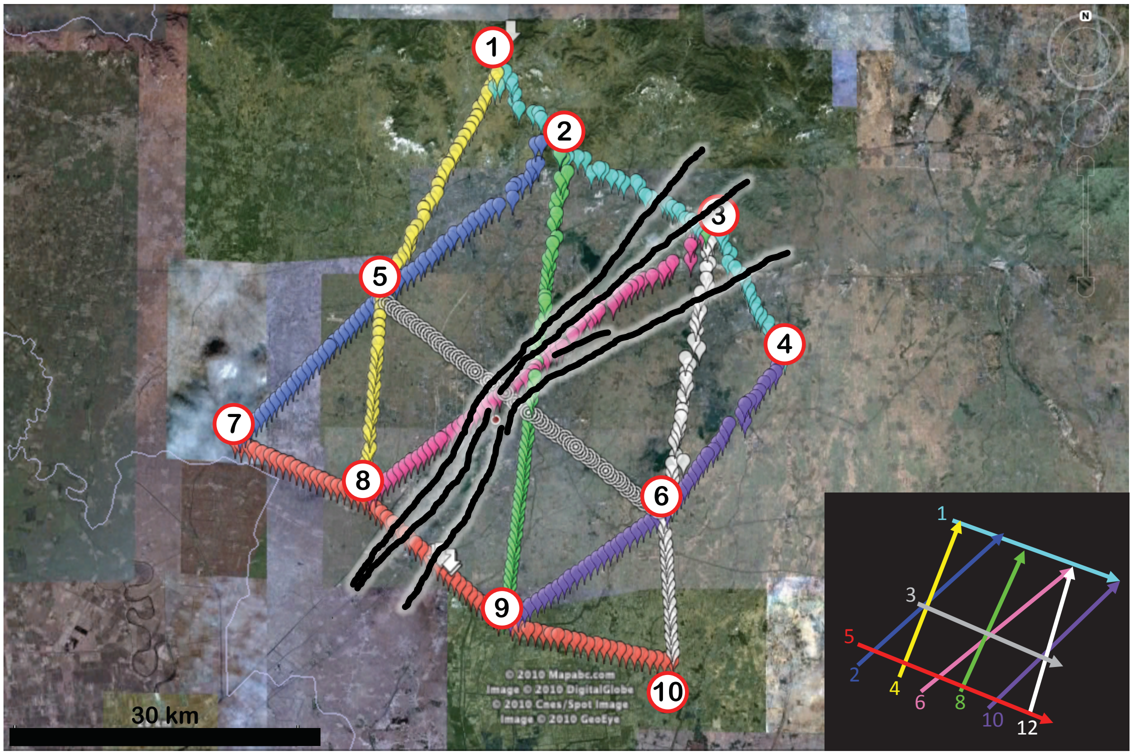

**Figure 12. Tangshan 3D Seismic Survey Geometry**
Study area (plotted on Google Maps), showing mapped faults (bold black lines), receiver locations (colored point symbols), and shot point locations (circles with numerals). Inset shows line numbers references in the text, and other figures throughout the paper.

## Field Operations

The seismic survey, which was conducted in January 2010, deployed 425 REFTEK 125A ("Texan") recorders at 500 m spacing, in an area approximately 40 km x 60 km centered on the city of Tangshan (Fig. 12). The operating team included two researchers and six students from the University of Oklahoma (OU); two researchers from the University of Texas at El Paso; and 18 researchers from the China Earthquake Administration, Chinese International Search and Rescue Team, and National Earthquake Response Support Service. I trained and led the deployment team, comprised of OU students and 18 local researchers. Galen Kaip (UTEP) and I programmed the Texan recording windows. Randy Keller (OU) and Steve Harder led the seismic source (explosives) team. The 3D survey comprised nine seismic refraction profiles: Lines 1, 3, 5 were perpendicular (northwest-southeast) to three mapped faults; Lines 2, 6, 10 were trending northeast-southwest; and Lines 4, 8, 12 were trending roughly north-south. A number of different sources, 20 altogether, were fired during the two-day listening window, which include our large shots, smaller explosive shots from a co-spatial reflection survey, blasts from nearby quarries, and a small (M<1) earthquake. The survey was designed to allow to record every source by every receiver, and thus providing dense raypath-coverage.

## Data Processing

The two-dimensional (2D) seismic data were cut to 60-second sections, starting from the shot times shown in Table 1, then modeled using the 3D inversion algorithm of Hole (1992), which is a modified version of the Vidale (1990) code, to allow for stable solutions with high, lateral velocity contrasts in the 3D tomographic model. Input to the Hole algorithm included: (1) the first arrival travel times, (2) an initial 3D velocity model, (3) source parameters, (4) station coordinates, and (5) framework script commands. Output from the algorithm is a new 3D model of velocities, using the finite difference method to achieve the best fit between calculated and observed travel times. The depth-resolution of this method is limited to the upper 10 km, due to the relatively short maximum source-receiver offsets in the array. To illuminate deeper structures of mid- to lower-crustal depths and the Mohorovičić discontinuity (Moho), I integrated reflection seismology techniques into a forward modeling workflow.

The raw 2D shot gathers had moderate signal-to-noise ratios (SNR), which were improved with minimal seismic processing in ProMAX for first arrival picking (Fig. 13). Processing was kept to a minimum to avoid introducing seismic artifacts that may introduce unwanted residual noise to the data, such as seismic phase shifts that affect the picked arrival times. Each shot gather across all the stations in the array was grouped into line gathers to correlate arrivals with the interlocking line geometry (Fig. 12). Spectral analysis on individual line gathers yielded frequency distributions, which were used to optimize the SNR using a bandpass filter. Later phases on the seismic gathers were identified using an automatic gain control (AGC) window of 2000 ms. These later arrivals could be not included in the 3D tomographic inversion, because the tomography only includes diving wave first arrivals. However, the later arrivals were employed in the forward modeling discussed below.

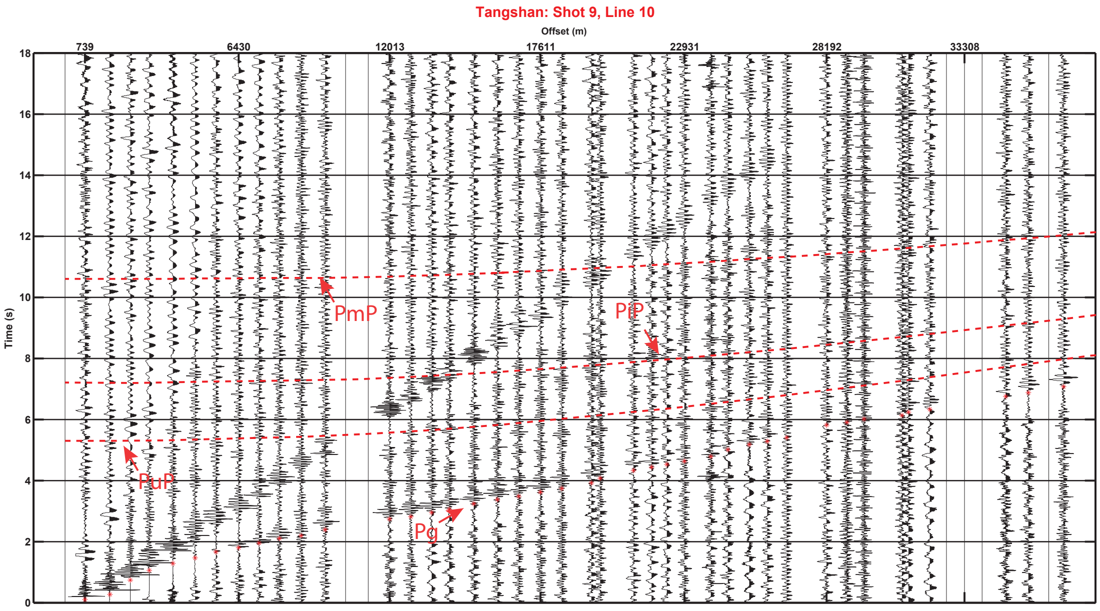

**Figure 13. Typical Seismic Data from the Tangshan Survey**
Shot-gather plots of refraction seismic lines referenced in Figure 12 inset. Time is on the y-axis (increasing up) vs source-receiver offset on the x-axis. Manually picked first arrivals are shown in asterisks (*), and theoretical reflected phases are plotted as dashed lines.

### *3D Modeling*

The first arrival picks in Figure 13 (Pg phase) were used as input for the tomographic inversion. The starting model was a 3D velocity volume consisting of 1 km$^3$ voxels that was constructed from 1-D modeling of the entire set of picked first arrival travel times. The 3D model space extends from 5 km above to 40 km below sea level. It also and extends to 10 km beyond the actual the survey perimeter. This model-padding is necessary to avoid rays encountering the edge of the model, where no defined velocity exists, which would create singularities and spurious results. The algorithm was executed a total of thirty iterations to obtain the final velocity model: six times per set of averaging and smoothening windows, with five sets of windows that progressively refined the resolution of the model.

### *2D Modeling*

To image deeper parts of the crust, I employed 2D forward modeling utilizing the MacRay ray-tracing software (Luetgert, 1992). The initial crustal velocity profile was taken from Li *et al.* (2006), which places the Moho at 32 km depth, and contains a low-velocity layer within the lower crust. The upper 5 km of the 2D ray-trace model (Fig. 14) was constrained by the 3D tomography results (Fig. 15). A bulk average of the relatively thin uppermost layer was used to simplify the model calculations and results.

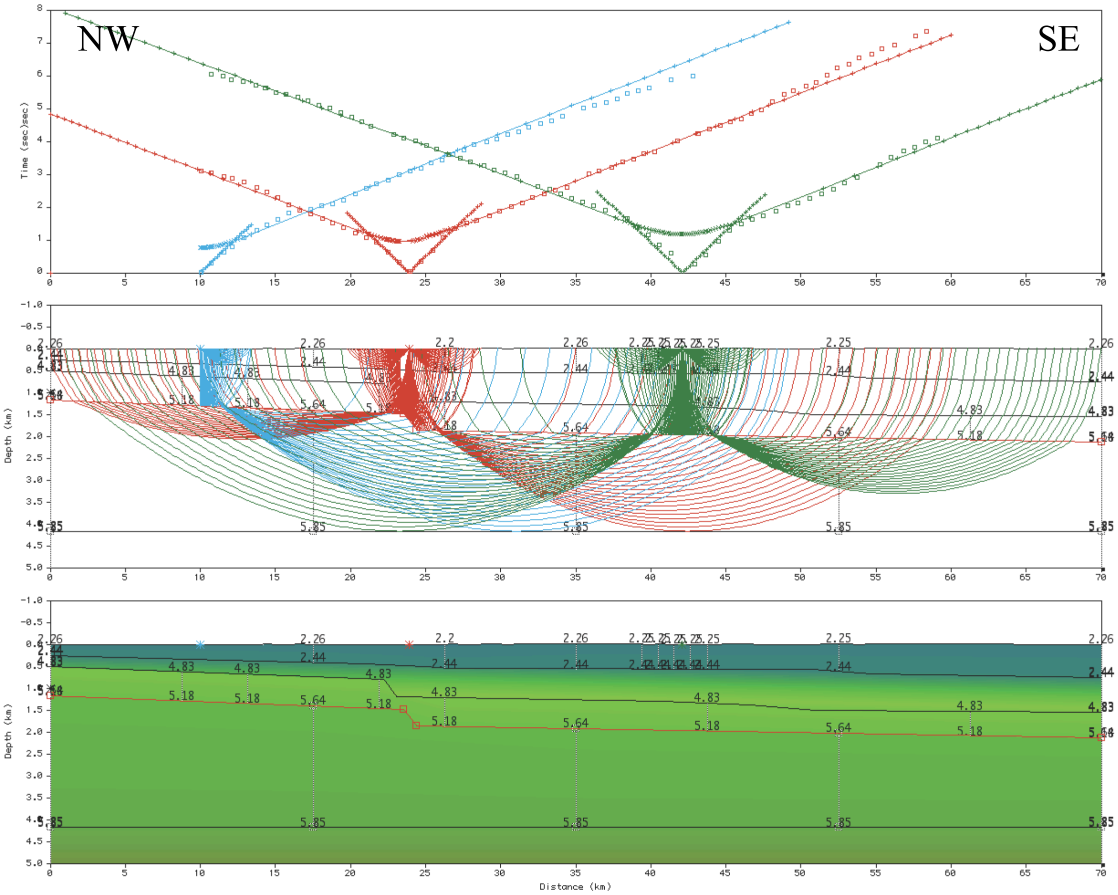

**Figure 14. 2D Forward Raytracing Model Across the Study Area**
Top shows the Pg phase picks (squares) and the calculated seismic travel times (lines). Middle shows the probable ray paths from shot to receivers. Bottom shows the 2D velocity gradient used in the raytracing model, with velocities in km/s.

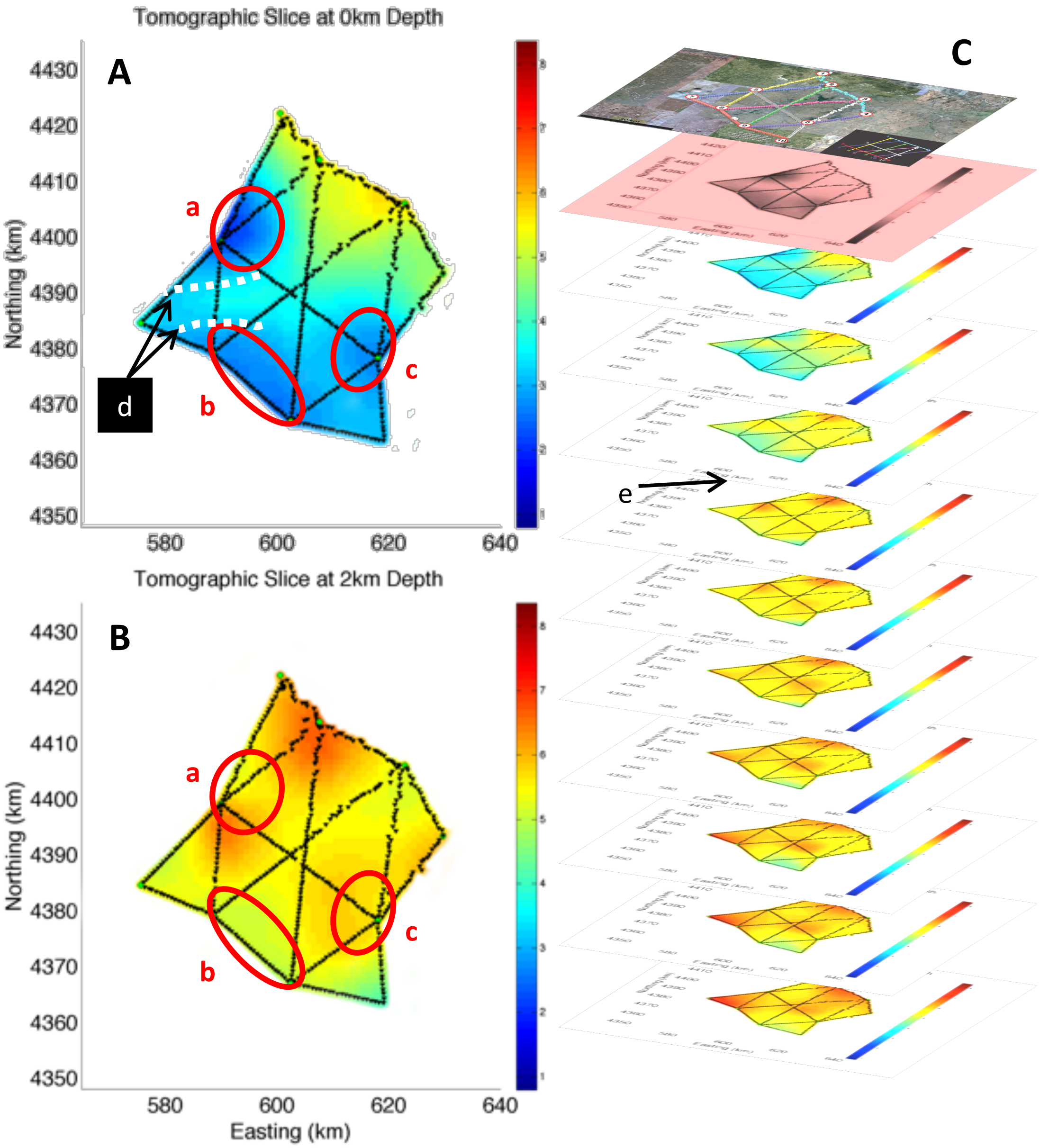

**Figure 15. Horizontal Depth Slices of the Tomography Volume**
Horizontal depth slices of the seismic tomography volume, at the surface (A), at 2 km depth (B), and every 0.5 km from the surface to 5 km down (C). Colorbar shows seismic P-wave velocity gradient in km/s, and are consistent across the figure. Red circles in A and B indicate interpreted sub-basin (a,b, and c), from the surface (0 km) velocity slice. White dashed lines (d) indicate relatively sharp lateral velocity contrasts. Vertical velocity contrast (e) shows the transition where slower than 5 km/s velocities are no longer visible.

### *Visualization*

Model visualization and interpretation were done using a custom-developed MATLAB graphical user interface (GUI), called Digitize Raster Slice (DRSLICE). The output velocity model from the 3D tomography is a 32-bit binary file. The file was converted into double precision rational numbers, gridded, and spatially referenced within DRSLICE. The GUI displays longitudinal, latitudinal, and horizontal cross-sections quickly and precisely. Accessory MATLAB scripts were written to visualize and contour off-axis cross-sections.

## Synthesis: Subsurface Structures and Fault Zones

The two-dimensional raytracing showed that the two-way travel-time (TWTT) at zero-offset is about 10.5 s beneath the central uplifted block (Fig. 14). TWTT delays of up to 1 s were calculated for the outlying basins, which may signify an overestimate of the thickness of sedimentary layers. The TWTTs were calculated for a fixed Moho depth of 32 km (velocity model of Li *et al.*, 2006), yet it is possible that the Moho shallows to the southeast of the Tangshan area, but we could not assess such perturbations due to the short aperture of the survey.

The seismic tomography aligns well with observed basement outcrop to the north of the study area, in terms of location and seismic velocity of 5-6 km/s. The results indicate that the sedimentary cover generally thickens to the southwest, with relatively high velocities in the center of the study area (~4 km/s), bound laterally by sharp decreases to low-velocity of 2.2-2.45 km/s in the marginal areas of the survey (Fig. 15; white dashed lines). I interpret the central high velocities as possible pop-up structures from constraining-bends or -steps of major right-lateral strike-slip faults that extend across the city (Fig. 16). These pop-up structures reasonably correlate with mapped faults within the survey (Fig. 12). I interpret the marginal low-velocity zones as low density sedimentary fill. As the seismic station spacing of 500 m limits the lateral tomography resolution, the sharp lateral velocity contrasts between the center of the study area and marginal areas may be even narrower than indicated by the model.

The study area is best described as a broad low-velocity zone (broad regional basin) with seismic velocities of 2.2-2.45 km/s. The basin approximately covers an area of 45 km x 25 km, and sediments are no more than 1.5 to 2 km thick and likely averages only 0.5 to 1 km thick in most places. The areal extent of the broad basin presented here is a lower-bound estimate, since the basin appears to extend beyond the seismic survey footprint. Within the study area, I imaged at least three localized low-velocity zones in the northwest, southwest, and southeast, having an areal extent of 80 $km^2$, 140 $km^2$, and 70 $km^2$, respectively (Fig 15A). Also within the study area are strips of relatively higher-velocities separate the smaller pockets of low-velocity zones (Fig. 15A).

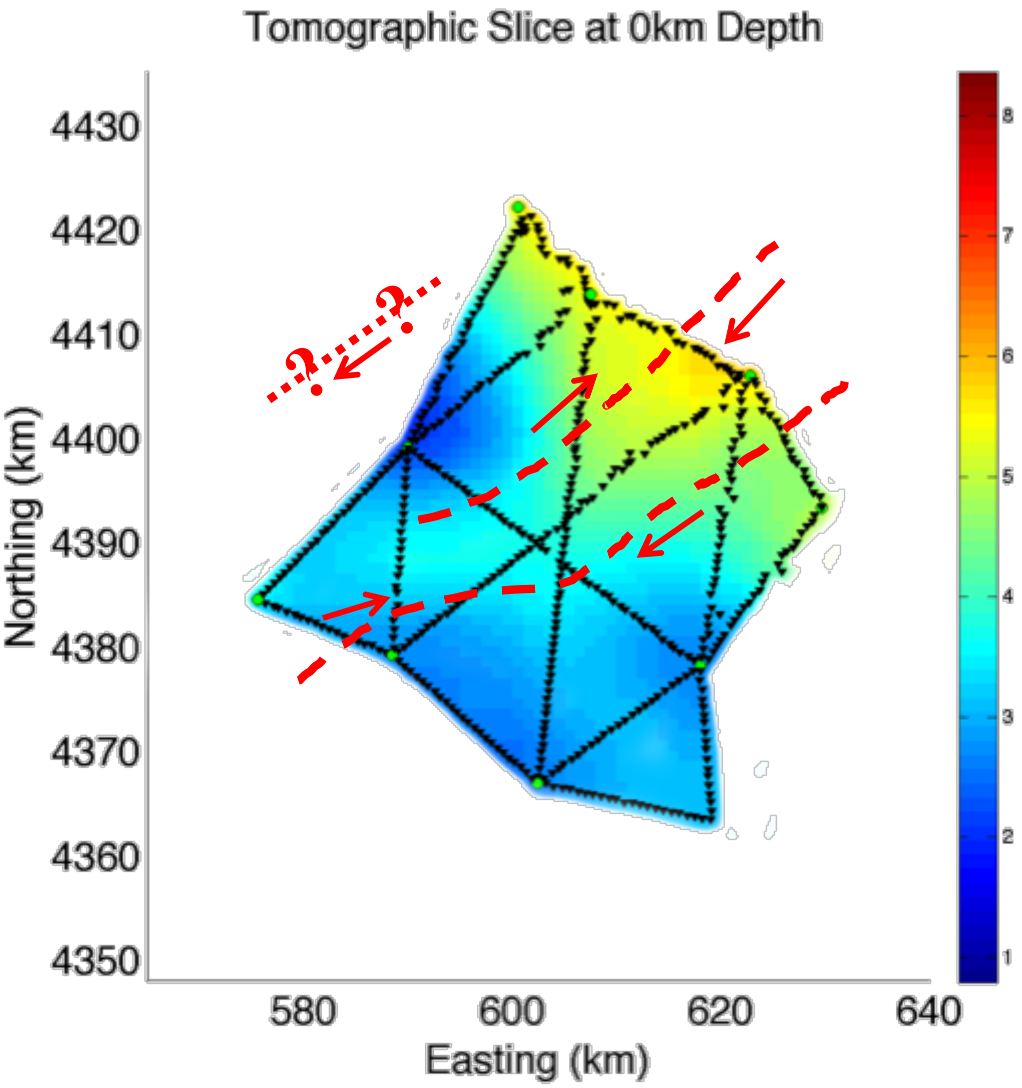

**Figure 16. Fault Interpretation from the Tomography Model**
Fault interpretation on the surface (0 km) slice of the velocity model. Left-stepping right-lateral faults (red dashed lines) may produce pop-up structures within the transpressional zone. Smaller sub-basins imply that there might be right-stepping fault geometries might be inferable (red dotted line with question marks).

## Discussion

### *Geologic Implication of the Tomography Results*

The 3D tomography revealed bimodal basins around the Tangshan area that is about 1.5-2 km thick (Figs. 13 and 14). There exists a broad low-velocity basin that thickens to the south, and extends beyond the study area, towards Bohai Bay. The results indicate that this broad basin is approximately 1.5 km thick that can be attributed to the regional subsidence observed in the Bohai Bay transtensional setting (Allen *et al.*, 1998). The modelled low-velocities of 2.2-2.45 km/s are typical of low density, unconsolidated, sedimentary deposits. This observation is consistent with the geomorphology of the area, as sediments migrate from the observed outcrops to the north, towards the Bohai Basin to the south. Within the broad basin are local, smaller sub-basins that have seismic velocities similar to the broad basin, but they locally extend up to 500 m deeper than the broader basin (Fig. 15).

The immediate area of Tangshan city is structurally high-standing based on the relatively high velocities (~6 km/s) observed at depths as shallow as 1.5 km. This high-standing block, trending roughly east-west, has a prominent velocity contrast with the overlying sediments at a depth of 1 km, where surficial deposits (2.3 km/s) transition sharply to a high-velocity basement (~6 km/s). This vertical contrast (Fig. 15C) is similar to the contrast with its lateral contrast, discussed earlier, but is less constrained in depth due to the lower depth-resolution of the model (0.5 km).

### *Structural Complexity*

The broad basin studied here is at least 1,125 km$^2$ in area with three smaller sub-basins. The broad basin extends beyond the southern and western edge of the study area, and is likely larger than what is shown here, due to the proximity of known depositional centers, like the Bohai Bay. Sharp velocity-transitions suggest that the smaller sub-basins are fault-bound. The velocity model shows some complexity in relation to known fault-motion and geometry of the main Tangshan fault, as the high-standing block shown in Figure 15A is trending orthogonally with the expected compressional zones in the Tangshan fault geometry. This compressional trend suggests that local fault strands may anastomose to form confined pull-apart basins and pop-up structures. Local fault bends and steps may have created the localized high- and low-velocity zones resolved in the tomography (Figs. 15 and 16). The different depths of the broad basin and the small sub-basins suggest that at least two modes of subsidence exist in the area, (1) a broad regional subsidence and (2) a more localized subsidence, but the timing of these episode cannot be resolved by this study.

### *Implications with Respect to Earthquake Hazard*

The extreme intensity (MMI > X) from the moderately strong M7.5 Tangshan earthquake could be attributed to site amplification of the poorly consolidated sediments beneath the city. Unreinforced buildings also likely contributed to the very high casualty rate. Although earthquakes of this magnitude in this area are rare, it is still an active tectonic region (NEIC earthquake catalog, accessed 2017).

## Summary

1. The 3D seismic survey revealed a 1.5-2 km low-velocity zone beneath the city of Tangshan. This zone is approximately a 45 km x 25 km area, and it is interpreted as a sequence of low-density sedimentary rocks.

2. At least two modes of subsidence are recognized: subsidence of a large basin that extends beyond the study area, and smaller sub-basins, which form small, deep sediments beneath parts of the city. The structural relationship between the two modes could not be identified in this study.
3. Sharp velocity contrasts across the model suggests that multiple fault splays exist across the velocity model, i.e., beneath the city of Tangshan. There may be buried faults distributed over a 40 km swath, which is a larger spread than the 10-14 km band of mapped surface faults.
4. The present results can serve as preliminary structural indicators as the survey resolution is limited in breadth and station spacing. A smaller spacing between seismic sensors would better define the boundaries lateral boundaries between low- and higher-velocity areas, while a broader survey would deepen the seismic ray penetration.

# Chapter 4: Seismological Observations in Oklahoma 2010-2017[2]

## Preamble

I succeeded Dr. Austin Holland in managing the Oklahoma regional seismic network and its local subnets, and leading the OGS seismic initiatives since late-2015. I transitioned Dr. Jake Walter into the Oklahoma State Seismologist from late-2016 to early-2017. I, along with Drs. Xiaowei Chen and Nori Nakata, greatly improved the seismic monitoring effort in Oklahoma, and trained a field technician and numerous students how to deploy telemetered seismic monitoring stations—this resulted in a four-fold increase in real-time data, which is critical for mitigating human-activity induced earthquake. Under my guidance, seismic analysts located earthquakes and determined fault plane solutions. I participated in a UNAVCO-led team that installed the permanent GPS stations in Pawnee and Osage counties to monitor crustal deformation. I generated all the texts and figures within this manuscript, unless otherwise noted.

## Abstract

The escalation of Oklahoma earthquake activity, in both number of occurrences and in areal extent, during the past five years, prompted an increase in seismic monitoring efforts in the region. My analysis, based on the enhanced Oklahoma seismic monitoring network for the period of 2010-2017, shows an increasingly detailed pattern of seismicity. Starting with less than 10 seismic stations prior to 2010, I helped deploy over 60 additional seismic stations, supplemented by approximately 40 more stations from other regional monitoring institutions. This expanded network operation provides

---

[2] The research described in the chapter was partly published as yearly seismicity reports by the Oklahoma Geological Survey (2015 and 2016), and my contributions to the publication of Chen *et al.* (2016), Fielding *et al.* (2016), and Walter *et al.* (2016).

well-located earthquake hypocenters that I use to derive three-dimensional seismogenic fault surfaces that become part of the Oklahoma Fault Database. The spatiotemporal correlation between oil and gas production-related activity and seismicity follow two different time lags. I observe an approximately two-year lag of when prolific seismic activity begins after oil and gas production ramps up in the Hunton dewatering and Mississippi Lime plays in central and northcentral Oklahoma, respectively. The timing with hydraulic fracture stimulations is signifficantly shorter, typically either during the stimulation stages or within days of well-completion. In a case study of the M5.8 Pawnee earthquake, my analysis leads to a new hypothesis of top-down fault-slip propagation as a measurable tracer of induced seismicity.

## Introduction

### *Tectonic Setting*

Oklahoma sits in the middle of the North American craton, far away from major plate boundaries. The Oklahoma crust has numerous faults in the Precambrian crystalline basement, with some extending up through the Paleozoic sedimentary strata (Marsh and Holland, 2016) due to its geologic history. Though considered tectonically stable, Oklahoma is not structurally dormant nor seismically quiescent. The largest and most documented Holocene fault scarp east of the Colorado Rockies is in Oklahoma, the Meers fault, which generated an estimated M7 earthquake when it last slipped 1100-1300 years ago (Crone and Luza, 1990).

### *Seismic Activity and Probabilistic Hazard*

Oklahoma has gone through a period of seismic renaissance in the past few years. Oklahoma went from experiencing an average of less than three M3+

earthquakes per year before 2010 to over 900 M3+ earthquakes in 2015 alone (Fig. 17; Tbl. 3). Furthermore, moderate M5+ earthquakes in Oklahoma are rare, with the M5.5 El Reno earthquake in 1952, followed by the M5.7 Prague 2011 earthquake—almost 60 years later. In 2016, Oklahoma experienced three M5+ events within a few months of each other: the 13 February M5.1 Fairview earthquake; the 03 September M5.8 Pawnee earthquake; and the 07 November M5.0 Cushing earthquake. This rate of increase has prompted the USGS to supplement long-term (50-year) probabilistic seismic hazard maps for the conterminous United States (e.g., Petersen *et al.*, 2015) with short-term yearly probabilistic hazard maps Central and Eastern United States (CEUS) (e.g., Petersen *et al.*, 2016 and 2017).

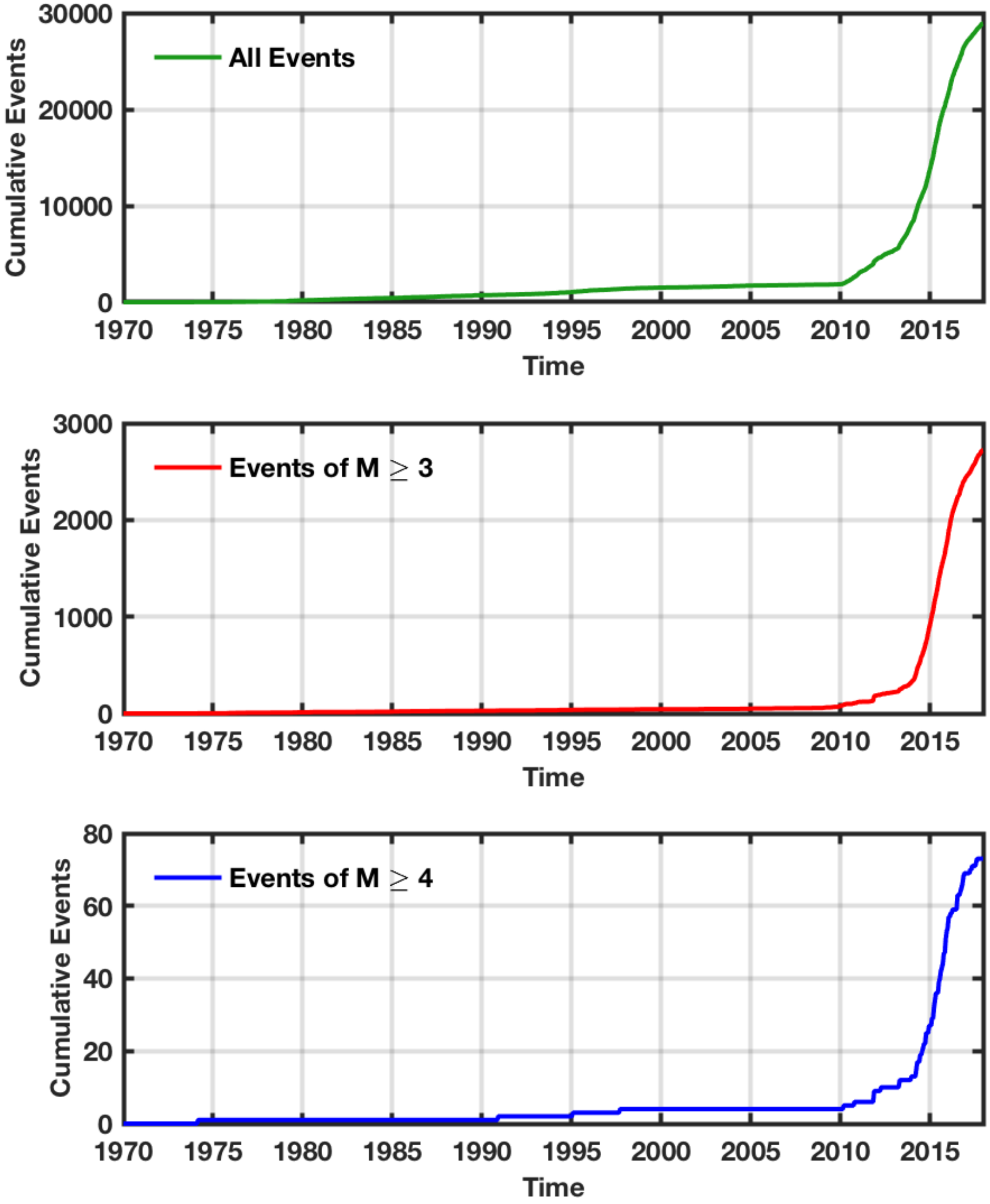

**Figure 17. Oklahoma Seismicity from 1970 to 2017**
Cumulative count of earthquakes in the Oklahoma Earthquake Catalog starting from 1990 to 2017. We observe seismicity rates begin to ramp up in the beginning of 2010 for all events, which is mimicked by counts of M3+ and M4+ earthquakes.

| Time Period | M2.5+ | M3+ | M4+ | M5+ |
|---|---|---|---|---|
| 1970-01-01 to 1979-12-31 | 47 | 12 | 1 | 0 |
| 1980-01-01 to 1989-12-31 | 74 | 15 | 0 | 0 |
| 1990-01-01 to 1999-12-31 | 80 | 16 | 3 | 0 |
| 2000-01-01 to 2009-12-31 | 88 | 34 | 0 | 0 |
| 2010-01-01 to 2010-12-31 | 124 | 41 | 2 | 0 |
| 2011-01-01 to 2011-12-31 | 234 | 67 | 3 | 1 |
| 2012-01-01 to 2012-12-31 | 124 | 35 | 1 | 0 |
| 2013-01-01 to 2013-12-31 | 362 | 110 | 3 | 0 |
| 2014-01-01 to 2014-12-31 | 1991 | 579 | 14 | 0 |
| 2015-01-01 to 2015-12-31 | 3314 | 903 | 27 | 0 |
| 2016-01-01 to 2016-12-31 | 2189 | 624 | 15 | 3 |
| 2017-01-01 to 2017-12-04 | 970 | 283 | 4 | 0 |

**Table 3. Oklahoma Seismicity from 1970 to 2017**
Decadal (1970-2009) and yearly (2010-2017) Oklahoma seismicity count (data from the Oklahoma Earthquake Catalog).

### *Induced vs. Tectonic Seismicity*

The dramatic increase in seismicity rate in Oklahoma from recent years is globally unprecedented. Although Oklahoma has tectonically triggered earthquakes, it is widely envisioned that the bulk of the recent seismicity in the state are likely due to subsurface injections associated with the oil and gas industry, either by hydraulic fracturing (e.g., Holland, 2013) or wastewater fluid disposal (e.g., Ellsworth, 2013; Keranen *et al.*, 2013). While there are strong spatiotemporal correlations between wastewater disposal and earthquake activity, constitutive relations are yet to be formulated.

### *This Study*

This chapter describes the Oklahoma seismic network and discusses preliminary results of the regional seismic analysis. The Oklahoma Geological Survey (OGS) monitors and documents seismic events within the state, since 1976 (Fig. 18). By 2010, OGS managed and operated a network of seven permanent and semi-permanent seismic stations. By late 2015, I managed and operated 20 seismic stations with real-time data streaming to monitor earthquakes. By 2017, in cooperation with the University of Oklahoma ConocoPhillips School of Geology and Geophysics (CPSGG), I manage and operate over 80 real-time seismic monitoring stations to monitor and locate earthquakes (Fig. 19), and investigate possibly induced seismicity. The network and results are shown in figures.

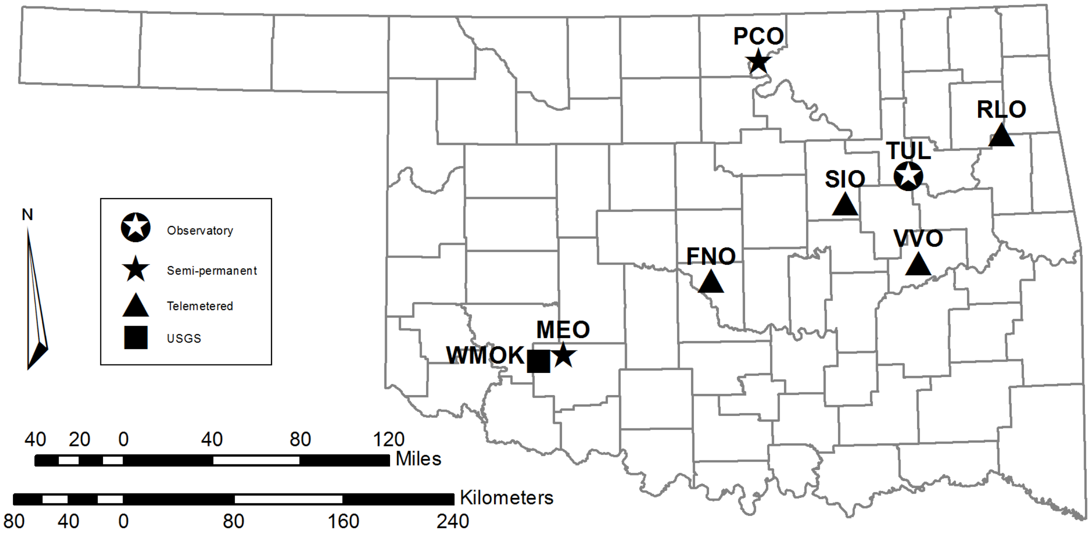

**Figure 18. Legacy Seismic Monitoring Stations in Oklahoma**
Historic seismic stations used by the OGS Geophysical Observatory to monitor earthquakes in 2010. The Geophysical Observatory was located in Leonard, OK (TUL) and operated four real-time telemetered stations (triangles) and two semi-permanent stations (stars). WMOK (square) is a USGS backbone station. Currently, the OGS still operates FNO and RLO, and USArray operates the TUL site.

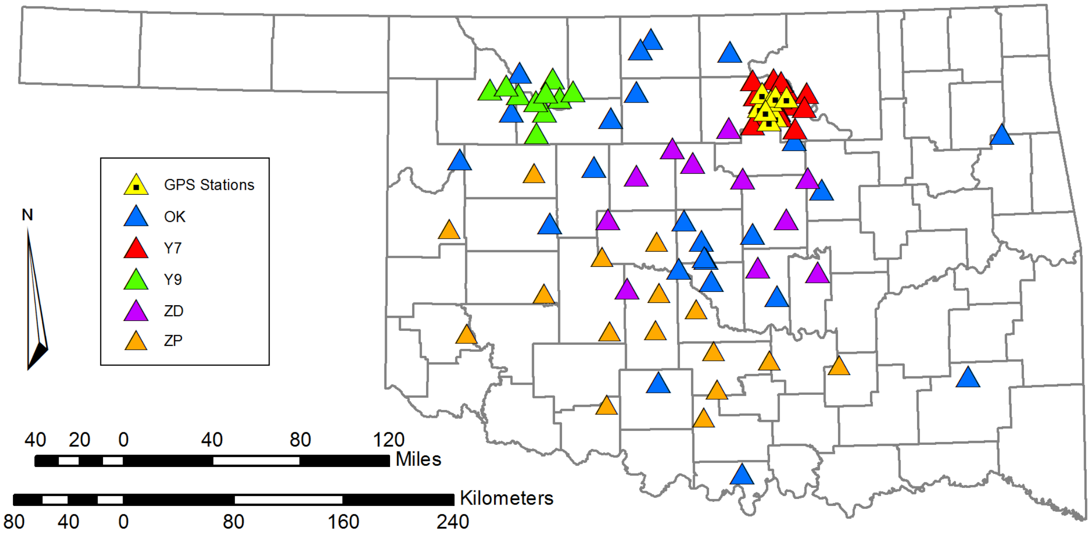

**Figure 19. Current Seismic Monitoring Stations in Oklahoma**
Current sites of real-time telemetered seismic monitoring and GPS stations operated by the OGS. International Federation of Digital Seismograph Network code: OK (blue) is the Oklahoma backbone network; Y7 (red) is the Pawnee aftershock monitoring network; Y9 (green) is the Fairview-Waynoka aftershock monitoring network; ZD (purple) is the Oklahoma Risk and Hazard (OKRaH) network; ZP (orange) is the Seismic Investigation of South Central Oklahoma (SISCO) network. GPS stations surrounding the Pawnee M5.8 epicenter are shown in yellow.

## Oklahoma Regional Seismic Network

### *Network and Data Description*

The Oklahoma regional seismic network uses real-time telemetered stations, located within and around Oklahoma and operated by the OGS, USGS, and other academic institutions (Fig. 20). I focus specifically on the OGS-operated subnets: OK, ZD, Y9, Y7, and ZP networks (Fig. 19). The data acquisition and analysis center is located at the University of Oklahoma in Norman. All stations are installed on properties volunteered by willing landowners.

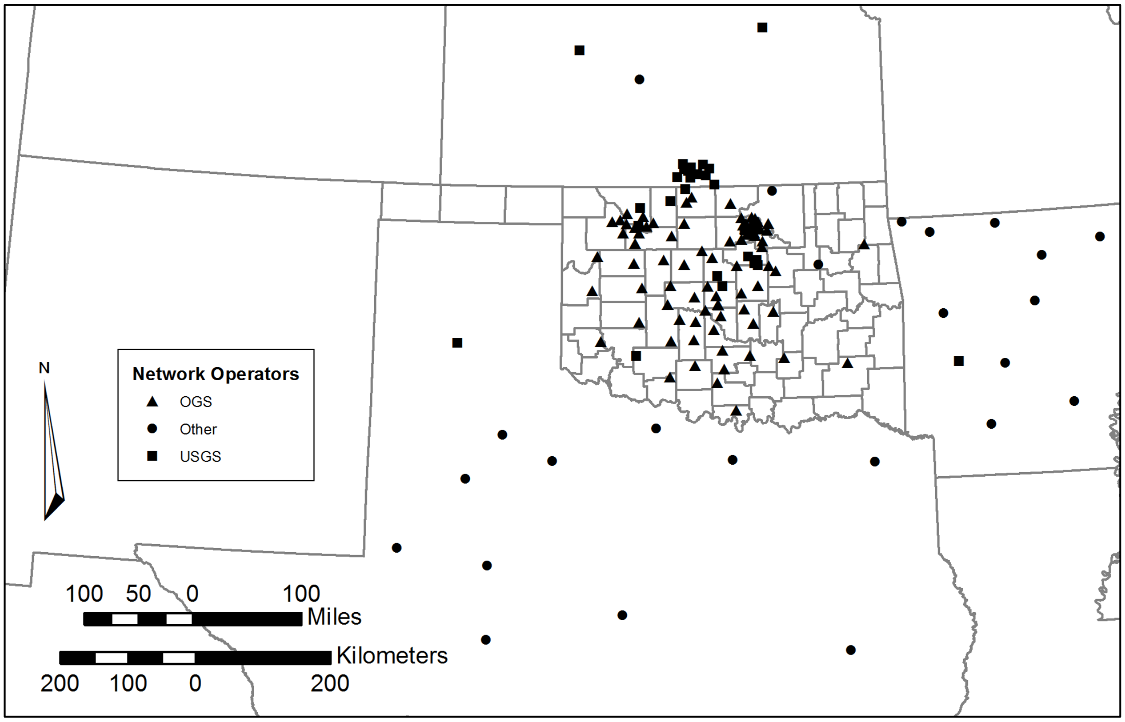

**Figure 20. Regional Seismic Monitoring Network**
Map of all telemetered seismic monitoring stations used in locating Oklahoma earthquakes. OGS operated stations are shown as triangles. USGS permanent and temporary stations are shown as squares. Telemetered stations operated by other institutions are shown as circles.

### *Oklahoma Seismic Network*

The Oklahoma Seismic Network (OK) is the oldest continually operating seismic network in Oklahoma. The network consists of 24 seismic station spread throughout the state. Each station is equipped with a three-component (3C) broadband seismometer. These are permanent and semi-permanent stations that are owned and maintained by the OGS. All seismic data are digitized at 100 Hz and publicly available.

### *Oklahoma Risk and Hazard (OKRaK) Network*

OKRaH (ZD) network is a temporary seismic deployment that is part of a larger interdisciplinary project: 4D Integrated Study Using Geology, Geophysics, Reservoir Modeling & Rock Mechanics to Develop Assessment Models for Potential Induced Seismicity Risk. It is aimed at studying central Oklahoma, and understanding the conditions in which seismicity increased. Each of the 12 stations is equipped with 3C short-period seismometers. Data from this deployment are sampled at 100 Hz, and have been made publicly available since 2016, when all of the stations were equipped with cellular modems.

### *Fairview-Waynoka Network*

The Fairview-Waynoka (Y9) network is a temporary seismic deployment to study the aftershocks of the 13 February 2016 M5.1 Fairview earthquake. Each station is equipped with 3C broadband seismometers, which are sampled at 100 Hz. Data from one station are publicly available, while a two-year embargo is set for the rest of the data for CPSGG researchers.

### ***Pawnee Network***

The Pawnee (Y7) network is a temporary seismic deployment to study the aftershocks of the 03 September 2016 Pawnee earthquake. Each station is equipped with 3C short-period seismometers. All seismic data from this deployment are sampled at 200 Hz, and publicly available.

### ***Seismic Investigation of South Central Oklahoma (SISCO)***

The SISCO (ZP) network is a temporary seismic deployment to monitor two oil and gas plays: South Central Oklahoma Oil Province (SCOOP) and Sooner Trend oil field Anadarko basin Canadian and Kingfisher counties (STACK). The network utilizes eight 3C broadband and eight 3C short-period sensors, spread throughout the southwest-third of Oklahoma. All seismic data from this deployment are sampled at 100 Hz, and are publicly available.

## *Data Acquisition*

Data from the Oklahoma regional seismic network are sent to an acquisition server at the University of Oklahoma, and archived at the Incorporated Research Institutions for Seismology (IRIS) data center. Data without research embargoes are shared with the USGS and other institutions. Seismograms are publicly available online through Winston Wave Server.

### ***Automatic Computer Processing***

The bulk of monitoring, an average of 360 channels of the real-time vertical- and horizontal-component data streams, is done automatically. Seismic data are analyzed by in-house software, *Seiproc*, which uses a rolling long-term average short-term average (LTA/STA) window to trigger events. If *Seiproc* detects three events on different stations within a time window, an origin timestamp is determined and 2.5-minute seismograms from the continuous wave buffer are cut and transferred to a separate directory for automatic processing and human analysis. Seismic analysts can also trigger events manually in cases where automatic detection did not.

### ***Analysis***

OGS seismic analysts examine and process the data to pick first motion and seismic phase arrival times to locate the earthquake, and pick seismic amplitudes and phase spectra to estimate earthquake magnitudes. Analysts process events in SEISAN earthquake analysis software. P- and S- phases times are picked and recorded, along with first-motion polarity. Event hypocenter is located using HYPO71 and a one-dimensional (1D) velocity model (Tbl. 4) chosen as the best solution from RMS misfit, using VELEST (Kissling *et al.*, 1994). First-motion polarity data are used to determine fault plane solutions (FPS) whenever possible. Once analysis is complete, OGS stores the earthquake metadata in a database, which OGS disseminates to the USGS and the public.

| Depth (km) | Velocity (km/s) |
|---|---|
| 0.0 | 2.70 |
| 0.3 | 2.95 |
| 1.0 | 4.15 |
| 1.5 | 5.80 |
| 8.0 | 6.27 |
| 21.0 | 6.41 |
| 42.0 | 7.90 |
| 50.0 | 8.15 |

**Table 4. Seismic Velocity Profile for Oklahoma**
1D P-wave velocity model used infor the State of Oklahoma used by the OGS earthquake location program, with Vp/Vs ratio of 1.73.

### *Magnitude Calculation*

OGS seismic analysts calculate magnitudes for all analyzed events. The preferred magnitude reported is as follows: moment magnitude ($M_W$), local magnitude ($M_L$), and duration magnitude ($M_D$). OGS reports $M_W$ if it is available; if not, OGS reports $M_L$ if it is available; if not, OGS reports $M_D$. $M_W$ are typically computed for earthquakes with ≥ M3.5, using frequency spectra analysis in SEISAN (Ottemoller *et al.*, 2017). $M_L$ are estimated from stations within 25-250 km of the epicenter, using amplitude calculations on the horizontal components of the seismogram digitally simulated as a Wood-Anderson seismograph (Richter, 1935):

$$\mathrm{M_L} = \log \mathrm{A} - \log \mathrm{A_O}(\Delta) \;, \tag{4.1}$$

where $A$ is the maximum amplitude (in millimeters) for the station at $\Delta$ km, and $A_O(\Delta)$ is the maximum amplitude for a standard earthquake. $M_D$ are estimated if no other magnitude calculation is possible. OGS uses the derivation by Lawson (1978), based on the empirical relations determined by Lee *et al.* (1972):

$$M_D = 1.86 \log D - 1.49 \;, \tag{4.2}$$

where $D$ is the duration in seconds from the P-wave arrival time until the final coda amplitude decreases to twice the background-noise amplitude.

## Oklahoma Seismicity

### *Seismicity Trends 2010-2017*

The seismicity rate discussed in this chapter is the number of earthquakes during the specified time period and for the magnitude range defined in context. The number of M3+ earthquakes in Oklahoma increased steadily for 2010 to early 2013 (Tbl. 3), with the exception to a temporal spike in late 2011; this spike is attributed to the November 06, 2011 M5.7 Prague earthquake and its aftershocks (Fig. 21). The seismicity rate increase from 2013 to 2014 may be partly attributed to an increase and rearrangement of seismic monitoring stations, but the dramatic rise in seismicity from 110 M3+ earthquakes in 2013 to 579 M3+ earthquakes in 2014 is an absolute increase in earthquake activity and not a reflection of earthquake detectability. After seismicity rates peaked in 2015-2016, with 903 and 624 M3+ earthquakes, respectively, I observe a marked decrease in 2017 that is 283 M3+ earthquakes by 2017 December 04—I expect the final count for M3+ earthquakes to be than 300 when the year ends.

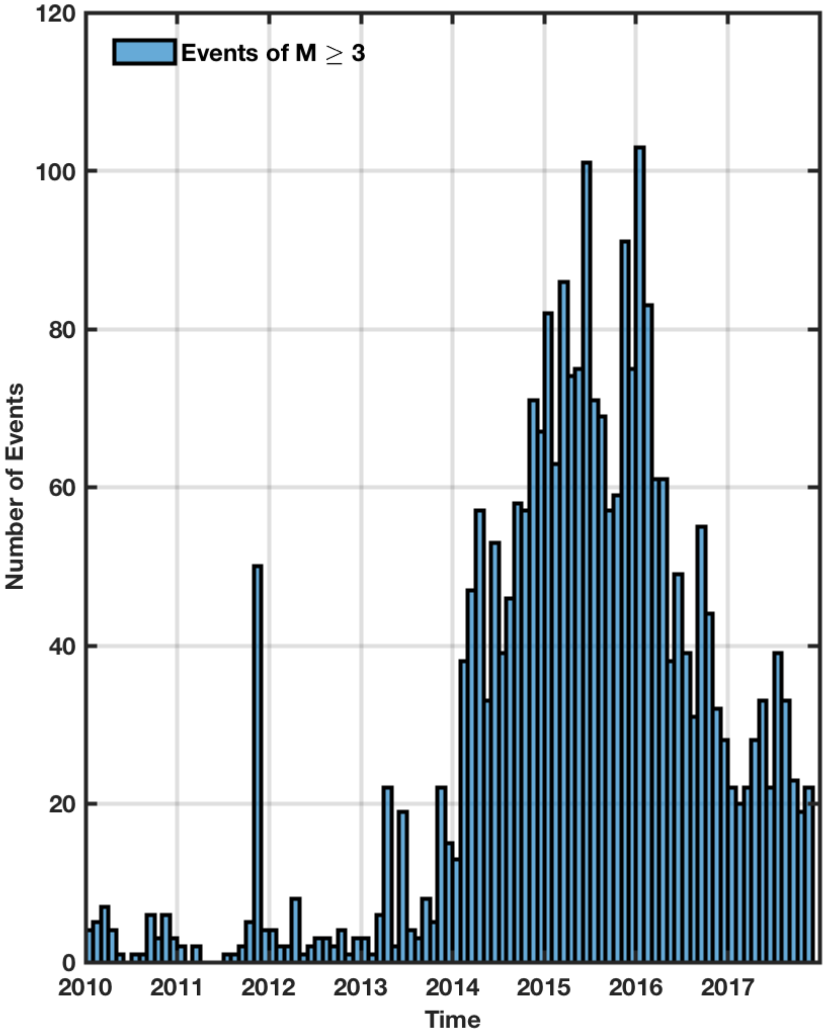

**Figure 21. Monthly Seismicity in Oklahoma**
Monthly histogram count for M3+ earthquakes from 2010 to 2017. Data are from the Oklahoma Earthquake Catalog.

### *Hypocenters*

## ***Central Oklahoma Seismicity***

Oklahoma seismicity displays a lateral migration of from central to northern Oklahoma over time. Earthquakes prior to 2010 were primarily happening in the southcentral region of the state, a wide swath from far-southcentral to west-central Oklahoma, approximately 9,600 $km^2$ (Fig. 22). Seismicity from 2010-2011 occurred mainly in central and southcentral Oklahoma, and concentrated in eastern Oklahoma, southeastern Lincoln, eastern Okfuskee, and northwestern Coal counties (Figs. 23 and 24). In 2012, I see seismicity remains steady in central Oklahoma counties. Coal county seismic activity subsides, and northcentral Oklahoma begins to experience small and sparse earthquakes. After 2012, the seismicity rate in the state increased drastically, but the seismicity rate in central Oklahoma remains steady (Fig. 25).

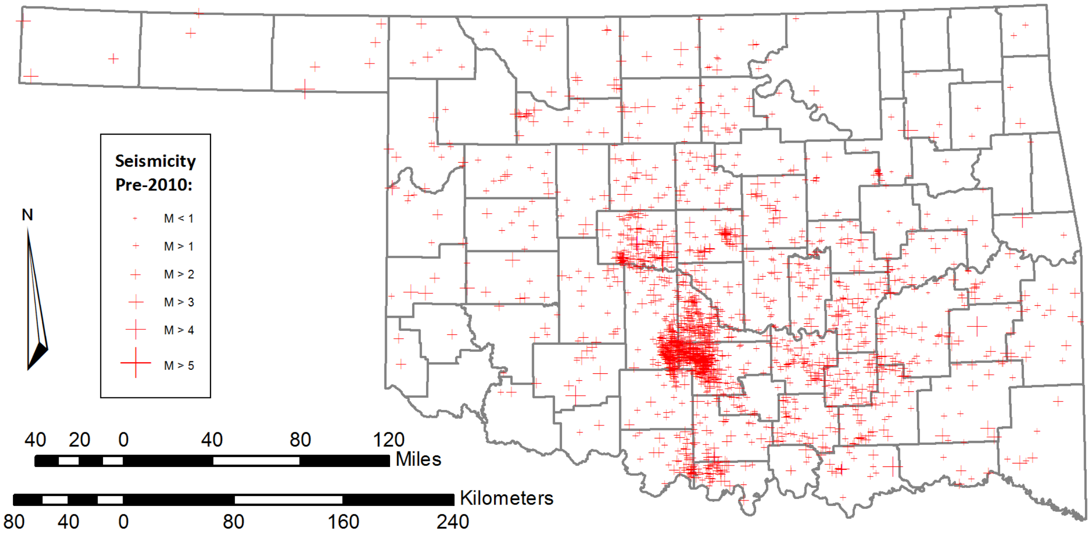

**Figure 22. Oklahoma Seismicity Map: 1882-2009**
Oklahoma seismicity from 1882 to the end of 2009 (data from the Oklahoma Earthquake Catalog). Crosses show location of events, cross sizes are scaled according to magnitude.

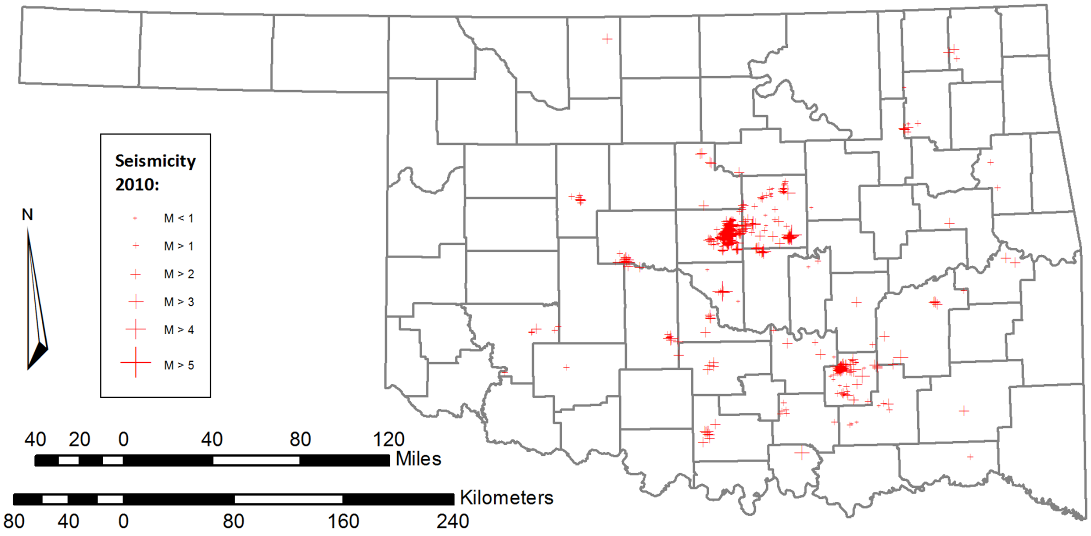

**Figure 23. Oklahoma Seismicity Map: 2010**
Oklahoma seismicity for 2010 (data from the Oklahoma Earthquake Catalog). Crosses show location of events, cross sizes are scaled according to magnitude.

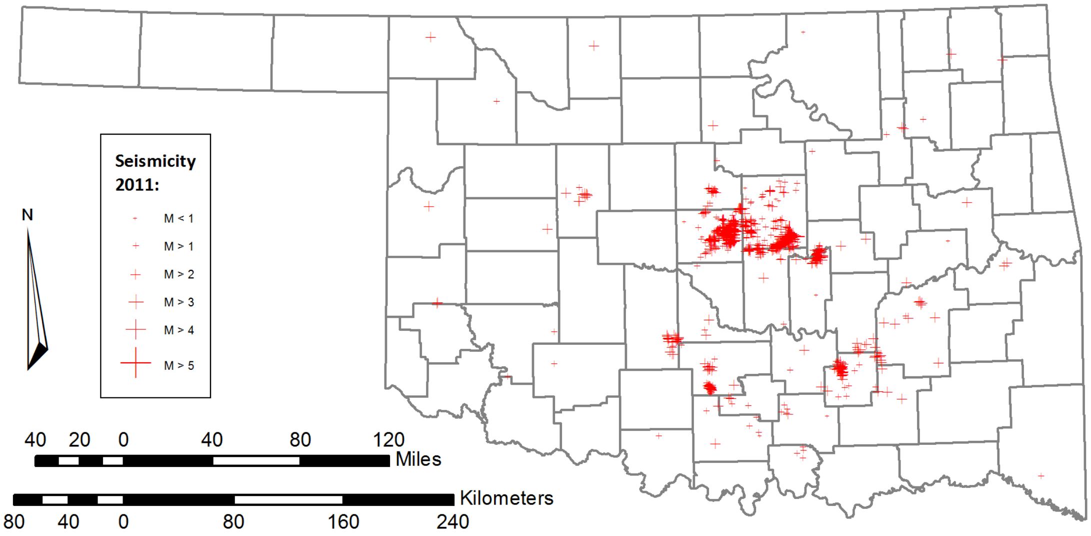

**Figure 24. Oklahoma Seismicity Map: 2011**
Oklahoma seismicity for 2011 (data from the Oklahoma Earthquake Catalog). Crosses show location of events, cross sizes are scaled according to magnitude.

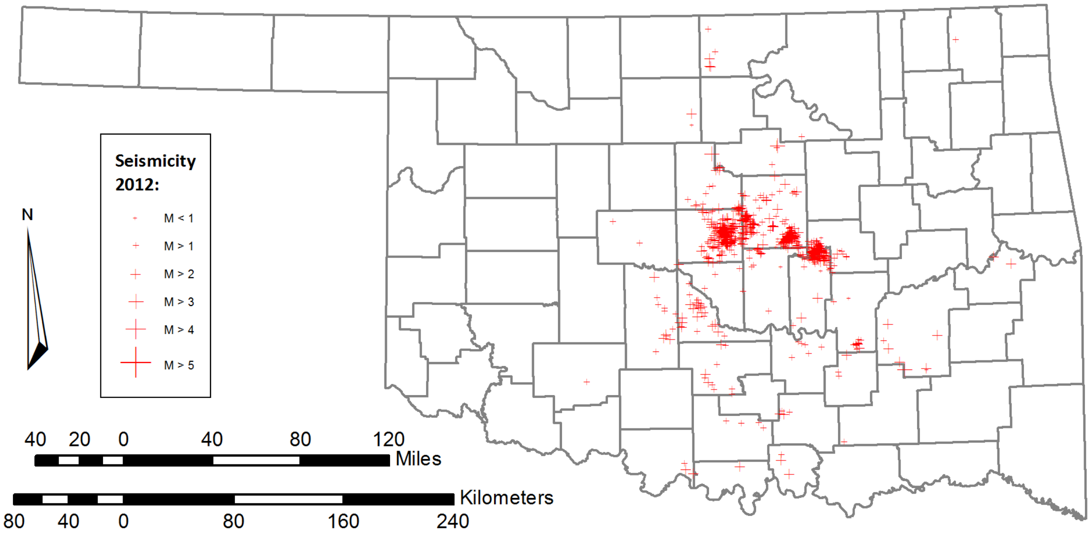

**Figure 25. Oklahoma Seismicity Map: 2012**
Oklahoma seismicity for 2012 (data from the Oklahoma Earthquake Catalog). Crosses show location of events, cross sizes are scaled according to magnitude.

### *Northern Oklahoma*

In 2013, northcentral Oklahoma counties experience a drastic increase in earthquake activity, with seismicity spreading to Logan and Payne counties (Fig. 26). In 2014, seismicity in the south appears to form a linear trend from southcentral to west-central Oklahoma; seismic activity in central and northcentral Oklahoma spreads further northwest and west, respectively, but appear to be migrating away from the south; a lineament of earthquakes begin to form in northeast Woodward county (Fig. 27). In 2015, earthquake activity in southern Oklahoma subsides, while seismicity in northcentral Oklahoma intensifies (Fig. 28). In 2016, I observe localized clustered seismic activity in west-central Oklahoma. Seismicity in central and northcentral Oklahoma seem to occur more in lineaments (Fig. 29) in 2017. New lineaments in northwestern Oklahoma begin to show activity; while the general seismicity in the state is subsiding, the pattern of seismicity seems to form tighter clusters in general (Fig. 30).

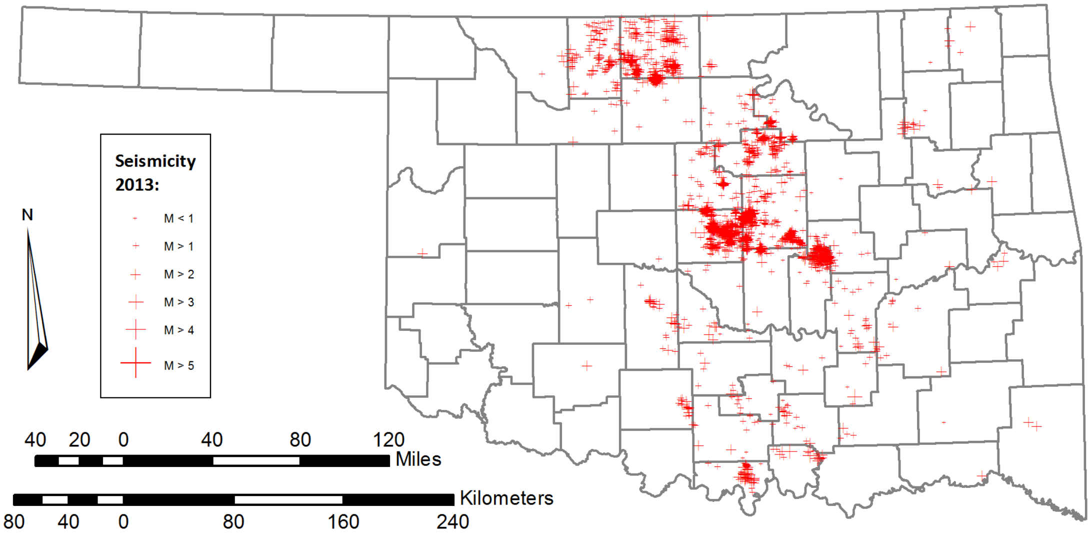

**Figure 26. Oklahoma Seismicity Map: 2013**
Oklahoma seismicity for 2013 (data from the Oklahoma Earthquake Catalog). Crosses show location of events, cross sizes are scaled according to magnitude.

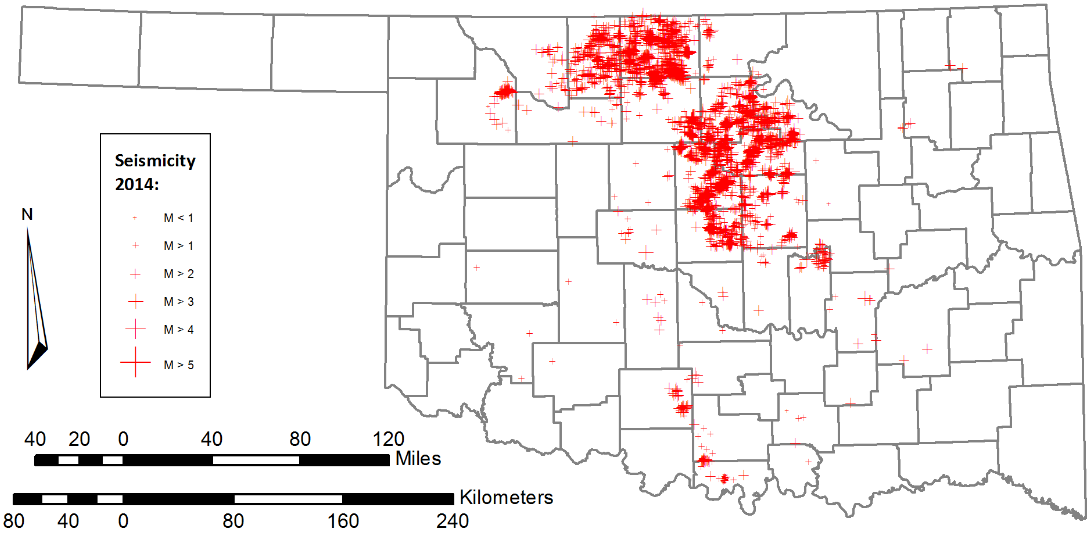

**Figure 27. Oklahoma Seismicity Map: 2014**
Oklahoma seismicity for 2014 (data from the Oklahoma Earthquake Catalog). Crosses show location of events, cross sizes are scaled according to magnitude.

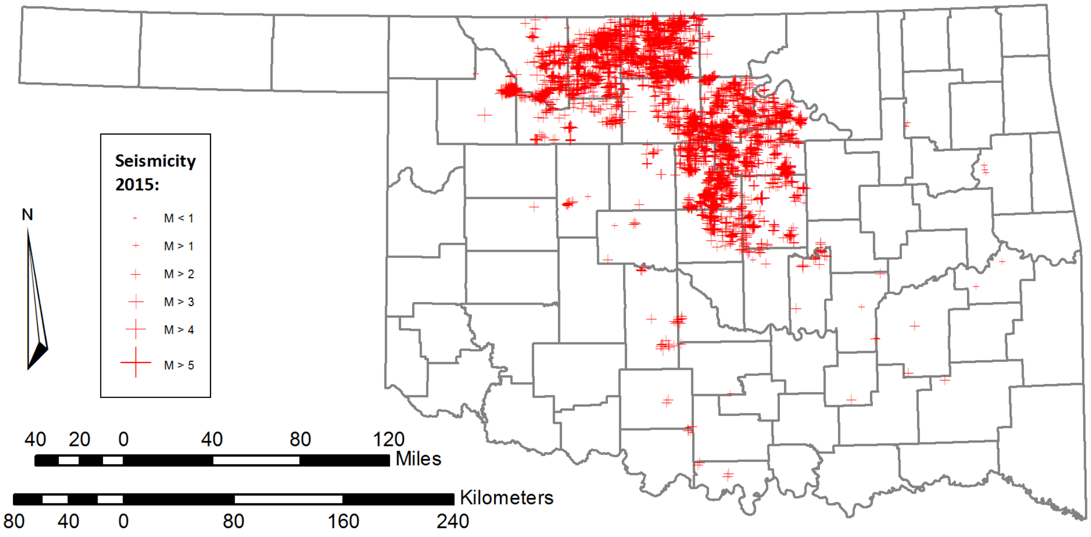

**Figure 28. Oklahoma Seismicity Map: 2015**
Oklahoma seismicity for 2015 (data from the Oklahoma Earthquake Catalog). Crosses show location of events, cross sizes are scaled according to magnitude.

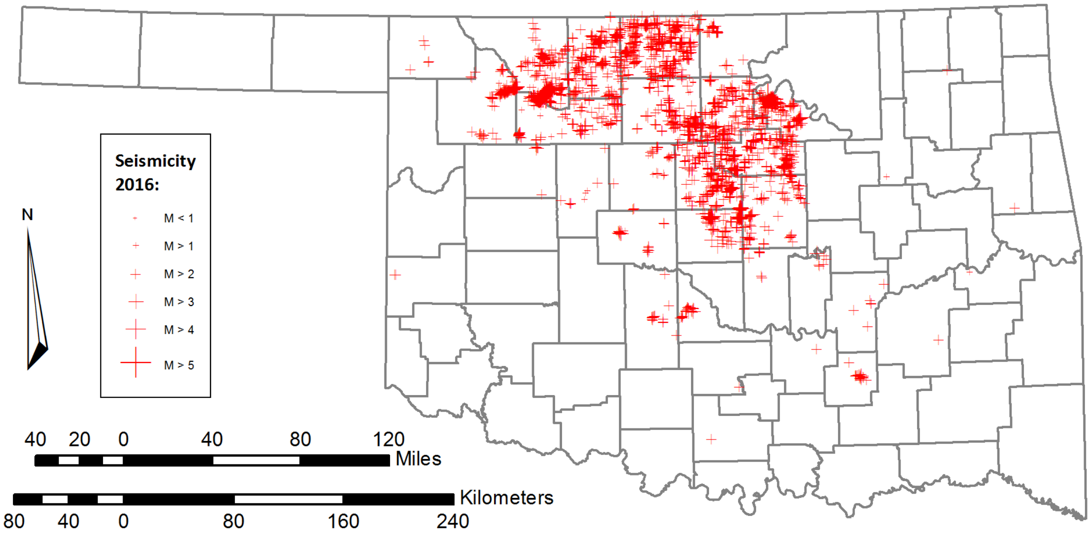

**Figure 29. Oklahoma Seismicity Map: 2016**
Oklahoma seismicity for 2016 (data from the Oklahoma Earthquake Catalog). Crosses show location of events, cross sizes are scaled according to magnitude.

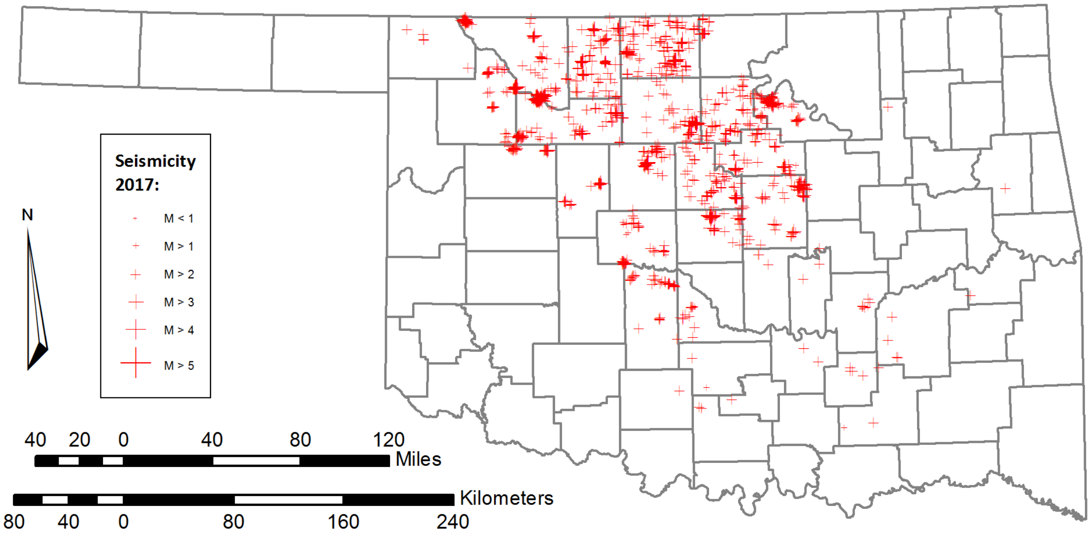

**Figure 30. Oklahoma Seismicity Map: 2017**
Oklahoma seismicity for 2017 (data from the Oklahoma Earthquake Catalog). Crosses show location of events, cross sizes are scaled according to magnitude.

### *Deepening with Time*

Reported earthquake depths are relative to the station elevations used to analyze the events. Depths of 5 km are manually assigned to an event if the hypocenter is poorly constrained. Most seismic activity in Oklahoma occur in the crystalline basement. The hypocentral depths increased from approximately 4 km in 2010-2013, to 5 km in 2014-2015, and to 6 km after 2015.

#### *Focal Mechanisms*

OGS seismic analysts determined fault plane solutions (FPS) using P-wave first-motion polarities for all magnitude events, and recorded FPS only if the auxiliary planes are well-constrained by the polarity data. Throughout most of Oklahoma, the FPS systematically indicate strike-slip motion with minor components of reverse of normal slip. FPS in far northcentral Oklahoma and southern Kansas, indicate a few extensional dip-slip along with the strike-slip solutions (Fig. 31).

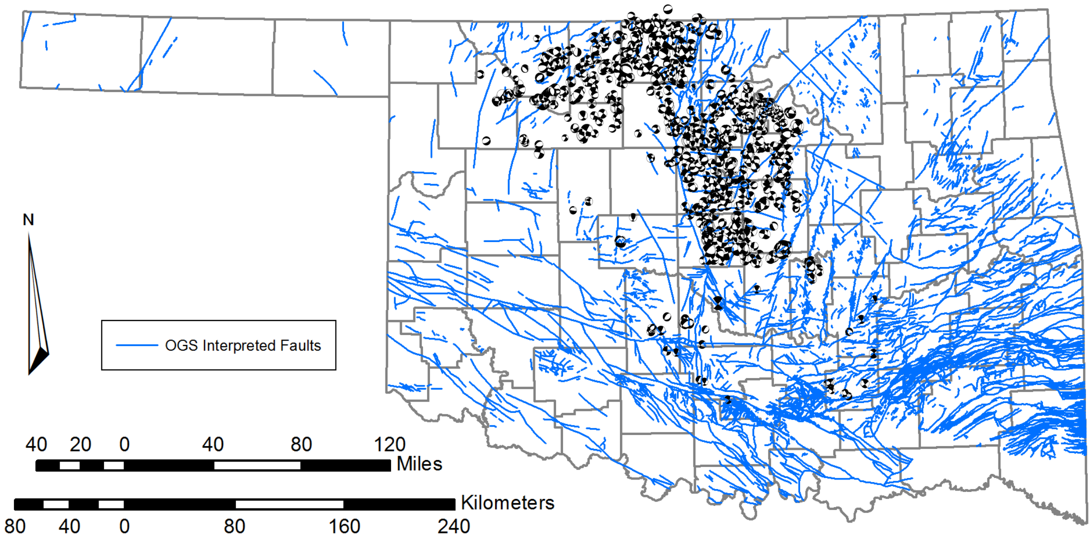

**Figure 31. Oklahoma Focal Plane Solutions**
Focal plane solutions for some Oklahoma earthquakes, from 2010 to 2016. Data for 2017 events are currently unavailable.

### The 03 September 2016 M5.8 Pawnee Earthquake

The M5.8 Pawnee earthquake is the strongest instrumentally recorded earthquake in Oklahoma. It was a moderate earthquake that was felt strongly across the state, with a maximum Modified Mercalli Intensity (MMI) of VIII, and was also felt as far as Denver, CO, Minneapolis, MN, San Antonio, TX, and Louisville, KY (USGS DYFI Reports). I visited the epicenter area to investigate damage, and found no evidence of a fault scarp. I found multiple sand blows near river banks (Fig. 32), while a few buildings had damage with cracked walls, fallen chimneys, and shifted foundation. The local community reported that one person was hospitalized for a head injury from a falling brick.

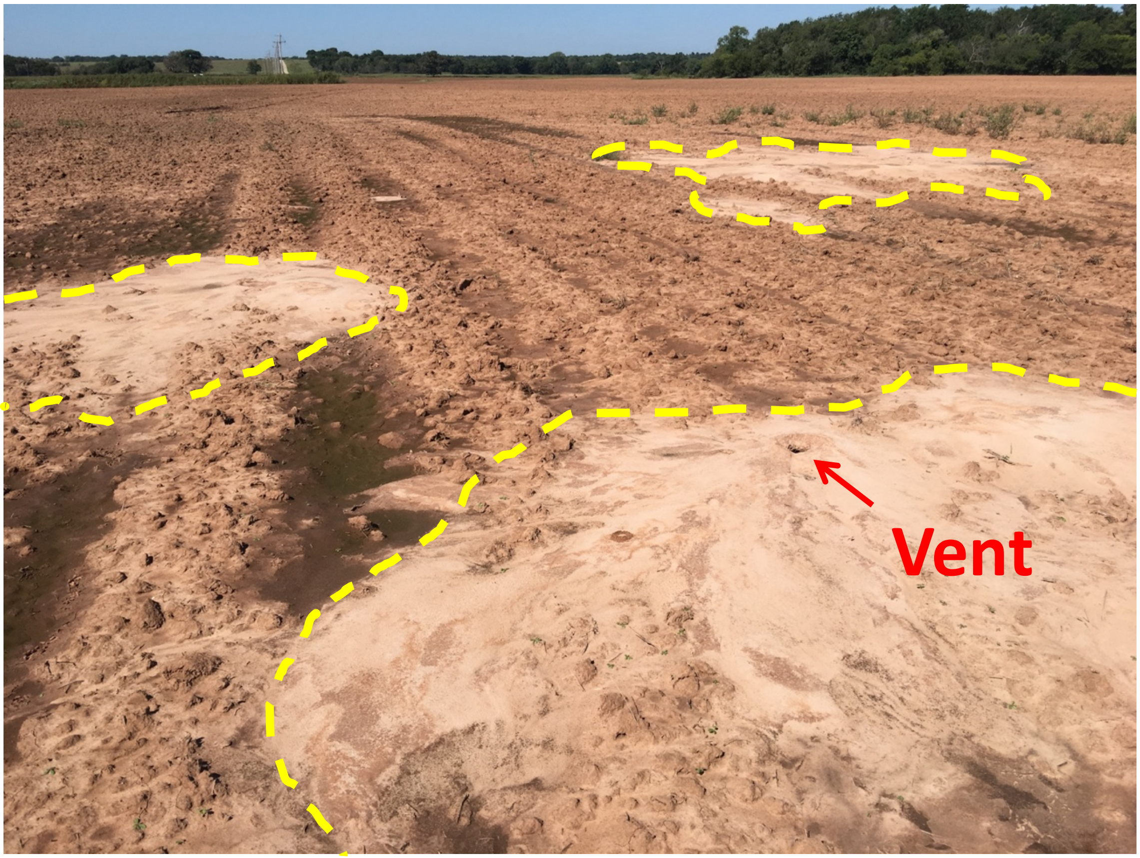

**Figure 32. Sand Blows near the M5.8 Pawnee Epicenter**
Sand blows (or sand boils) near Black Bear Creek, approximately 8 km S 10° E of the M5.8 Pawnee epicenter. I observed approximately 20 sand blows that ranged in size, from 1-12 m in diameter, with most averaging of 3-6 m in diameter, identified here in yellow dashed lines. Location of expulsive vent for the proximal mound is shown in red.

**Figure 33. Fissure near the M5.8 Pawnee Epicenter**
Fissure that reportedly opened up after the M5.8 Pawnee earthquake, immediately north of the Arkansas River in Osage county, approximately 3 km due north of the epicenter. Land owner reported that the fracture was over 15 m deep in some areas. Photo courtesy of Rick Rice.

### *Mainshock*

A $M_W$ 5.8 earthquake occurred northwest of Pawnee, Oklahoma on 03 September 2016 at 12:02:44.43 UTC, in the region of the Watchorn and Labette faults. It was initially suspected that the event was right-lateral slip on a southern segment of the northeast-southwest striking Labette Fault, because seismic activity was located along that segment for months prior to as late as a few days before the mainshock (Chen *et al.*, 2017). However, aftershock analyses (Walter *et al.*, 2017) and satellite radar interferometry (InSAR) (Fielding *et al.*, 2017) showed that the earthquake slipped left-laterally on an unknown fault that I named the Sooner Lake Fault (some publications may refer to it as the Pawnee Fault, such as Yeck *et al.* (2017)).

### *Aftershocks*

The Oklahoma regional seismic network recorded over 500 aftershocks in a cluster surrounding the hypocenter, within a year of the mainshock (Fig. 34). Since the mainshock occurred near the intersection of three faults, I am including seismic activity on all three faults as aftershocks. OGS seismic analysts located tens of events on the Watchorn fault, from the intersection south, but not north. The Labette segment has been moderately active with over 150 aftershocks. The bulk of the aftershocks, a year after the mainshock, occured on the Sooner Lake Fault. After more than one year since the M5.8 event, the area has not experienced an aftershock of M4 or greater.

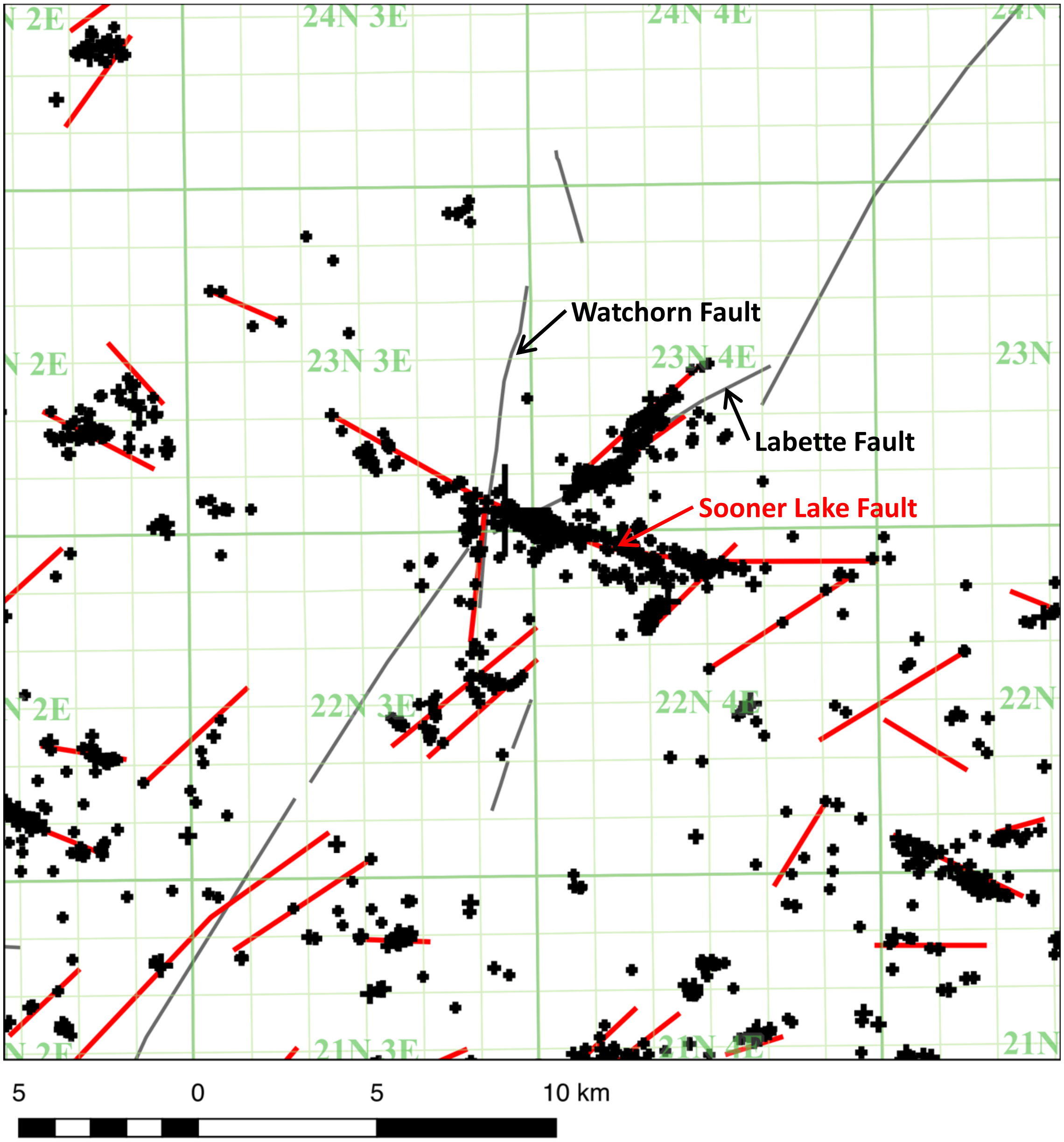

**Figure 34. Seismicity Map of the Pawnee Aftershocks**
Seismicity map centered on the M5.8 Pawnee earthquake (large black cross). Seismicity shown is from 2016 September 03 12:02:44.43 (UTC) to one year later. Seismogenic faults in this study are shown in red. Interpretive faults (Marsh and Holland, 2016) from the Oklahoma Fault Database are shown in black lines.

### *Long-term Deformation*

In response to the M5.8 Pawnee earthquake, we installed eight permanent real-time GPS stations surrounding the epicentral region in Pawnee and Osage counties (Fig. 19). In the future, I plan on augmenting the GPS station coverage with more permanent stations and a rigorous temporary station campaign in order to better understand intraplate crustal deformation in Oklahoma, not only from earthquake slip, but also from extraction of natural resources (Segall, 1985) and fluid injection (Shirzaei *et al.*, 2016). Due to the time it takes to monitor changes in long-term crustal deformation, I have yet to collect sufficient data from this effort to synthesize results.

## **Discussion**

### *Spatiotemporal Correlations of Earthquakes with Oil and Gas Activity*

Concentrated areas of seismicity coincide with oil and gas plays: the Hunton Reservoir (informally the Hunton de-watering play), in east-central Oklahoma; the Mississippi Lime, across much of northern Oklahoma; and the SCOOP and STACK in west-central, southwestern, and southern Oklahoma. The Hunton Reservoir and Mississippi Lime plays are both wet plays, with an approximate 9:1 or higher ratio of water to oil and gas (Chesapeake, 2009). Much of the wastewater/saltwater disposal volumes in Oklahoma come from these two plays. The SCOOP and STACK plays are reportedly drier plays, which means operators have less volumes of wastewater to dispose (Oklahoma Corporation Commission, personal communication, 2016). All three plays are more economic due to horizontal drilling and hydraulic fracturing well-stimulation.

Spatiotemporal trends of seismicity appear to follow oil and gas activity, after a two-year lag, in plays of high-water content that require high volumes of wastewater disposal into the Arbuckle aquifer (Keranen *et al.*, 2013; Walsh and Zoback, 2015). Prior to 2013, seismic activity was confined in central Oklahoma, in the South and Southeast Cherokee Platform (Figs. 23-25). Horizontal drilling rigs in the Mississippi Lime quadrupled from 2011 to 2012, after which, activity plateaued until 2015, when drilling activity dropped down to the same level as early 2011 (Natural Gas Intelligence, 2017). Seismic activity in northern Oklahoma began in 2013 and rose dramatically in 2014, peaking in 2015, and is in general decline to about the same activity as late 2013. Although the development of these two plays utilize horizontal wells and hydraulic well-stimulations, the sustained seismic activity in the regions suggests that a likely tie exists with sustained disposal activity, as well-stimulations are relatively shorter in duration—which are a few weeks on average.

Spatiotemporal correlation with hydraulic well-stimulations are designed to cause small earthquakes. Although most events are "microseismic" (smaller than M2) earthquakes, I observed cases where earthquakes > M2 occur within 2 km of a well-head and within lass than 10 days of well-completion, where background seismicity prior to fracking activity was negligible, in both the SCOOP and STACK plays. The SCOOP and STACK plays were announced in 2014, and oil and gas extraction has since slowly increased (Shale Experts, 2017). In late-2016 until our current analysis time (late-2017), seismic activity has increased in these areas, and have been felt by local residents in Grady, McClain, Garvin, Blaine, Kingfisher, and Canadian counties. I also observe earthquakes in the Mississippi Lime play that fall within this spatiotemporal relationship. Unfortunately, the background seismicity in the area makes its temporal correlation less constrained when linked to well-completion activities.

### *Anomalous Seismicity and Aseismicity*

Not all seismicity in Oklahoma has close spatiotemporal correlations with oil and gas activities—conversely, not all oil and gas activity in Oklahoma has spatiotemporal correlations with seismicity. I observe the former scenario in the Fairview-Waynoka swarm, where the nearest significant saltwater disposal wells are 15 km away. I observe the latter scenario in Osage county, where oil and gas activity is prevalent in the Mississippi Lime play, yet the area has little to no seismicity—less than two dozen unfelt earthquakes in the county interior have been documented in the entire 130-year record of the Oklahoma Earthquake Catalog (Figs. 22-30). These observations suggest that injection activity alone is not enough to induce earthquakes in Oklahoma. The bounding conditions in which human activity may trigger seismic slip remains unresolved.

### *Seismicity and its Relationship to Mapped Faults*

The regional stress field in Oklahoma is roughly east-west for $S_{Hmax}$ (Zoback and Zoback, 1991). Although Darold and Holland (2015) highlighted optimally oriented faults with strikes that favor seismic slip with the regional stress, I note that most seismic activity in the state do not occur on these mapped faults (Fig. 19). I mapped fault-plane derived faults from seismicity recorded with our regional network (Fig. 20). These seismogenic faults and first motion-derived FPS are consistent with in-situ borehole stresses (Alt and Zoback, 2016). This may suggest that the dominant stresses acting on the faults are regional, and not cause by local stress perturbations.

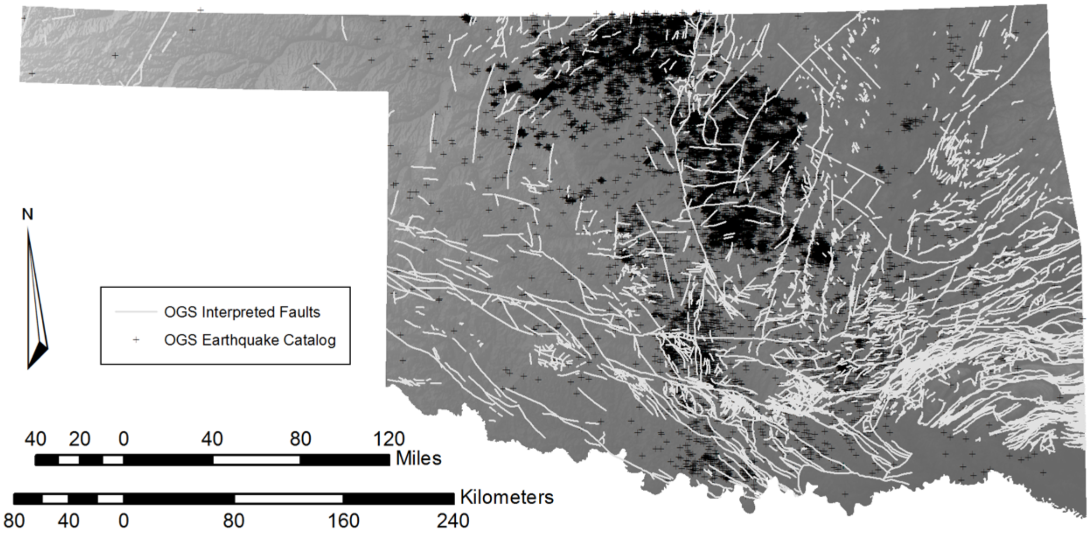

**Figure 35. Oklahoma Fault Map**
Map of the OGS earthquake catalog (black +) and OGS published faults (light-gray lines) show that seismicity occurred mostly on unmapped faults.

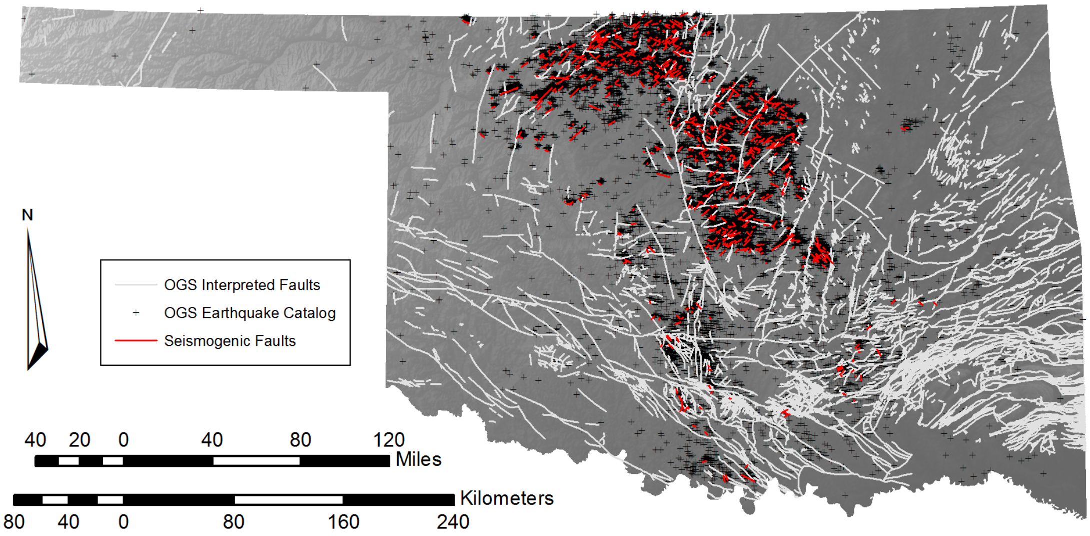

**Figure 36. Seismogenic Faults from this Study**
Seismogenic faults (red lines) derived from HypoDD relocated earthquakes that will be added to the OGS fault database (gray lines). Only events from 2010 and younger were relocated due to the unavailability of digitized phase picks from older paper records.

### *Inducing Seismicity*

The leading hypothesis that relates fluid injection to seismicity is that the fluid communicates with deeper basement faults, either directly via permeable faults and fractures, or indirectly through pressure pulses. Wastewater fluids are typically disposed into the Arbuckle aquifer, which directly overlies the top of the crystalline basement, for much of Oklahoma. The fluid or pressure is thought to perturb the normal force on a tectonically loaded fault, causing less clamping force and unlocking the fault, thereby allowing the built-up strain to release. If this is the case, I propose that an earthquake which propagates from the top-down is likely induced, in contrast to natural fault-slip as being a result of tectonic plate motion, which is driven from below.

### *The M5.8 Pawnee Earthquake as a Possibly Induced Earthquake*

The M5.8 Pawnee earthquake slipped on an unmapped fault in the Mississippi Lime play. The epicenter is surrounded by dozens of wastewater disposal wells into the Arbuckle Group. I observed episodes of foreshock activity in the area, which may have led to stress shadows triggering the mainshock (Chen *et al.*, 2017). I also note that the Pawnee foreshock pattern is tantamount to foreshock patterns observed near plate boundaries (Walter *et al.*, 2017). Although it is possible that foreshock activity may have triggered the Pawnee earthquake, I do not have direct evidence that it did. In contrast, Fielding *et al.* (2017) used InSAR data to model crustal deformation and coseismic-slip, and the modeled top-down slip-propagation suggests that the Sooner Lake Fault unlocked from shallow to deep.

## Summary

1. I led the deployment of a denser Oklahoma seismological network that now comprises a backbone of 22 permanent stations spread throughout the state, and four temporary, local networks, totaling 58 stations. I also utilized publicly shared seismic data from networks operated in Oklahoma and surrounding states.
2. The majority of detected earthquakes migrated from central to northern Oklahoma, with temporal pattern following wastewater disposal of oil and gas production activity. The focal depths of almost all analyzed events occur between 2 to 9 km, primarily within the crystalline basement. Two dominant regions of seismicity emerge with spatial correlation to oil and gas activities, with a two-year lag from peak wastewater disposal activity to peak seismic activity.
3. A spatiotemporal correlation between hydraulic well-stimulations and felt seismicity was noted at distances less than 2 km away from the well-head, and during well-stimulation or less than 10 days after well-completion.
4. I use well-constrained first-motion P-wave focal mechanisms from our regional network, and mapped clustered hypocenters and aftershocks to define three-dimensional seismogenic fault planes to add to the Oklahoma Fault Database. The majority of recorded Oklahoma earthquakes occur in the crystalline basement, primarily along unmapped faults.

5. The regional stress field of N 78° E for central Oklahoma (Dart, 1990) sufficiently explains the observed strike-slip style of faulting the analyzed in Oklahoma earthquakes.
6. The probable seismic hazards derived from known faults should be taken as minima, since the strongest earthquake recorded in Oklahoma occurred on an unmapped fault. Seismic hazard from unmapped faults still pose a risk that is difficult to mitigate.

# Chapter 5: Realizing the Potential of the Full Gravity Field[3]

## Preamble

The impetus to model vertical component of the gravity field using a vertical line element mass approximation came from Dr. Kevin Crain. I created the working algorithm described here, derived the listed equations for the gravitational potential from a point source from first principles, and postulated the idea of periscopic modeling. The Osage model was a joint effort by Dr. Kevin Crain and myself. I generated all other texts and figures within this manuscript, unless otherwise noted.

## Abstract

The entire gravity field is the unique result of mass distribution. Using a vertical line mass approximation, I developed a new forward modeling algorithm that not only calculates the vertical component of gravity, but also the full tensor gravity gradient. The Semi-Infinite Gravity Modeling Algorithm (SIGMA) offers significant improvement in computation speed over conventional mass approximations, without sacrificing accuracy. I tested SIGMA against analytical solutions and found it to be accurate to within the limit of 64-bit double-precision arithmetic. The significant reduction in computation times without losing accuracy may also benefit other geophysical methods, such as geomagnetic modeling, topographic and isostatic reductions in geodesy. An exceptional feature of SIGMA is the ability to calculate the gravity value at any given point, not only on the Earth's surface, but also in the air, within a mine, down a borehole, in a submarine, on the seafloor. This ability to

---

[3] This chapter is planned to be submitted for publication, with Dr. Kevin Crain as the second author.

concurrently model points at any point of observation is the key to realizing the full gravity field, which constrains density distributions more inimitably than equipotential observations.

SIGMA is a flexible tool in modeling potential fields. I illustrate the accuracy and efficiency of this new modeling tool by applying it to a standard sphere model. I illustrate the utility of SIGMA with current gravity modeling techniques with a case study of the gravity high in Osage County, Oklahoma. Finally, I expand on the possibilities of modeling the entire gravity field with a synthetic case, using data from a variety of different depths that shows the value of SIGMA in merging heterogeneous acquisition campaigns.

## Introduction

### *Current Gravity Modeling*

The fundamental basis for how the gravity method works is mass accountability, which can be traced back to Newton's Law of universal gravitation:

$$F = G\frac{m_i\, m_n}{R^2}\,, \tag{5.1}$$

where $G$ is gravitational constant, $m_n$ is the of the relative distribution of mass, and $R$ is the Euclidean distance away from the gravity meter, $m_i$. A successful gravity investigation accounts for the masses and their volumetric distribution within the model to match the observed readings. Corrections to the raw observations are applied to account for the bulk mass of the Earth and its topographic irregularities, so that investigators are only modeling gravity "anomalies", or masses that have not been accounted for by these bulk corrections. The latitude correction accounts for the Earth's elliptical shape. Since the gravity meter gets closer to the center of the Earth at the poles, the gravity is expected to increase with increase in latitude. The Free Air Correction accounts for gravity variations due to elevation. The Bouguer Slab corrects for the excess mass beneath the observation point, if the point is above the reference datum, or the deficient mass above the observation point, if the point is beneath the reference datum. The Terrain Correction accounts for variations in the observed gravity caused by variations in topography near the observation point, which can be a very complex operation as it corrects for the topography that undulates above and below the elevation plane of the gravity station or observation point (Hayford and Bowie, 1912).

### *Mass Approximation Methods*

Modern tools such as computers and high-resolution digital elevation models have not changed the way in which gravity and gravity corrections calculated, but rather removed the tedium of computing gravitational effect of the mass distribution in the model. Another outcome of using computers is that data are discretized, typically as grids (e.g., square pixels on digital elevation models (DEM). The natural extrusion of two-dimensional (2D) grids in three-dimensions (3D) is a prism. The most common method in 3D gravity modeling is to fit a surface with a suite of right-rectangular cylinders (prisms) to approximate the subsurface mass (Fig. 37) (Nagy, 1966; Nagy *et al.*, 2000 and 2002), but this method requires extensive computation times when corrections are needed (Rodriguez *et al.*, 2005). Because of this computationally expensive modeling approach, previous workers suggested several alternatives to approximate mass with the equivalent mass of a prism, using different geometric elements: Heiland (1940) suggested a thin vertical plate; Danes (1960) suggested using vertical lines; Grüninger (1990) formulated the point mass and mass layer approximations of a tesseroid; Heck and Seitz (2007) formulated the use of tesseroids.

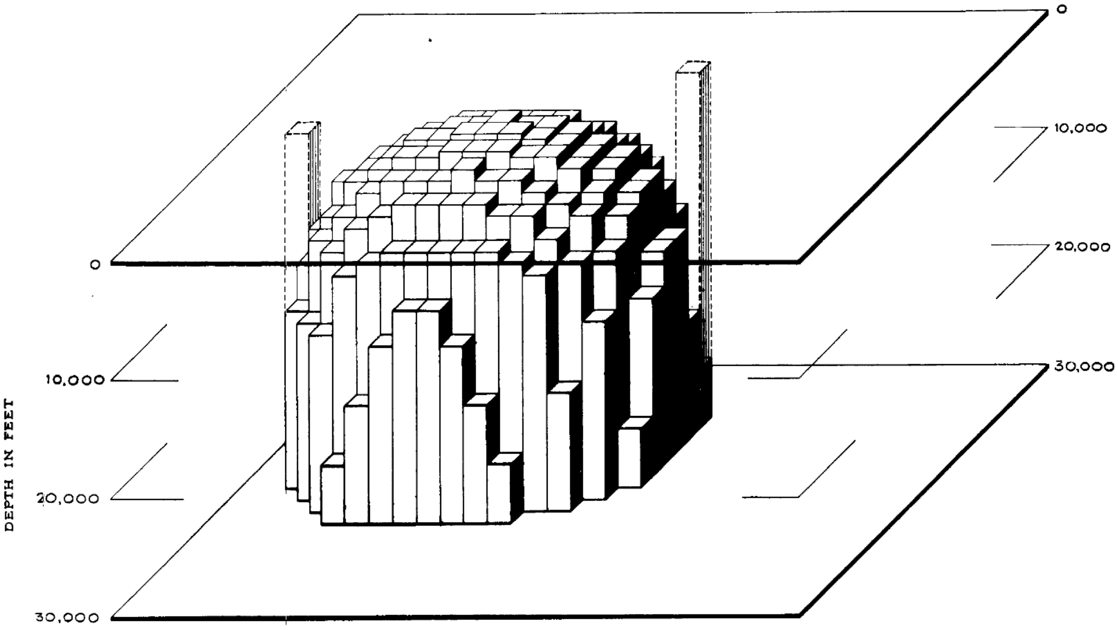

**Figure 37. Underground Mass Body Represented by Prisms**
An underground mass body representing a salt dome, with two right-rectangular cylinders (prisms) projected to the surface (0 ft), from Danes (1960).

### *This Study*

In this work, I modify the vertical line mass approximation to make it a viable tool for rapid computation of vertical gravity and gravity gradiometry. I begin with a review of the vertical line element or VLE. I then show that by using a quadtree algorithm that I can subdivide the VLE to produce arbitrary accuracy. I calibrate the algorithm to model a standard spherical mass to test for accuracy and computational speed, and then apply it to a large regional study in Osage, Oklahoma. Although I specifically present workflows using gravity, this method also applies to other branches of potential field geophysics, as well as topographic and isostatic reductions in geodesy. Furthermore, I use the forward modeling algorithm, coupled with an inversion developed by Crain (2006), to demonstrate the potential of full-field modeling with periscopic observation points instead of equipotential surfaces.

## Theory

### *Vertical Line Mass Approximation*

Danes (1960) introduced vertical line elements (VLEs) to approximate a mass in order to efficiently calculate the effect of any vertical body. Building on this concept, SIGMA approximates rectangular prisms with vertical line at the prism axis, and calculates the gravity contribution of that VLE. The sum of the contributions from all the VLE used to model the mass distribution is the gravity effect of that body.

### *Methodology*

#### ***Vertical Line Element Definition***

I use two VLEs to approximate a finite-sized mass prism. Each VLE is defined by an area ($A \neq 0$), and a point in Cartesian coordinates, where $Z$ represents the top of the prism. The VLE is assumed to go down vertically from $Z$ to infinity. I calculate $g_Z$ using a unit density giving the Green's function for the semi-infinite prism. Using a unit density for forward calculations allows for modularity in combining various datasets, and simplifies iterations when reconciling the modeled volume with observed data iteratively as a density assignment is a trivial scalar multiplication, either subjective tests via residual analysis or objective iterations in an inversion.

#### ***Mass Volume from Vertical Line Elements***

A subtraction of the bottom VLE from the top VLE gives a finite volume (Fig. 38). This workflow creates a pseudo-prism or -layer using four parameters per VLE. The top VLE is defined by coordinates $X_t$, $Y_t$, $Z_t$, and its area, $A_t$. The bottom VLE is defined by coordinates $X_b$, $Y_b$, $Z_b$, and its area, $A_b$. The VLE from the top and bottom surfaces of a body or layer can be of varying spatial resolutions, but they both need to cover the same lateral area. The error from an areal mismatch is obvious if the top- and bottom-VLE have the same $(X, Y, Z)$; this case often presents itself when using a zero-length VLE, such as when mass layers pinch out. A zero-length VLE does not have a volume (or mass), so the gravitational contribution should be zero. If the top VLE has a larger area then the subtraction of the bottom VLE will result with a mass excess. If the bottom VLE has a larger area then the subtraction from the top VLE will result in a mass deficit.

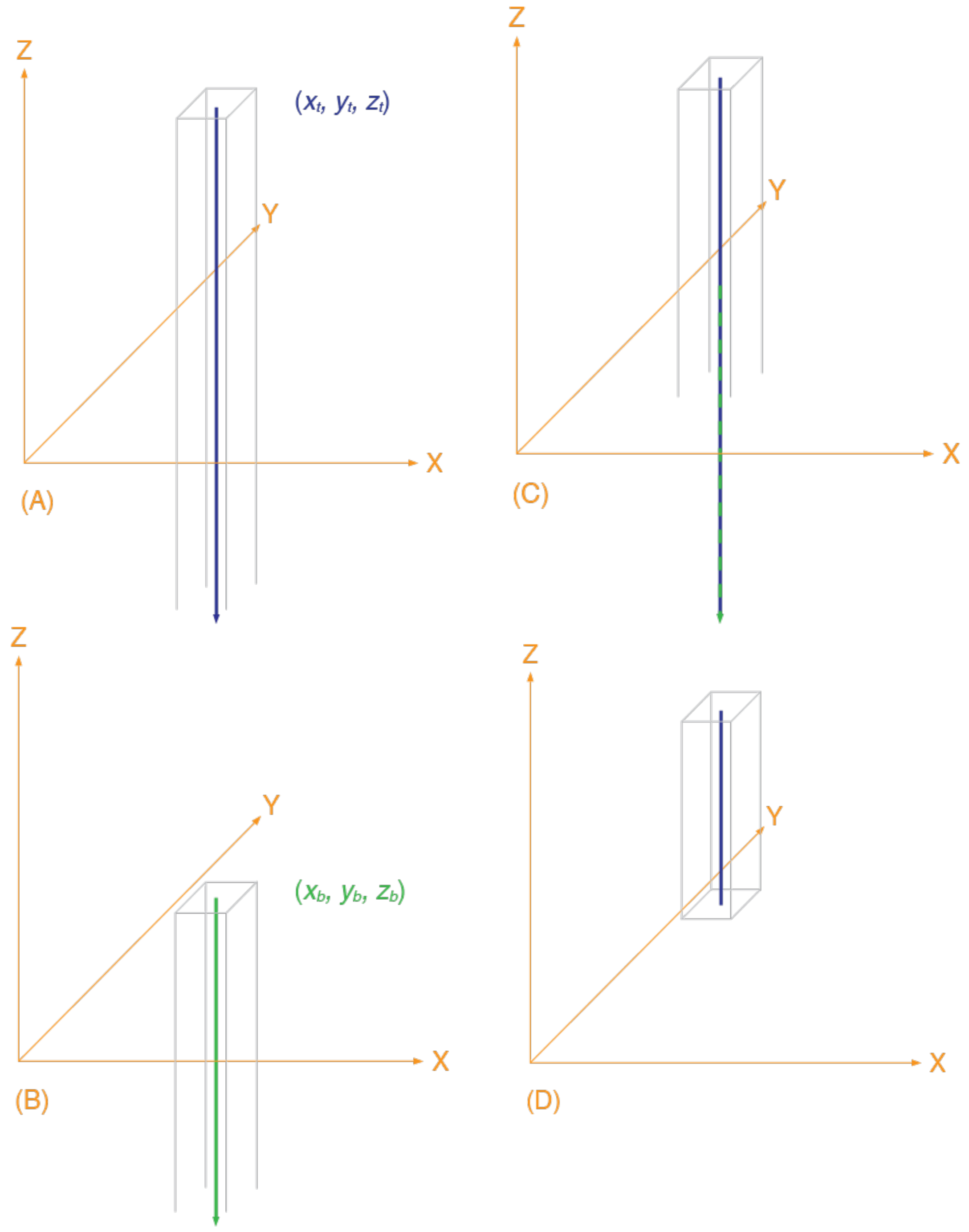

**Figure 38. Semi-infinite Vertical Line Elements**
Semi-infinite VLEs in Cartesian coordinates, with an assigned area and density, are used as proxies for masses that are being modeled. Shown here are two schematic lines that will be used to define a (A) “top” and (B) “bottom” of a mass; both lines extend down to infinity in Cartesian coordinates. (C) The bottom element is subtracted from the top element, relative to the observation point or station. (D) After the subtraction, what is left is a line of finite length, along with the associated area and density of the line, thus defining a finite mass within the model.

### *Highly Parallel Processing*

The calculated vertical gravity component, $g_Z$, for a mass defined by a VLE that extends to infinity is:

$$g_z = 0.00667 \frac{\rho A}{D}, \tag{5.2}$$

where $\rho$ is the density of the pseudo-prism, $A$ is the area that the VLE represents, and $D$ is the Euclidean distance from the observation point to the top of the VLE. In forward modeling, each point of observation is computed against each VLE in the model. Since the arithmetic operation on an observation point is independent to other observation points, the computational problem presents itself as highly parallel. Each VLE variable that defines the full topography (i.e., Cartesian coordinates and area, $A$) is placed into a matrix. Hence, Eq. (5.2) becomes a scalar matrix operation that is run in parallel, allowing SIGMA to run efficient computations.

### *Advantages and Disadvantages of Using Vertical Line Elements*

Cardenas and Ceberio (2012) hypothesized VLE to be more efficient at calculating 3D gravity. Danes (1960) predicted that it would be hundreds of times more efficient than calculating a comparable problem with prism mass elements. The typical drawback to efficiency is accuracy. Indeed, the this has been the Achilles heel of several mass approximation methods (Heck and Seitz, 2007; Wild-Pfeifer, 2008). With respect to the VLE mass approximation, Hammer (1974) demonstrated that the error introduced by such an approach increases as the observation point approaches the axis of the VLE (Fig. 39). This error seemed insurmountable as observation points taken on the surface being modeled, e.g., on the surface of the Earth, could not be reliably calculated, and the concept of using VLE mass approximation has since fallen out of favor.

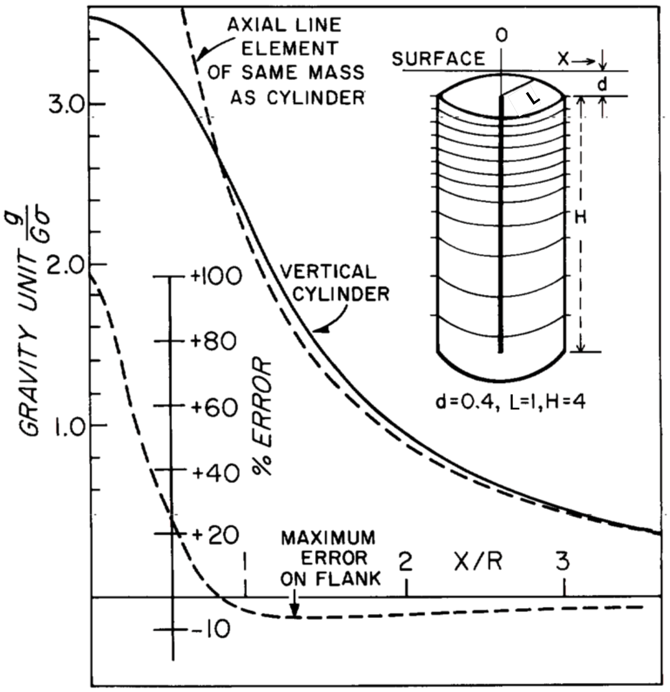

**Figure 39. Errors from Using Vertical Line Mass Elements (from Hammer, 1974)** Gravity calculations are sensitive to the distance (X) between observation point and vertical line element, and the radius (L, which is also related to the horizontal-sectional area) of the cylinder that the vertical line element represents. Eq. (2) shows that a station being mathematically zero distance away from the top of a VLE will cause the calculated gravity effect to be infinite.

## Numerical Implementation

### *Gravitational Potential of a Point Source*

I start by isolating the gravity meter at the observation point, located at the observation point and the mass(es) affecting it that I will represent with a VLE. The attraction of the mass at the observational point to mass represented by the VLE is described by Newton's law of universal gravitation in vector form as

$$\vec{\mathbf{F}} = -\mathrm{G}\frac{\mathrm{m_{OP}}\,\mathrm{m_{VLE}}}{\mathrm{R}^2}\,\hat{\mathbf{r}}\,, \tag{5.3}$$

where $\vec{\mathbf{F}}$ is the force experienced by the instrument mass, $m_i$ at the Cartesian coordinates of the observation point, $(x, y, z)$, caused by the mass of the VLE, $m_{VLE}$, at distance $R$, $G$ is the universal gravitational constant, and $\hat{\mathbf{r}}$ is a unit vector pointing the opposite sense of the force.

The gravitational field, $\vec{g}$, at the observation point is given by

$$\vec{g}(x, y, z) = \frac{\vec{F}}{m_i} = -G\frac{m_{VLE}}{|\vec{R} - \vec{R}_o|^2}\,\hat{r}\,. \tag{5.4}$$

Assuming the $\vec{g}$ generated by $m_{VLE}$ is isotropic, meaning the gravity field from $m_{VLE}$ is the same at any point in Cartesian space that is $R$ distance away, then the observed gravitational field, $\vec{g}$, at any observation point, $(x, y, z)$ is

$$\vec{g}(x, y, z) = -G\frac{m_{VLE}}{|\vec{R} - \vec{R}_o|} = -G\frac{m_{VLE}}{\sqrt[2]{(x-x_0)^2 + (y-y_0)^2 + (z-z_0)^2}} \tag{5.5}$$

for any $m_{VLE}$ at Cartesian coordinates $(x_0, y_0, z_0)$.

For simplicity, I substitute the gravity components of the infinitesimal point source at the observation point are determined by taking the negative gradient of the gravitational potential at the observation point, thus

$$\vec{g}(x, y, z) = -\nabla U(x, y, z)\,, \tag{5.6}$$

or

$$\begin{aligned} g_x &= -\frac{\partial U}{\partial x} \\ &= -\frac{\partial}{\partial x}\left\{-G\, m_{VLE}\frac{1}{\sqrt[2]{(x-x_0)^2 + (y-y_0)^2 + (z-z_0)^2}}\right\} \\ &= -G\, m_{VLE}\frac{(x-x_0)}{\aleph^3}\,, \end{aligned} \tag{5.7}$$

$$g_y = -G\, m_{VLE}\frac{(y-y_0)}{\aleph^3}\,, \tag{5.8}$$

and

$$g_z = -G\, m_{VLE}\frac{(z-z_0)}{\aleph^3}\,. \tag{5.9}$$

The gravity tensor components due to the point source are determined by taking the gradient of the gravity components. Assuming that neither the observation point nor the point source is accelerating with respect to each other, then the gravity tensor can be written as

$$g_{xx} = \frac{\partial g_x}{\partial x}$$

$$= \frac{\partial}{\partial x}\left\{-G\, m_{VLE} \frac{(x-x_0)}{[(x-x_0)^2 + (y-y_0)^2 + (z-z_0)^2]^{\frac{3}{2}}}\right\}$$

$$= -G\, m_{VLE} \frac{-2(x-x_0)^2 + (y-y_0)^2 + (z-z_0)^2}{\aleph^5}$$

$$= -G\, m_{VLE} \frac{3\left(\frac{x-x_0}{\aleph}\right)^2 - 1}{\aleph^3} \,, \tag{5.10}$$

$$g_{xy} = \frac{\partial g_x}{\partial y}$$

$$= \frac{\partial}{\partial y}\left\{-G\, m_{VLE} \frac{(x-x_0)}{[(x-x_0)^2 + (y-y_0)^2 + ]^{\frac{3}{2}}}\right\}$$

$$= -G\, m_{VLE} \frac{3\left(\frac{x-x_0}{\aleph}\right)\left(\frac{y-y_0}{\aleph}\right)}{\aleph^3} \,, \tag{5.11}$$

$$g_{xz} = \frac{\partial g_x}{\partial z}$$

$$= \frac{\partial}{\partial z}\left\{-G\, m_{VLE} \frac{(x-x_0)}{[(x-x_0)^2+(y-y_0)^2+(z-z_0)^2]^{\frac{3}{2}}}\right\}$$

$$= -G\, m_{VLE} \frac{3\left(\frac{x-x_0}{\aleph}\right)\left(\frac{z-z_0}{\aleph}\right)}{\aleph^3} \,, \tag{5.12}$$

$$g_{yy} = \frac{\partial g_y}{\partial y}$$

$$= \frac{\partial}{\partial y}\left\{-G\, m_{VLE} \frac{(y-y_0)}{[(x-x_0)^2 + (y-y_0)^2 + (z-z_0)^2]^{\frac{3}{2}}}\right\}$$

$$= -G\, m_{VLE} \frac{(x-x_0)^2 - 2(y-y_0)^2 + (z-z_0)^2}{\aleph^5}$$

$$= -\mathrm{G}\,\mathrm{m}_{\mathrm{VLE}}\,\frac{3\left(\frac{\mathrm{y}-\mathrm{y}_0}{\aleph}\right)^2 - 1}{\aleph^3}\ , \tag{5.13}$$

$$\mathrm{g}_{\mathrm{yz}} = \frac{\partial \mathrm{g}_{\mathrm{y}}}{\partial \mathrm{z}}$$

$$= \frac{\partial}{\partial \mathrm{z}}\left\{-\mathrm{G}\,\mathrm{m}_{\mathrm{VLE}}\,\frac{(\mathrm{y}-\mathrm{y}_0)}{[(\mathrm{x}-\mathrm{x}_0)^2+(\mathrm{y}-\mathrm{y}_0)^2+(\mathrm{z}-\mathrm{z}_0)^2]^{\frac{3}{2}}}\right\}$$

$$= -\mathrm{G}\,\mathrm{m}_{\mathrm{VLE}}\,\frac{3\left(\frac{\mathrm{y}-\mathrm{y}_0}{\aleph}\right)\left(\frac{\mathrm{z}-\mathrm{z}_0}{\aleph}\right)}{\aleph^3}\ , \tag{5.14}$$

and since there is no relative acceleration between $m_i$ and $m_{VLE}$, then

$$\mathrm{g}_{\mathrm{xx}} + \mathrm{g}_{\mathrm{yy}} + \mathrm{g}_{\mathrm{zz}} = 0$$

such that

$$\mathrm{g}_{\mathrm{zz}} = -\mathrm{g}_{\mathrm{xx}} - \mathrm{g}_{\mathrm{yy}}\ . \tag{5.15}$$

### *Volume and Mass from a Vertical Line*

Using Equations (5.9-5.15), I integrate through a vertical line starting at the top of the VLE $(x_0,\ y_0, z_0)$. After subtracting the bottom-VLE from the top-VLE, the resulting VLE has a finite length. The residual length of the VLE, and the area assigned to the VLE, $A$, yields a volume. This volume, multiplied by the density assigned in Eq. (5.2), $\rho$, yields the mass distribution of the finite VLE. Although I used a square area for simplicity, as it is the default element in a DEM, it is possible to define the area in other shapes, as long as the top and bottom surfaces of the source-body being modeled are fully tessellated.

### *Quadtree Method in SIGMA*

The errors associated with the VLE mass approximation decrease as the ratio $L/X$ decreases (Fig. 39). I embedded a quadtree method in SIGMA to circumvent this mathematical limitation (Fig. 40). I then validate SIGMA's accuracy against closed form analytical solutions of simple models. The error arises when the point of observation point at $(x, y, z)$ is close to the VLE-top, $(x_0,\ y_0, z_0)$. I solved this issue using a quadtree method of quartering the offending topography-cell to have smaller areas with four new VLEs. Out of the four new VLEs, one will have a $L/X$ ratio > 1, which becomes the new offending VLE. The quadtree process is repeated until the error diminishes sufficiently. Dividing the VLE to quarter-VLEs does not eliminate the erroneous $g_Z$ contribution thrown by the closest VLE, but diminishes the error by orders of magnitude, to the point where it is virtually indistinguishable from other sources of noise. I tested the quadtree division up to 256 iterations, and found the error limit of 64-bit double precision, or $10^{-15}$.

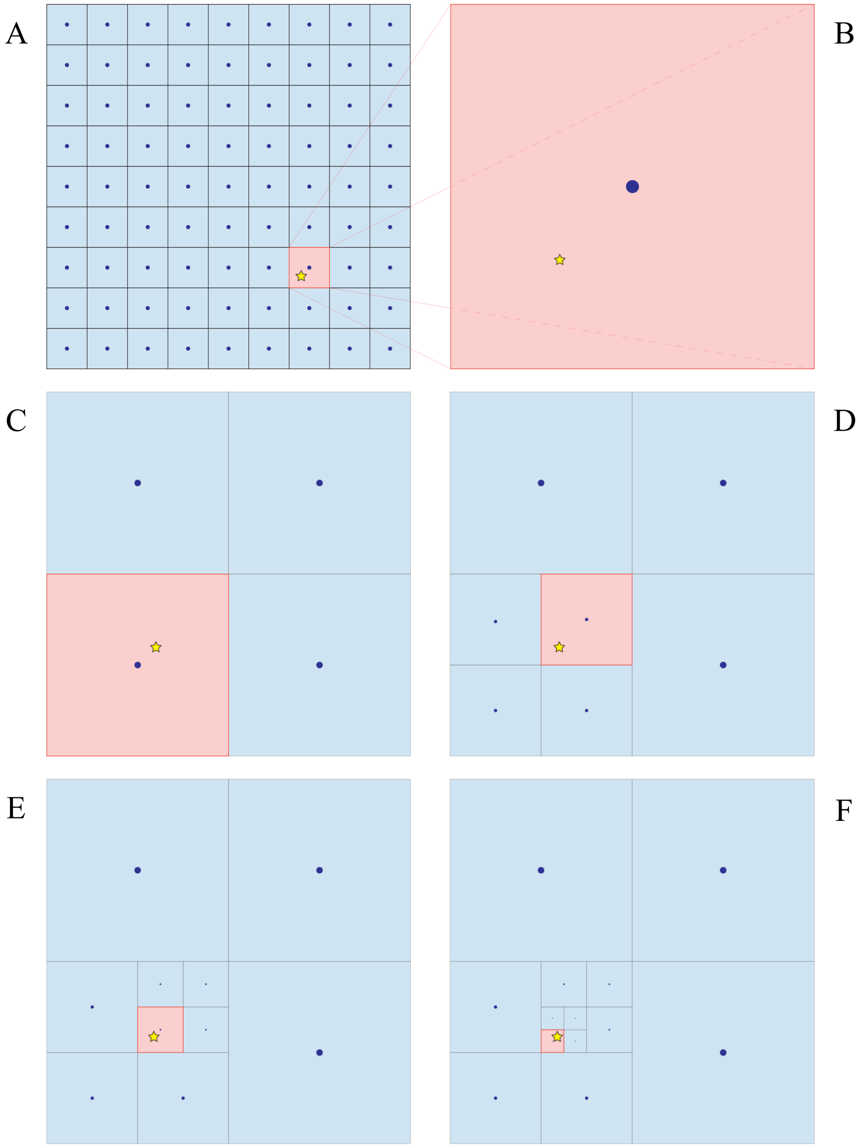

**Figure 40. Visualization of the Quadtree Division in SIGMA**
(A) Map view of terrain grid squares, VLE circles, and station location (star). A unit elevation grid cell gives erroneous results (red), due to its proximity of the station relative to the VLE—this occurs when the station is within the area that the VLE represents. Cells yield accurate results (blue), if $\boldsymbol{L/X < 1}$, or the cells are far away from the station (Fig. 38). Relative contribution of the VLE is shown by the relative size of the circle in the centroid of the cell. (B) Isolated cell from *A* that gives erroneous computational results. (C) First division of the quadtree pattern. The unit cell is divided into four quarters. These daughter cells represent the equivalent mass of the original unit cell when summed. Each quarter-cell has its own new VLE coordinates. Upon computation of the entire area, only a quarter of the original unit cell yields erroneous results. (B-F) Multiple quadtree divisions are done on the subsequent daughter cells until the erroneous contribution to the summed result is no longer significant.

# Application

## *Case 1: Gravity Effect of a Sphere*

### ***Standard Sphere Test***

To validate the accuracy of the method, I tested the accuracy of SIGMA against an analytical solution, using a commonly used standard sphere. I used a 500 m radius sphere of unit density, centered at the elevation $Z_S$ = 2,040 m, with station elevations held constant at elevation $Z_{obs}$ = 2,640 m. This model analytical solution for $g_z$ was chosen as a benchmark by Bell Geospace, a commercial firm specializing in processing gravity and gravity gradiometry. They used a station spacing of 10 m, covering the same 1 km x 1 km lateral footprint as the sphere (Fig. 41).

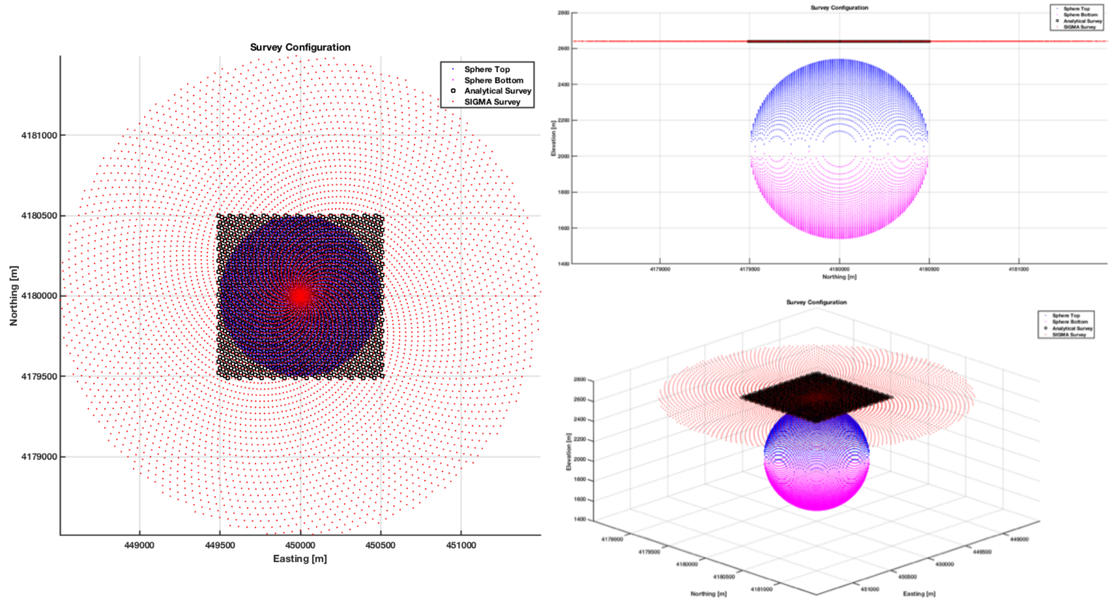

**Figure 41. Standard Test Sphere for Gravity Calculations**
Survey configuration of sphere test used in analytical vs. SIGMA comparison. The 500 m radius sphere (blue = top, magenta = bottom) is centered an elevation of 2,040 m. Analytical results were computed independently by Bell Geospace for the same size sphere, with stations covering 1 km x 1 km area, with 10 m spacing between each station (black dots), at a constant elevation of 2,640 m. SIGMA stations (red dots) were calculated at the same center and elevations as Bell Geospace, but extended to 1500 m laterally.

## ***Discussion***

### Accuracy of the Results

I modeled the same standard sphere and station elevations using SIGMA, with a radially distributed station spacing of a 1500 m radius survey footprint. I compared the SIGMA results with the analytical standard sphere results from co-located stations, and found maximum differences of less than 0.005% for $g_z$ (Fig. 42). No singularities were observed in any of our testing at various scales. We conclude that the quadtree division implemented in SIGMA was sufficient in minimizing the systematic errors identified by Hammer (1974), to be sufficient evidence that the errors an observation point being too close to a VLE were skirted by the quadtree method embedded in SIGMA.

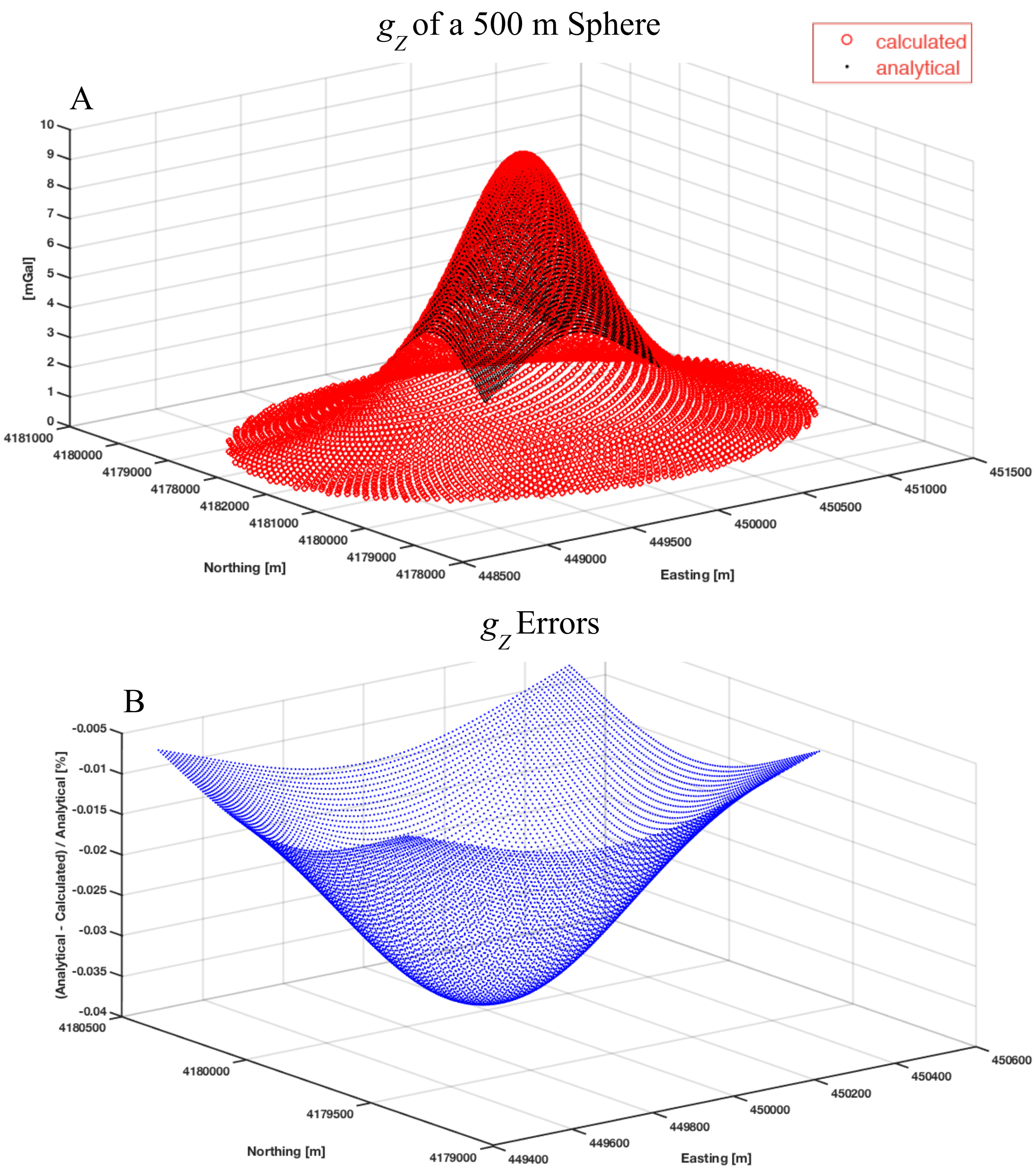

**Figure 42. Analytical vs. SIGMA Results**

Analytical vs. SIGMA-calculated results for $g_Z$. (A) Analytical solution (black dots) and SIGMA results (red open circles) from a 500 m sphere. (B) Shows the percent error (blue dots) for each co-located stations—none more than 0.005% from the analytical solution.

### Computational Speed

I used the sphere in Figure 41 to test the computational efficiency of SIGMA against the standard prism mass approximation defined by Nagy *et al.* (2000 and 2002) and compared it to the normalized results compiled by Wild-Pfeifer (2008). The model parameters include a sphere comprising 7,825 square prisms of varying heights, and 65,536 observation points (or gravity stations). Each square prism requires a pair of VLE, one for the top and another for the bottom, to model the same mass equivalent. Hence a total of 15,650 VLE were used in this model. I used the same desktop workstation for both tests, running a Windows 10 64-bit operating system on Intel Core i7-3770 CPU at 3.40 GHz with 32 GB of RAM. The time to compute a $g_z$ for the prism mass approximated sphere was over 52 hours. The time for SIGMA to compute the same $g_z$, on the same computer, was less than 5.6 s. The SIGMA implementation of the VLE is on average 33,000 times more efficient than the prism calculation.

## *Case 2: Modeling a Gravity High in Osage, Oklahoma*

### ***Osage Gravity High***

The Osage Anomaly is a gravity high that was first mentioned by Cook (1954), and noted by Denison (1981) as being difficult to correlate to the known geology. A regional Free Air Anomaly (FAA) map shows that known continental rift structures show up as gravity highs (Fig. 43A), due to the denser basaltic rocks intruding less-denser crust. The Osage Anomaly is puzzling in that there is no known source for rocks that might produce the observed gravity high. In this work, we construct a preliminary model to determine the extent of the source for the Osage Anomaly. The interpretation of the Osage Anomaly to a geologic history has been reported by Crain and Keller

(2013). In this paper, I obtained Crain and Keller’s (2013) Osage Anomaly and used it as an example of how SIGMA may be used in iterative gravity modeling.

### ***Motivation***

Substantial increases in seismicity across northcentral Oklahoma in the last decade have been generally attributed to human activity (see Chapter 4). During the last oil and gas boom, the Cherokee Platform was generally targeted by many energy companies. However, these new production wells yielded sometimes as much as 90% (or more) formation saltwater, along with hydrocarbons, which was commonly disposed of into deeper formations of the Arbuckle aquifer. Wastewater injection into the Arbuckle Group, which directly overlies crystalline basement, has been proposed to hydraulically or elastically perturb the stresses on basement faults, causing them to slip.

An Oklahoma seismicity map shows Osage County as an anomalously “quiet” region. Seismicity in counties surrounding Osage County experienced hundreds of earthquakes during 2014-2016, yet the area of Osage experienced less than a dozen earthquakes in the decades-long history of the Oklahoma seismic network. This is surprising since the fundamental geologic settings and possible anthropogenic triggers are essentially the same for these seismically active and quiet areas. Here, we use gravity to model the crystalline basement beneath Oklahoma to investigate how Osage differs from its neighboring areas.

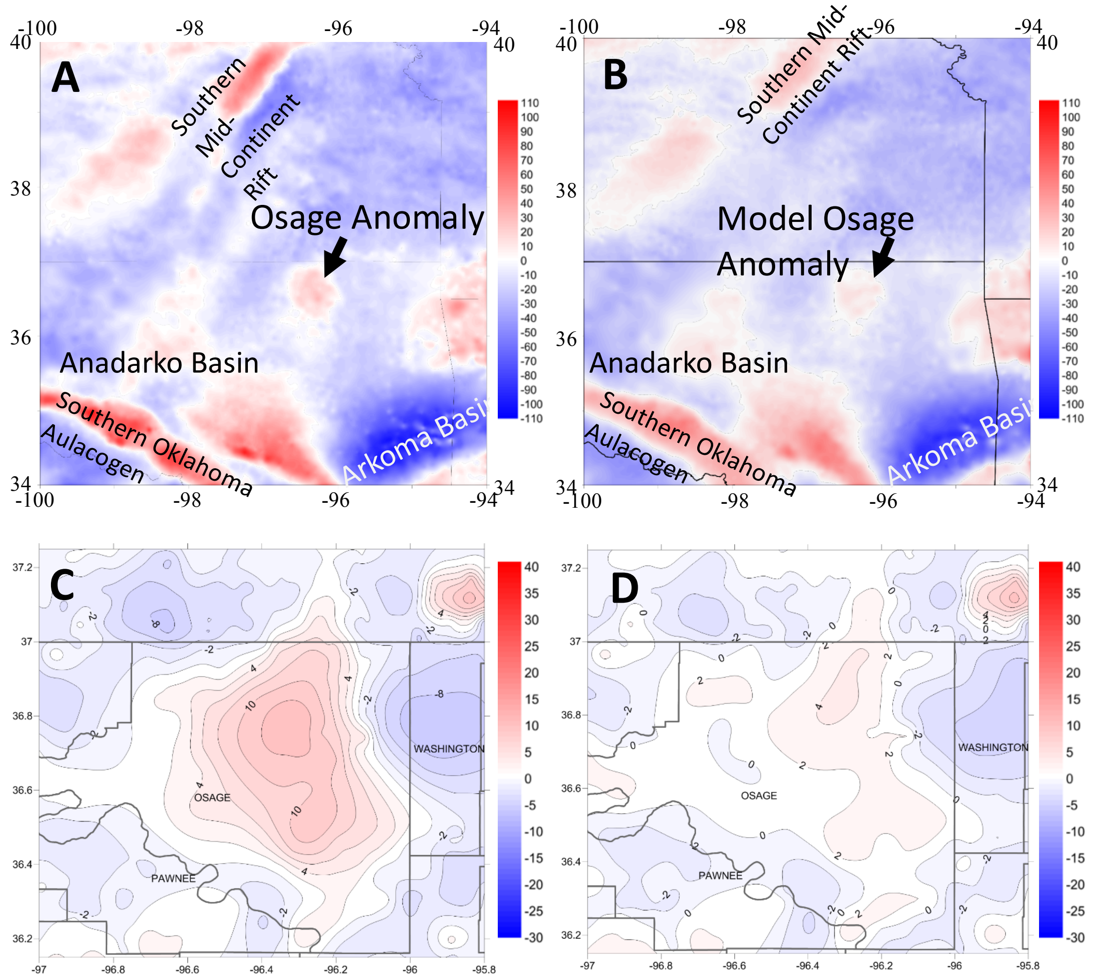

**Figure 43. Free Air Anomaly Maps**
(A) Observed Free Air Anomaly (FAA) map. (B) Modeled FAA map, using only mass distributions in layers A-E described in text and in Figure 44. (C) Close up view of the residual FAA between the observed and modeled FAA, with counties outlined for reference. (D) Close up view of the residual FAA after accounting for the additional mass in the upper crust beneath Osage County, with counties outlines for reference. Mapped colors are in mGal.

### *Regional Mass Distribution in Subsurface Layers*

We model the Osage Anomaly using five mass layers (Fig. 44): (A) the sedimentary package at 2.54 g/cm$^3$, from the surface topography to the top of crystalline basement; (B) the upper crust 2.67 g/cm$^3$, from top of the crystalline basement to 16 km below mean sea level (BMSL); (C) the mid-crust 2.79 g/cm$^3$, from 16 km BMSL to 24 km BMSL; (D) the lower crust 2.79-3.00 g/cm$^3$, from 24 km BMSL to 42 km BMSL; and (E) the upper mantle 3.20-3.40 g/cm$^3$, from 42 km BMSL to 100 km BMSL. The lateral extent of the whole model is 10° latitude x 10° longitude. The sedimentary package, modeled at 1 asec grid-resolution, uses almost 2.6 billion VLE for the entire layer. The lower four mass layers, modeled at 30 asec, uses over 11.5 million VLE combined.

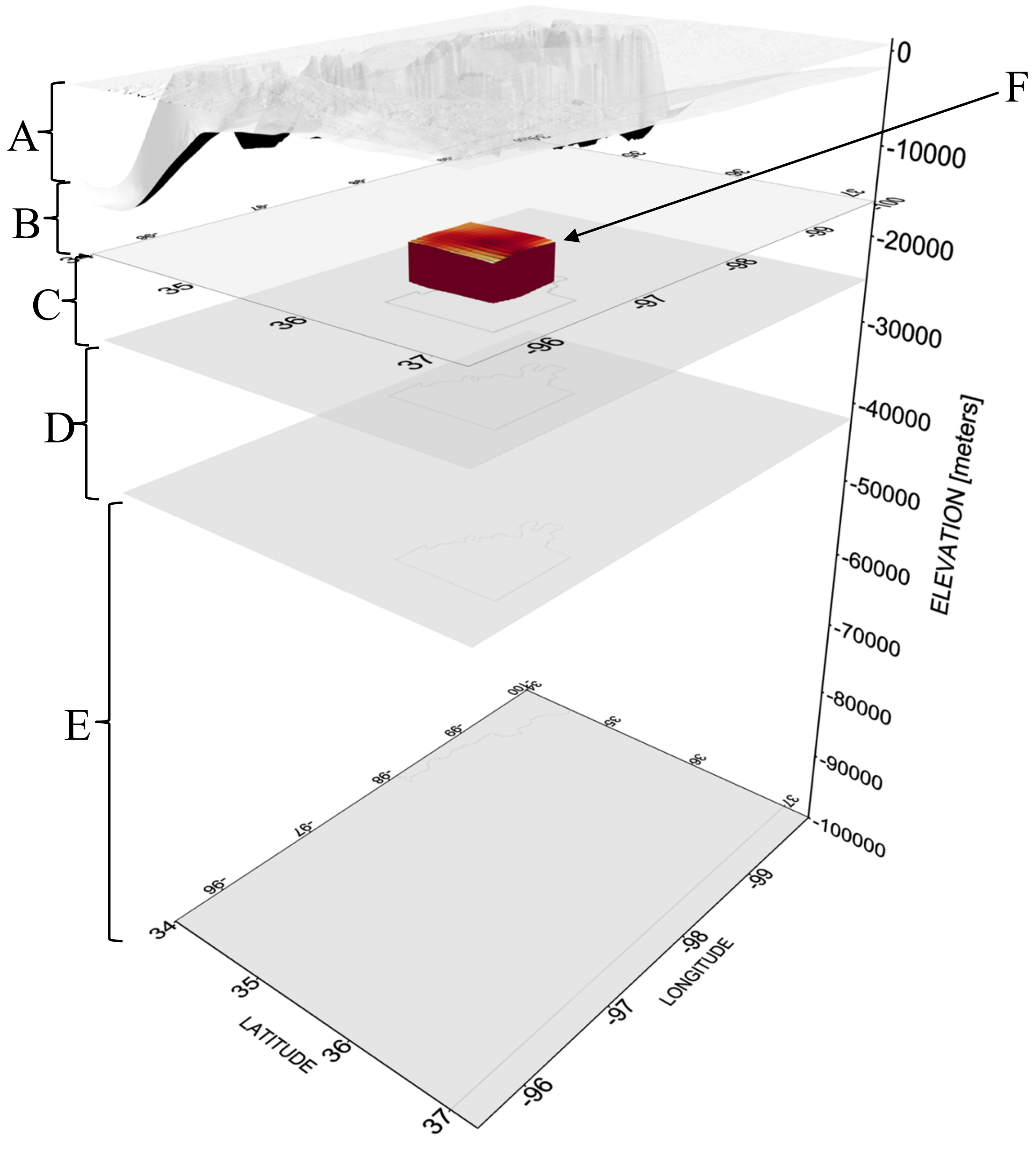

**Figure 44. Osage Anomaly Density Model**
Perspective view, looking towards the southwest of a cropped view of the Osage density model. Only top and bottom surfaces are shown of the VLE layers for visual clarity. (A) Variable thickness sedimentary package, above the crystalline basement; (B) upper-crustal layer; (C) mid-crustal layer; (D) lower-crustal layer; (E) upper-mantle layer; (F) additional mass distribution added to account for discrepancies in the residual gravity between the observed gravity and the SIGMA-calculated gravity.

### *Residual Modeling*

We calculate the model described above to account for the Free Air Anomaly (FAA) of the regional gravity from 8193 observation points (Fig. 8). The residual FAA for the Osage area shows that the regional mass distribution did not fully account for the observed FAA by +/- 12 mGal (Fig. 8C). With a qualitative magnetic analysis, we determine that the unaccounted mass is likely above the Curie depth, and computed an additional mass in the upper crust to account for the FAA discrepancy (Fig. 7F). The additional volume has a density of 2.87 g/cm$^3$, laterally extends approximately 78 km x 67 km, with an average thickness of 3.8 km. This additional mass brings the residual FAA down to +/- 4 mGal (Fig. 8D). With every new iteration, we can modularly add or subtract masses to account for overages or deficits in the residual gravity.

### *Discussion*

Modeling the Osage Anomaly shows how we can modularly forward model the geology using several iterations of adding (or subtracting) mass distributions to get the modeled FAA gravity to match the observed FAA gravity. In this case, we modeled the regional mass distribution to account for the large-scale gravity observation, then we modeled a mass body in the mid-crust to account for the Osage Anomaly. The residual FAA (Fig. 40D) suggests that not all the masses, which produced the observed FAA, are accounted for. Thus, the next iteration would be to model smaller mass bodies to lessen the residual difference between the observed FAA and the modeled FAA.

Even though we demonstrate how SIGMA can fit in typical gravity modeling workflow, processing the sedimentary layer used in the Osage model, with almost 1.3

billion prisms to achieve the equivalent resolution, would take almost 20 weeks to compute if we linearly extrapolate the test conditions in Case 1.

The iterative approach in the modeling the Osage Anomaly could benefit from an inversion to minimize the misfit between the observed FAA and modeled FAA. The speed and accuracy of SIGMA to model gravity is clear, but I hypothesize that using gravity data points that observe the mass distribution from different perspectives can significantly reduce the non-uniqueness of the inverse problem. In the following case, I will explore a new way to model gravity by inversion of heterogeneous gravity data.

### *Case 3: Full-Field Modeling*

### ***A New Approach to 3D Gravity Modeling***

I liken gravity readings taken at the Earth's surface to an observer seeing a distant object with monoscopic vision. It is difficult to determine the true size and distance of a distant object due an infinitely possible combination of size and distance that will produce the same observation (Fig. 45). If there were at least two observers orthogonally oriented to the object communicating with each other, then determining the true size and shape would be much more constrained. This is essentially how gravity has been modeled with conventional approaches—all the observation data are on one side of the masses being modeled (Fig. 46-47). I extend this approach to gravity modeling, where I test the postulation with a synthetic mass distribution and hypothetical data collected on the surface, in the air, and underground.

### ***Conventional Gravity Data***

Gravity data from different types of surveys are typically not modeled concurrently. The most common type of gravity survey is a land-based reading with a surface gravimeter that observes the vertical component of gravity, $g_Z$, with units in mGals. A more sophisticated type of survey is gravity gradiometry, which observes the full gravity tensor, $g_{xx}$, $g_{xy}$, $g_{xz}$, $g_{yy}$, $g_{yz}$, and $g_{zz}$, with units in eotvos (abbreviated as E). Gravity gradiometry surveys are typically airborne or marine; typically, only $g_{zz}$ data are used in modeling gravity gradiometry, because the other tensors are not intuitive (Ben Drenth, personal communication, August 25, 2015). The borehole gravity survey is similar to common land surveys, but the gravity meter is now placed down a well, and the gravity readings are taken at different downhole intervals. Smith (1950) first proposed the use of gravity meters down a well, and touted its many uses, but not one of them was to model gravity. Decades later, combining borehole $g_Z$ observations with a land $g_Z$ observations is still not done with conventional modeling techniques (Brady *et al.*, 1993; Ander and Chapin, 1997). The typical use for borehole gravity measurements is to derive limited density information between the downhole observation points (e.g., Brady *et al.*, 1993). At the time of writing, there is no known method that combines data from these different types of gravity surveys.

### ***Periscopic Analysis***

It is often stated that the gravity method provides non-unique solutions, meaning that the observed gravity can be modeled using different possible mass distributions. Figure 46 illustrated the commonly cited scenario of a gravity effect from a deeply buried sphere matching the gravity effect from a shallower boudin-shaped body that is less than that of the sphere (Saltus and Blakely, 2011). This statement is true for some cases. If we take the same two mass distributions of the sphere and boudin-shaped body and turn it on its side, the surface gravity effects will reflect this new mass distribution

(Fig. 47). I posit that the entire gravity field, as a whole, is a unique result of mass distribution in space. If gravity can be observed in more relative dimensions, more constraints can be put on modeling the mass distribution that produced the observed gravity.

### ***Point Data Modeling***

Intrinsic in SIGMA is modeling data at the point in which they are observed. SIGMA computes a scalar mGal or eotvos value for vertical gravity or gravity gradient, respectively. This means that SIGMA can combine data from different surveys and model them concurrently. The computed results can be used in any inversion, but I use the inversion developed by Crain (2006) as it can constrain the inverted model and data using their natural units (*i.e.*, g/cm$^3$ for the model, and mGal or eotvos for the gravity data). With this workflow, the periscopic scenario depicted in Figure 45 is possible (Fig. 48). In this case study, I generate a synthetic model with highly heterogeneous density distribution, calculate hypothetically observed data from a typical land-gravity survey, airborne gravity gradiometry survey, and borehole survey. As a test to see if the inversion can resolve the synthetic density distribution for the hypothetically observed data, I use a homogeneous model as the *a priori* model to the inversion.

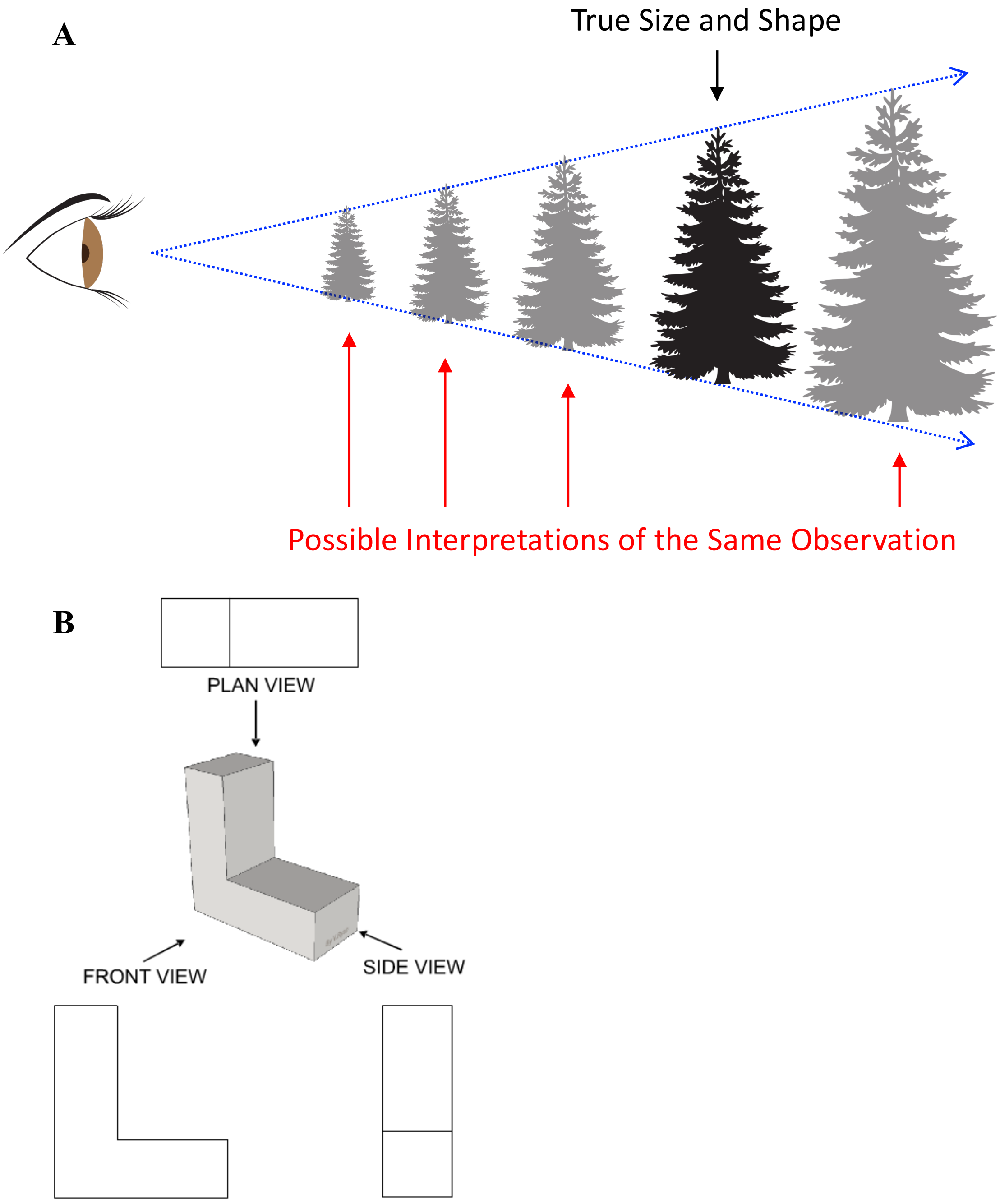

**Figure 45. Monoscopic vs. Periscopic Vision**
(A) Schematic diagram of an observer with monoscopic vision, which results in more than one possible interpretation of the same observation. (B) Example of periscopic vision: viewing the same object from multiple angles better constrains its true shape and size.

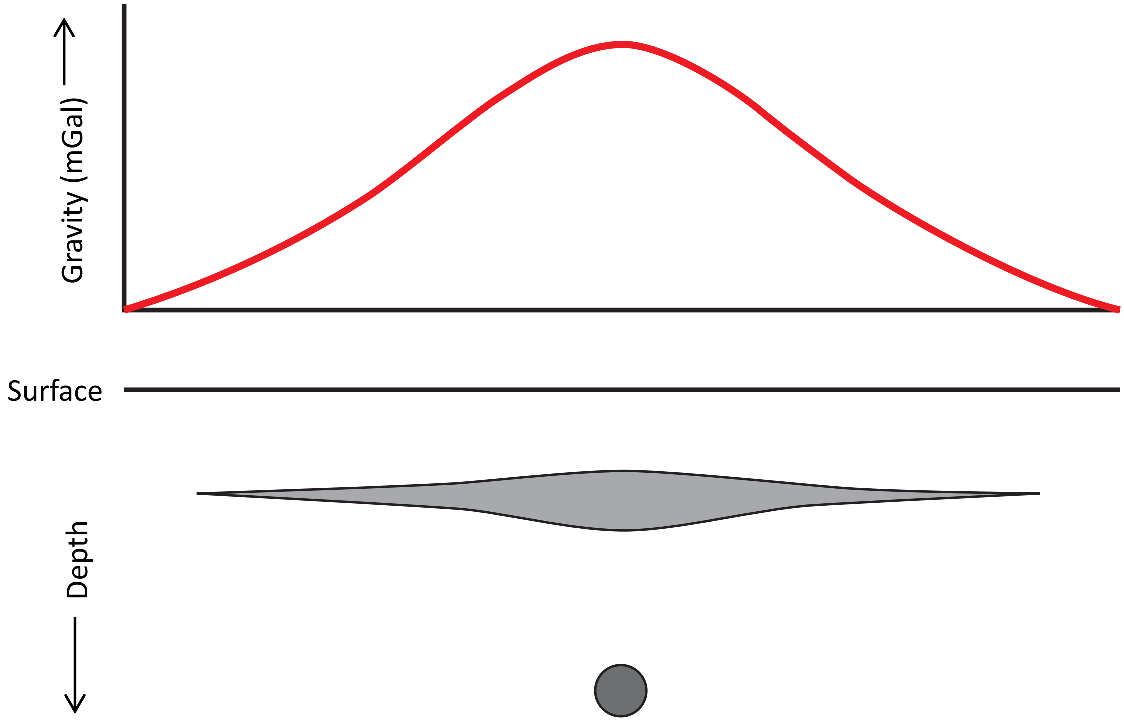

**Figure 46. Ambiguity in Gravity Observations**
Classical schematic cross-section showing ambiguity in gravity solutions (modified from Saltus and Blakely, 2011). A deeply buried dense spherical mass body can produce the same surficial gravity profile (red line) as a shallower boudin-shaped mass body with less density, in addition to other combinations of shape and density. Thus, modeling the true mass distribution from surficial observation is impossible without independent constraints. Note that this diagram is scale independent.

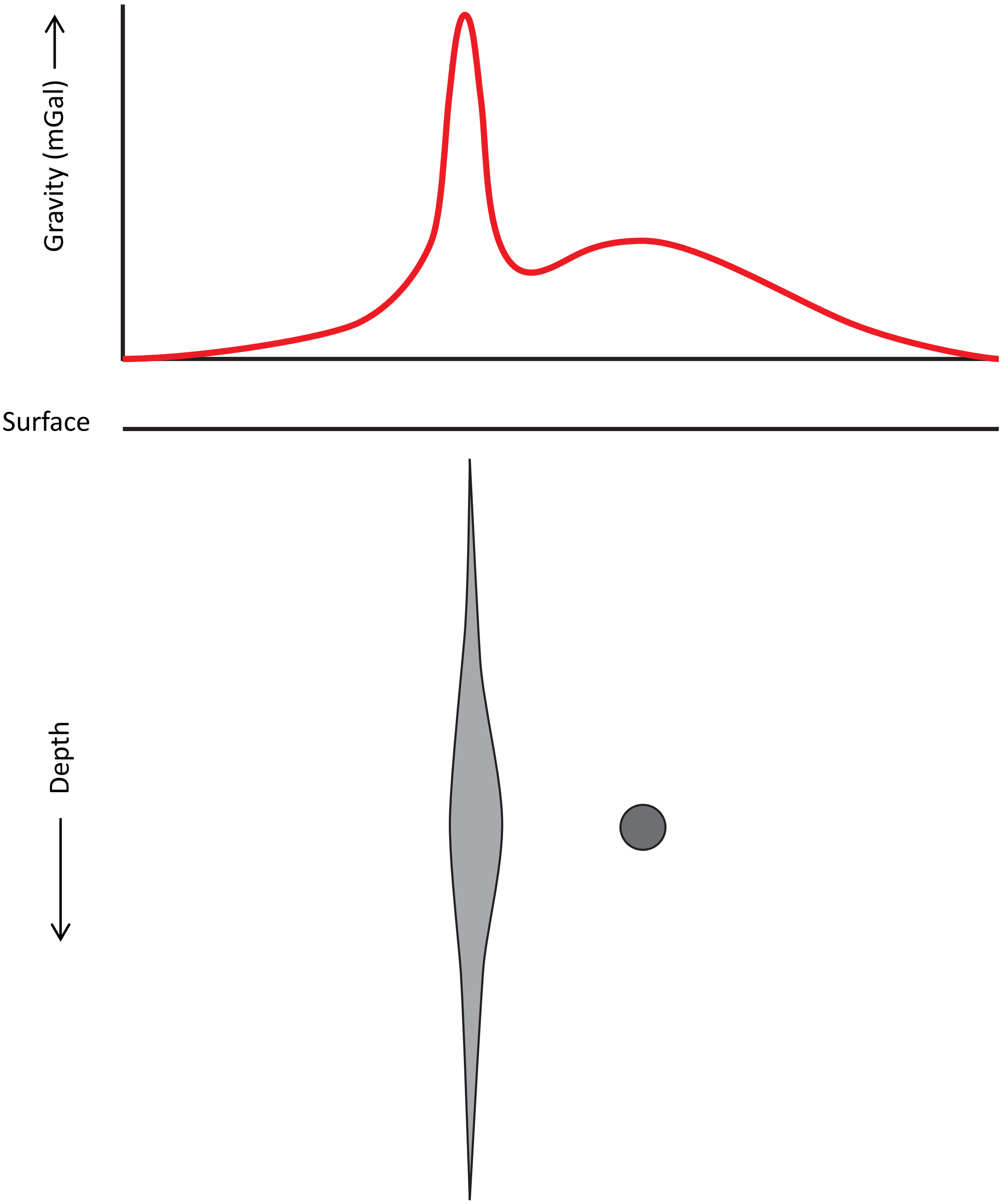

**Figure 47. Classical Mass Bodies from a Different Perspective**
Schematic cross-section of classical gravity model in Figure 45 that has been rotated counterclockwise. The combined gravity effects from both bodies are depicted in the surficial gravity profile (red line). This shows that the two bodies in this orientation have different profile signatures due to their mass distribution. Note that this diagram is scale independent.

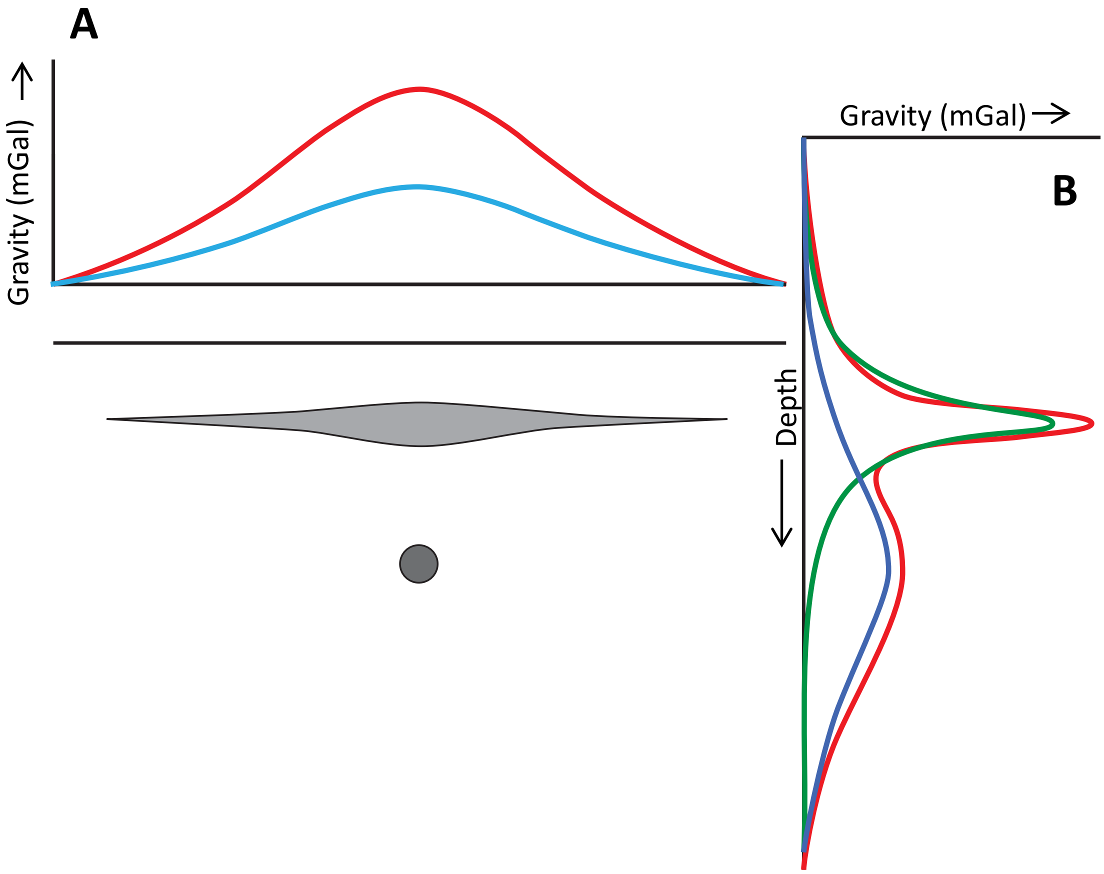

**Figure 48. Using Different Gravity Observations to Delineate Mass Bodies**
Schematic cross-section of a deeply buried spherical mass body and a boudin-shaped mass body. (A) Schematic surficial gravity profile: red line shows the expected gravity profile if both mass bodies were present; cyan line shows the expected gravity profile if either mass body is present. (B) Schematic vertical gravity profile: red line shows the expected gravity profile if both mass bodies were present; blue line shows the expected gravity profile if only the sphere mass body was present; green line shows the expected gravity profile if only the boudin-shaped mass body was present. Combining these orthogonal gravity observations shows how I can better delineate different scenarios: (1) if I observe the cyan and blue profiles, then it must be a buried spherical mass body; (2) if I observe the cyan and green profiles, then it must be a buried boudin-shaped mass body; (3) if I observe both red profiles, then it must be both mass bodies; (4) if I observe the red surficial profile and the green depth profile, then it must be a denser boudin-shaped body; (5) if I observe the cyan surficial profile and red depth profile, then it must mean both bodies are less dense, and so forth. Note that this diagram is scale independent.

## ***Generating Synthetic Data***

### *Mass Distribution of the Synthetic Volume*

I mapped the heterogeneous mass distribution in Figure 40 using data from a real rock. I used the density distribution from XRCT scans of a 1-inch plug of Haynesville Shale (cf., Elmore *et al*., 2016). Values from the XRCT scans were assigned densities. Then the scans were re-mapped to a 4.6 km x 4.6 km x 1.8 km (length x width x height, respectively) block to represent a typical target for a local gravity survey. The volume has 1074 discrete densities, spread over 371 million 10 m x 10 m x 1 m (length x width x height, respectively) elements. This is similar to a checkerboard test used in tomographic inversion (Leveque *et al.*, 1993), except the checkerboard in this case has: (1) randomly sized shapes; (2) 1074 discrete answers, instead of 1's and 0's; (3) random distributions of the discretized answers in three dimensions.

### *Synthetic Observations*

I used the mass distribution described above to calculate synthetically observed data for four different surveys: surface acquisition, airborne acquisition, and borehole acquisition (Fig. 49-50). These data points represent currently available methods of collecting gravity data, and their acquisition parameters are typical parameters for their respective survey type. The survey parameters and synthetic observations given below are not exact due to added random noise, which I introduced to replicate real world measurements.

The land survey comprises $g_Z$ field observations 0.025-0.525 m above the surface of the mass distribution (sea level in this case). The area covers 30.5 km x 30.5

km, with a lateral station spacing of approximately 500 m. The land survey extends past the target volume to account for edge effects. Observational units are in mGal.

The air survey is typical of a six-component airborne gravity gradiometry survey. Flight lines for the run east-west and 125 m (+/- 10 m) apart, with observations taken at 30 m (+/- 5 m) intervals. The six components from a gradiometry survey are $g_{xx}$, $g_{xy}$, $g_{xz}$, $g_{yy}$, $g_{yz}$, and $g_{zz}$. Observational units are in eotvos.

The vertical and inclined borehole have station intervals of 1 m (+/- 0.5 m) in depth. The vertical measurements start from the surface to 2k m depth. The inclined borehole has a total length of 5031 m, and approximately trends 116º and plunges 19º. Observational units are in mGal for both surveys.

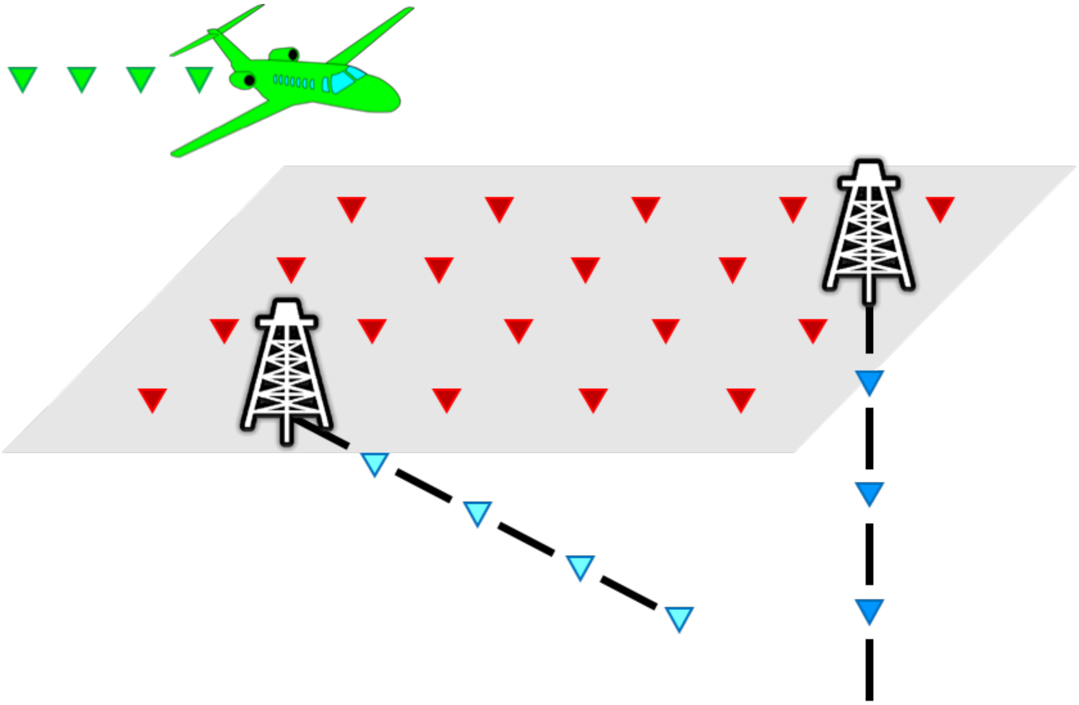

**Figure 49. Schematic Diagram the Synthetic Survey Design**
Schematic illustration of the types of gravity surveys used in the synthetic model. Triangles illustrate data points that correspond with Figure 52: red for land survey; green for the airborne gravity gradiometry survey, cyan for the diagonal borehole survey; and blue for the vertical borehole survey.

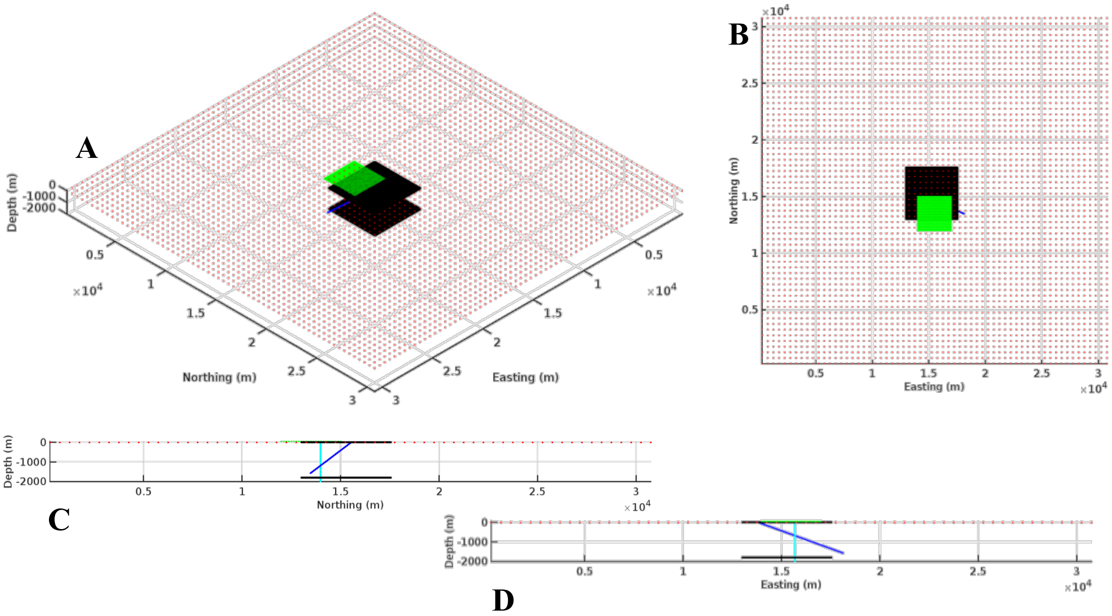

**Figure 50. Synthetic Survey Design**
Synthetic survey design used in this study. (A) map view; (B) perspective view; (C) cross-sectional view looking west; (D) cross-sectional view looking north; black squares delineate top and bottom surfaces of the target volume, which have mass distributions that are derived from an actual rock sample; red dots represent a typical land-based survey of vertical gravity; green dots represent six-component airborne gravity gradiometry survey; cyan and blue dots represent vertical and diagonal borehole gravity surveys. Total volume of interest is approximately 5x5x2 $km^3$.

### *Hypothetical Modeling*

I generate a voxelized volume of the same size as the synthetic volume. Each voxel has an *a priori* density of 2.62 $g/cm^3$, which is the average density of the entire synthetic volume. From the single-density volume, I use SIGMA to calculate the effective gravity for the land and borehole surveys, and effective gravity gradient for the airborne survey. As expected, the calculated results and the synthetic result do not match as they were generated from different mass distributions. I use a constrained inversion that changes the *a priori* density to minimize the misfit between the modeled results to the synthetic observations.

### *Inversion Results*

The output from SIGMA is a $m \times n$ matrix, where $m$ is the number of rows equal to the number of stations used in the computation, and $n$ is the number of columns equal to the number of density bodies delineated by the modeler. I used these results as the input matrix in the inversion defined by Crain (2006), which uses statistical constraints to solve for the unknown parameters in the model. I input the average density of 2.62 g/cm$^3$ for all the elements in the model, and allow the inversion to shift the densities 0.1 g/cm$^3$ per iteration.

The final results show that the inversion was able to reasonably resolve the hypothetical mass distribution (Fig. 51). The inversion appears insensitive to the input parameters, but varied mainly on the station data that I used. Using only the surface data ($g_z$), the resulting model had a fit of 64.7%. The addition of gravity gradiometry data ($g_{xx}$, $g_{xy}$, $g_{xz}$, $g_{yy}$, $g_{yz}$, and $g_{zz}$) to $g_z$ was slightly better at 75.2%. It was not until the addition of borehole data, or vertical observational constraints, that the resulting model correlated to 91.4%. I interpret these observations to confirm that as the orthogonality of the observations increase, the better I can resolve mass distributions within the model.

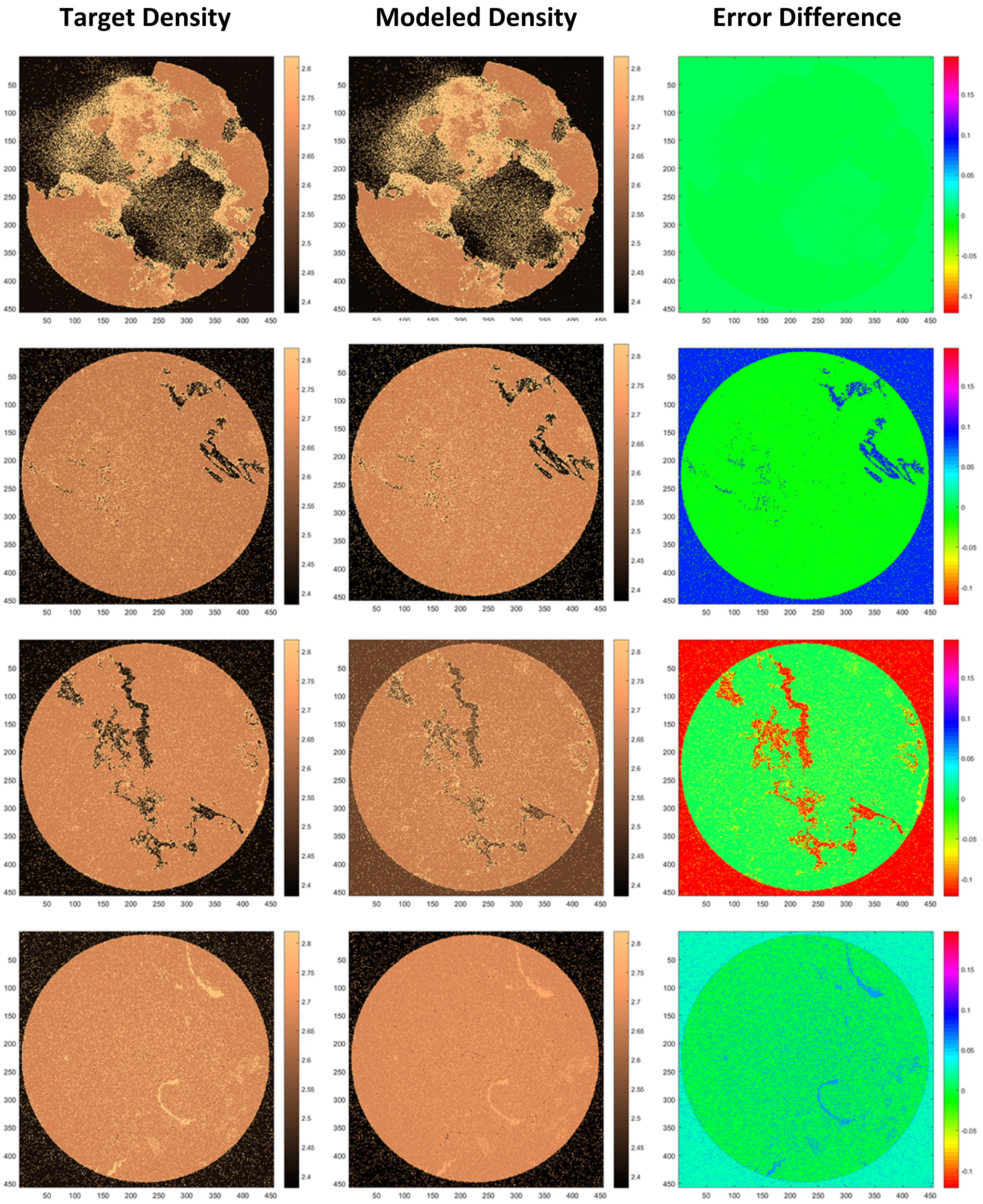

**Figure 51. 2D slices through density volumes**
SIGMA processing and inversion results can delineate subtle density variations, even with less than 0.5 g/cm$^3$ total range in values spread over a 5 km x 5 km x 1.8 km body. Target Density (left) derived from a Haynesville Shale XRCT scan (Elmore *et al.*, 2016). Modeled Density (center) distribution using combined point data described in the text. Residual density (right) = target density – resultant density. The *a priori* density model was isometrically 2.62 g/cm$^3$.

## Conclusions

At its most basic use, SIGMA can quickly compute terrain corrections for the routine computation of the Bouguer Anomaly in traditional gravity workflow. SIGMA cuts processing time by several orders of magnitude depending on the size of the study area and requested resolution. The computation results in minimal error even when compared to analytical solutions, and is significantly faster than competing methods of mass approximation. Such efficiencies would also apply to geodetic modeling, where a lot of effort is devoted to computing topographic reductions.

Piece-wise or modular gravity computations allow model refinement without recalculating static components of the model. As seen in the Osage County modeling, running the entire volume through the forward modeling algorithm was not necessary to reduce the residual between observed FAA and calculated FAA. This is especially efficient when modeling large areas at high resolution.

SIGMA can compute the vertical gravity and gravity gradient at any given point in space, from any 2D profile or 3D volume. This unique ability to model point data is key to periscopic observations in potential fields, which can theoretically produce a more constrained solution. The ability for SIGMA to compute the gravity field at points, combined with an inversion, maximizes the potential of the gravity method in geophysical investigations.

# Dissertation Summary

My dissertation comprises four chapters that investigate earthquakes and faulting processes, from small-scale laboratory experiments to large-scale regional modeling. I successfully simulated $M_W$4-8 earthquakes in rotary shear apparatus, with Earthquake-Like Slip-Events (ELSE) experiments. The ELSE experiment delivers a finite amount of energy to the sample cell, and the sample responds spontaneously, with respect to the amount of delivered energy: (a) the sample slips if the Coulomb Energy Density is sufficient, or (b) the sample does not slip if the Coulomb Energy Density is not sufficient. The 3D tomography of Tangshan, China revealed two modes of basin-sizes: (1) a broad basin that I attribute to the large-scale subsidence in the Bohai Bay, and a relatively smaller-scale (tens of km) basin, which I attribute to local bends and steps of faults underlying Tangshan. The seismicity in Oklahoma from 2010 to 2017 increased rapidly from less than three felt earthquakes per year prior to 2010 to more than two thousand in felt earthquakes in 2014-2017. Chapter 4 covers the pivotal seismic evolution of Oklahoma, and the effort that went in to study the induced seismicity phenomenon. Lastly, is a discussion of a Semi-Infinite Gravity Modeling Algorithm (SIGMA) and its potential to advance gravity modeling that uses gravity observations at the coordinate space in which they are observed. This opens up the possibility to model mass bodies in a periscopic sense and better delineate mass-distributions that may be otherwise ambiguous using traditional gravity modeling methods alone.

# References

Ander, M.E., and Chapin, D.A., 1997, Borehole Gravimetry: A Review: Paper SEG-1997-0531 presented at the 1997 International Exposition and Annual Meeting, Society of Exploration Geophysicists, Dallas, Texas, 2-7 Nov.

Abercrombie, R.E., and Rice, J.R., 2005, Can Observations of Earthquake Scaling Constrain Slip Weakening?: Geophysical Journal International, v. 162, p. 406-424.

Alt, R.C., II, and Zoback, M.D., 2016, In Situ Stress and Active Faulting in Oklahoma: Bulletin of the Seismological Society of America, v. 107, n. 1, p. 216–228, DOI: 10.1785/0120160156.

Andrews, D.J., 2005, Rupture Dynamics with Energy Loss Outside the Slip Zone: Journal of Geophysical Research, v. 110, B01307, 14 pp, DOI: 10.1029/2004JB003191.

Boettcher, M.S., McGarr, A., and Johnston, M., 2009, Extension of Gutenberg-Richter Distribution to MW -1.3, No Lower Limit in Sight, Geophysical Research Letters, v. 36, L10307, DOI: 10.1029/2009GL038080.

Boneh, Y., Chang, J.C., Lockner, D.A., and Reches, Z., 2014, Evolution of Wear and Friction Along Experimental Faults: Pure and Applied Geophysics, v. 171, p. 3125-3141, DOI: 10.1007/s00024-014-0801-3.

Brady, J.L., Wolcott, D.S., and Aiken, C.L.V., 1993, Gravity Methods: Useful Techniques for Reservoir Surveillance: Paper SPE-26095-MS presented at Western Regional Meeting, Society of Petroleum Engineers, Anchorage, Alaska, 26-28 May, DOI: 10.2118/26095-MS.

Bullard, E.C., 1936, Gravity Measurements in East Africa: Philosophical Transactions of the Royal Society, London, v. 235, p. 445–534.

Cardenas, R., and Ceberio, M., 2012, Efficient Geophysical Technique of Vertical Line Elements as a Natural Consequence of General Constraints Techniques: Journal of Uncertain Systems, v. 6, n. 2, p. 86-88.

Chang, J.C., Lockner, D.A., and Reches, Z., 2012, Rapid Acceleration Leads to Rapid Weakening in Earthquake-Like Laboratory Experiments: Science, v. 338, No. 6103, p. 101-105.

Chang, J.C., 2016, Seismic Investigation of South Central Oklahoma: International Federation of Digital Seismograph Networks, DOI: 10.7914/SN/ZP_2016.

Chen, X., Elwood Madden, A.S., and Reches, Z., 2017, *in* Thomas, M.Y., Mitchell, T.M., and Bhat, H.S., eds., Evolution of Fault Properties During Seismic

Rupture: John Wiley & Sons, Inc., Hoboken, New Jersey, p. 133-150, DOI: 10.1002/9781119156895.ch7.

Chen, X., Nakata, N., Pennington, C., Haffener, J., Chang, J.C., He, X., Zhan, Z., Ni, S., and Walter, J.I., 2017, The Pawnee Earthquake as a Result of Interplay Among Injection, Faults and Foreshocks: Scientific Reports, v. 7, DOI: 10.1038/s41598-017-04992-z.

Chen, X., Peng, Z., and Chang, J.C., 2016, Rapid response for Fairview aftershock in Oklahoma: International Federation of Digital Seismograph Networks, DOI: 10.7914/SN/Y7_2016.

Cook, K.L., 1956, Regional Gravity Survey in Northeastern Oklahoma and Southeastern Kansas: Geophysics, v. 21, p. 88-106.Danes, Z.F., 1960, On a Successive Approximation Method for Interpreting Gravity Anomalies: Geophysics, v. 25, n. 6, p. 1215-1228.

Crain, K.D., 2006, Three-Dimensional Gravity Inversion with A Priori and Statistical Constraints [Ph.D. thesis]: El Paso, University of Texas, 64 p.

Crain, K.D., and Keller, G.R., 2013, 3D Gravity Modeling of Osage County, Oklahoma, 3D Geology Interpretation: presented at the 2013 Annual Meeting, Society of Exploration Geophysicists, Houston, Texas, 22-27 Sep.

Crone, A.J., and Luza, K.V., 1990, Style and Timing of Holocene Surface Faulting on the Meers Fault, Southwestern Oklahoma: Geological Society of America Bulletin, v. 102, p. 1-17.

Denison, R. E., 1981, Basement Rocks in Northeastern Oklahoma: Oklahoma Geological Survey Circular 84, p. 1-84.

Darold, A., 2014, 4D Integrated Study Using Geology, Geophysics, Reservoir Modeling & Rock Mechanics to Develop Assessment Models for Potential Induced Seismicity Risk. International Federation of Digital Seismograph Networks, DOI: 10.7914/SN/ZD_2014.

Darold, A.P., and Holland, A.A., 2015, Preliminary Oklahoma Optimal Fault Orientations: Oklahoma Geological Survey Open File Report OF4-2015.

Dart, R.L., 1990, In Situ Stress Analysis of Wellbore Breakouts from Oklahoma and the Texas Panhandle: U.S. Geological Survey Bulletin 1866-Chapter F, 36 pp.

Dieterich, J.H., 1981, *in* Carter, N.L., ed., Mechanical Behavior of Crustal Rocks: American Geophysical Union, Washington, DC, p. 103-120.

Di Toro, G., Han, R., Hirose, T., De Paola, N., Nielsen, S., Mizoguchi, K., Ferri, F., Cocco, M., and Shimamoto, T., 2011, Fault Lubrication During Earthquakes: Nature, v. 471, p. 494-498.

Elmore, R.D., Heij, G.W., and Wickard, A.K., 2016, Paragenesis of Mineralized Fractures and Diagenesis of Prominent North American Shales: The Sedimentary Record, v. 14, no. 4, p. 4-10.

Fang, W., 1979, The 1976 Tangshan Earthquake: Earthquake Information Bulletin (USGS), v. 11, p. 106-109.

Fielding, E.J., Sangha, S.S., Bekaert, D.P.S., Samsonov, S.V., and Chang, J.C., 2017, Surface Deformation of North-Central Oklahoma Before, During, and After the 2016 Mw 5.8 Pawnee Earthquake from SAR Interferometry Time Series: Seismological Research Letters, v. 88, p. 971-982, DOI: 10.1785/0220170010.

Freund, L.B., 1990, Dynamic Fracture Mechanics: Cambridge University Press, Cambridge.

Fukuyama, E., Mikumo, T., and Olsen, K.B., 2003, Estimation of the Critical Slip-Weakening Distance: Theoretical Background: Bulletin of the Seismological Society of America, v. 93, p. 1835-1840.

Goldsby, D.L., and Tullis, T.E., 2011, Flash Heating Leads to Low Frictional Strength of Crustal Rocks at Earthquake Slip Rates: Science, v. 334, p. 216-218.

Grady, D.E., and Kipp, M.E., 1985, Geometric statistics and dynamic fragmentation: Journal of Applied Physics, v. 58, p. 1210-1222.

Grüninger, W., 1990, Zur Topographisch-Isostatischen Reduktion der Schwere [Ph.D. thesis]: University of Karlsruhe, Germany.

Guatteri, M., and Spudich, P., 2000, What Can Strong-Motion Data Tell us About Slip-Weakening Fault-Friction Laws?: Bulletin of the Seismological Society of America, v. 90, p. 98-116.

Hammer, S., 1974, Approximation in Gravity Interpretation Calculations: Geophysics, v. 39, n. 2, p. 205-222.

Han, R., Hirose, T., and Shimamoto, T., 2010, Strong Velocity Weakening and Powder Lubrication of Simulated Carbonate Faults at Seismic Slip Rates: Journal of Geophysical Research, v. 116, B03412, DOI: 10.1029/2008JB006136.

Hayford, J.F., and Bowie, W., 1912, The Effect of Topography and Isostatic Compensation upon the Intensity of Gravity: U.S. Coast and Geodetic Survey Special Publication No. 10, Washington, DC.

Heard, H.C., 1963, Effect of Large Changes in Strain Rate in the Experimental Deformation of Yule Marble: Journal of Geology, v. 71, p. 162-195.

Heaton, T.H., 1990, Evidence for and Implications of Self-Healing Pulses of Slip in Earthquake Rupture: Physics of the Earth and Planetary Interiors, v. 64, p. 1-20.

Heck, B., and Seitz, K., 2007, A Comparison of the Tesseroid, Prism and Pointmass Approaches for Mass Reductions in Gravity Field Modelling: Journal of Geodesy, v. 81, n. 2, p.121-136, DOI: 10.1007/s00190-006-0094-0.

Heiland, C.A., 1940, Geophysical exploration: New York, Prentice-Hall, Inc., p. 152.Heshmat, H., 1995, The Quasi-Hydrodynamic Mechanism of Powder Lubrication – Part III: On Theory and Rheology of Triboparticulates: Tribology Transactions, v. 38, p. 269–276.

Hole, J.A., 1992, Nonlinear High-Resolution Three-Dimensional Seismic Travel Time Tomography: Journal of Geophysical Research, v. 97, p. 6553-6562, DOI: 10.1029/92JB00235.

Holland, A.A., 2013, Earthquakes Triggered by Hydraulic Fracturing in South-Central Oklahoma: Bulletin of the Seismological Society of America, v. 103, n. 3, p. 1784–1792, DOI: 10.1785/0120120109.

Holland, A., Keller, G.R., Darold, A., Murray, K., and Holloway, S., 2014, Multidisciplinary Approach to Identify and Mitigate the Hazard from Induced Seismicity in Oklahoma: presented at 2014 Fall Meeting, American Geophysical Union, San Francisco, California, 15-19 Dec.

Huang, H., and Feng, R., 2006, Dynamic Tribological Response of SiC Fracture Surfaces: Mechanics of Materials, v. 38, p. 186-202.

Ide, S., and Takeo, M., 1997, Determination of Constitutive Relations of Fault Slip Based on Seismic Wave Analysis: Journal of Geophysical Research, v. 102, p. 27379- 27391.

Kanamori, H., and Rivera, L., 2006, *in* Abercrombie, R.E., McGarr, A., Di Toro, G., and Kanamori, H., eds., Earthquakes: Radiated Energy and the Physics of Faulting: American Geophysical Union, Washington, DC, p. 3-13.

Keranen, K.M., Savage, H.M., Abers, G.A., and Cochran, E.S., 2013, Potentially Induced Earthquakes in Oklahoma, USA: Links Between Wastewater Injection and the 2011 Mw 5.7 Earthquake Sequence: Geology, v. 41, p. 699-702, DOI: 10.1130/G34045.1

Kissling, E., Ellsworth, W.L., Eberhart-Phillips, D., and Kradolfer, U., 1994, Initial Reference Models in Local Earthquake Tomography: Journal of Geophysical Research, v. 99, p. 19635-19646.

Lawson, J.E., Jr., 1978, A Preliminary Duration Magnitude Scale for Local and Regional Earthquakes Recorded at Oklahoma Seismograph Stations: Oklahoma Geophysical Observatory Open-File Report, 14 pp.

Lee, W.H.K., Bennet, R.E., and Meaghu, K.L., 1972. A Method of Estimating Magnitude of Local Earthquakes from Signal Duration: U.S. Geological Survey Open File Report, 28 pp.

Leveque, J-.J., Rivera, L., and Wittlinger, G., 1993, On the Use of the Checker-Board Test to Assess the Resolution of Tomographic Inversions: Geophysical Journal International, v. 115, p. 313-318.

Li, S., Mooney, W, and Fan, J., 2006, Crustal Structure of Mainland China from Deep Seismic Sounding Data: Tectonophysics, v. 420, p. 239-252.

Liao, Z., Chang, J.C., and Reches, Z., 2014, Fault Strength Evolution During High Velocity Friction Experiments with Slip-Pulse and Constant-Velocity Loading: Earth and Planetary Science Letters, v. 406, p. 93-101, DOI: 10.1016/j.epsl.2014.09.010.

Lockner, D.A., and Okubo, P.G., 1983, Measurements of Frictional Heating in Granite: Journal of Geophysical Research, v. 88, p. 4313-4320.

Luetgert, J.H., 1992, MacRay: Interactive Two-Dimensional Seismic Raytracing for the Macintosh: U.S. Geological Survey Open-File Report 92-356.

Marsh, S.M., and Holland, A.A., 2016, Comprehensive Fault Database and Interpretive Fault Map of Oklahoma: Oklahoma Geological Survey Open File Report OF2-2016, 15 pp.

McGarr, A., Bekins, B., Burkardt, N., Dewey, J., Earle, P., Ellsworth, W. Ge, S., Hickman, S., Holland, A., Majer, E., Rubenstein, J., and Sheehan, A., 2015, Coping with Earthquakes Induced by Fluid Injection: Science, v. 347, p. 830-831, DOI: 10.1126/science.aaa0494.

Nagy, D., 1966, The Gravitational Attraction of a Right Rectangular Prism: Geophysics, v. 31, n. 2, p. 362-371.

Nagy, D., Papp, G., and Benedek, J., 2000, The Gravitational Potential and its Derivatives for the Prism: Journal of Geodesy, v. 74, n.7-8, p. 552-560, DOI: 10.1007/s001900000116.

Nagy, D., Papp, G., and Benedek, J., 2002, Corrections to “The Gravitational Potential and its Derivatives for the Prism”: Journal of Geodesy, v. 76, n. 8, p. 475, DOI: 10.1007/s00190-002-0264-7.

Nakata, N., 2016, Acquisition of Aftershock Sequence of the 2016 M5.6 Sooner Lake Earthquake: International Federation of Digital Seismograph Networks, DOI: 10.7914/SN/Y7_2016.

Natural Gas Intelligence, 2017, http://www.naturalgasintel.com/misslimeinfo (accessed December 2017).

Niemeijer, A., Di Toro, G., Nielsen, S., and Di Felice, F., 2010, Frictional Melting of Gabbro Under Extreme Experimental Conditions of Normal Stress, Acceleration, and Sliding Velocity: Journal of Geophysical Research, v. 116, B07404, DOI: 10.1029/2010JB008181.

Ohnaka, M., and Yamashita, T., 1989, A Cohesive Zone Model for Dynamic Shear Faulting Based on Experimentally Inferred Constitutive Relation and Strong Motion Source Parameters: Journal of Geophysical Research, v. 94, p. 4089-4104.

Oklahoma Geological Survey, 1978, Oklahoma Seismic Network: International Federation of Digital Seismograph Networks, DOI: 10.7914/SN/OK.

Okubo, P.G., and Dieterich, J.H., 1981, Fracture Energy of Stick-Slip Events in a Large Scale Biaxial Experiment: Geophysical Research Letters, v. 8, p. 887-890.

Olgaard, D.L., and Brace, W.F., 1983, The Microstructure of Gouge from a Mining-Induced Seismic Shear Zone: International Journal of Rock Mechanics and Mining Science, v. 20, p. 11–19.

Ottemoller, L., Voss, P., and Havskov, J., 2017, SEISAN Earthquake Analysis Software: http://seis.geus.net/software/seisan/seisan.html (accessed December 2017).

Petersen, M.D., Moschetti, M.P., Powers, P.M., Mueller, C.S., Haller, K.H., Frankel, A.D., Zeng, Y, Rezaeian, S., Harmsen, S.C., Boyd, O.S., Field, E.H., Chen, R., Luco, N., Wheeler, R.L., Williams, R.A., Olsen, A.H., and Rukstales, K.S., 2015, Seismic-Hazard Maps for the Conterminous United States, 2014: U.S. Geological Survey Scientific Investigations Map 3325, 6 sheets, scale 1:7,000,000, DOI: 10.3133/sim3325.

Petersen, M.D., Mueller, C.S., Moschetti, M.P., Hoover, S.M., Llenos, A.L., Ellsworth, W.L., Michael, A.J., Rubinstein, J.L., McGarr, A.F., and Rukstales, K.S., 2016, 2016 One-Year Seismic Hazard Forecast for the Central and Eastern United States from Induced and Natural Earthquakes: U.S. Geological Survey Open-File Report 2016–1035, 52 pp., DOI: 10.3133/ofr20161035.

Petersen, M.D., Mueller, C.S., Moschetti, M.P., Hoover, S.M., Shumway, A.M., McNamara, D.E., Williams, R.A., Llenos, A.L., Ellsworth, W.L., Michael, A.J., Rubinstein, J.L., McGarr, A.F., and Rukstales, K.S., 2017, One-Year Seismic Hazard Forecast for the Central and Eastern United States from Induced and Natural Earthquakes: Seismological Research Letters, v. 88, n. 3, p. 772-783, DOI: 10.1785/0220170005.

Reches, Z., and Dewers, T.A., 2005, Gouge Formation by Dynamic Pulverization During Earthquake Rupture: Earth and Planetary Science Letters, v. 235, p. 361-374.

Reches, Z., and Lockner, D.A., 2010, Fault Weakening and Earthquake Instability by Powder Lubrication: Nature, v. 467, p. 452-455.

Rodriguez, E., Morris, C.S., Belz, J.E., Chapin, E.C., Martin, J.M., Daffer, W., and Hensley, S., 2005, An Assessment of the SRTM Topographic Products: Technical Report JPL D-31639, Jet Propulsion Laboratory, Pasadena, 143 pp.

Saltus, W.R., and Blakely, R.J., 2011, Unique Geologic Insights From "Non-Unique" Gravity and Magnetic Interpretation: GSA Today, v. 21, n. 12, p. 4-11.

Sammis, C.G., Lockner, D. A., and Reches, Z., 2011, The Role of Adsorbed Water on the Friction of a Layer of Submicron Particles: Pure and Applied Geophysics, v. 168, p. 2325-2334.

Segall, P., 1985, Stress and Subsidence Resulting from Subsurface Fluid Withdrawal in the Epicentral Region of the 1983 Coalinga Earthquake: Journal of Geophysical Research, v. 90, p. 6801-6816, DOI: 10.1029/JB090iB08p06801.

Shale Experts, 2017, http://www.shaleexperts.com/plays/stack-scoop/ (accessed 2017).

Shirzaei, M., Ellsworth, W.L., Tiampo, K.F., Gonzales, P.J., and Manga, M., 2016, Surface Uplift and Time-Dependent Seismic Hazard due to Fluid Injection in Eastern Texas: Science, v. 353, p.1416-1419, DOI: 10.1126/science.aag0262.

Smith, N.L., 1950, The Case for Gravity Data from Boreholes: Geophysics, v. 15, n. 4, p. 605-636, DOI: 10.1190/1.1437623.

The Play, 2009, https://www.chk.com/documents/media/publications/the-play-2009-2.pdf (accessed 2017).

Tinti, E., Spudich, P., and Cocco, M., 2005, Earthquake Fracture Energy Inferred from Kinematic Rupture Models on Extended Faults: Journal of Geophysical Research, v. 110, B12303, DOI: 10.1029/2005JB003644.

Vidale, J.E., 1990, Finite-Difference Calculation of Traveltimes in Three Dimensions: Geophysics, v. 55, p. 521-526.

Waldhauser, F., and Ellsworth, W.L., 2000, A Double-Difference Earthquake Location Algorithm: Method and Application to the Northern Hayward Fault, California: Bulletin of the Seismological Society of America, v. 90, p. 1353-1368.

Walsh, F.R., and Zoback, M.D., 2015, Oklahoma's Recent Earthquakes and Saltwater Disposal: Science Advances, v. 1, n. 5, 9 pp, DOI: 10.1126/sciadv.1500195.

Walter, J.I., Chang, J.C., and Dotray, P.J., 2017, Foreshock Seismicity Suggests Gradual Stress Increase in the Months Prior to the 3 September 2016 Mw 5.8 Pawnee Earthquake: Seismological Research Letters, v. 88, p. 1032-1039, DOI: 10.1785/0220170007.

Wells, D.L., and Coppersmith, K.J., 1994, New Empirical Relationships Among Magnitude, Rupture Length, Rupture Width, Rupture Area, and Surface Displacement: Bulletin of the Seismological Society of America, v. 84, p. 974-1002.

Wild-Pfeifer, F., 2008, A Comparison of Different Mass Element for Use in Gravity Gradiometry: Journal of Geodesy, v. 82, n. 10, p. 637-653, DOI: 10.1007/s00190-008-0219-8.

Wilson, B., Dewers, T.A., Reches, Z., and Brune, J., 2005, Texture and Energetics of Gouge Powder from Earthquake Rupture Zones: Nature, v. 434, p. 749-752.

Wornyoh, E.Y.A., Jasti, V.K., and Higgs III, C.F., 2007, A Review of Dry Particulate Lubrication: Powder and Granular Materials: Journal of Tribology, v. 129, p. 438-449.

Yabe, Y., Philipp, J., Nakatani, M., Morema, G., Naoi, M., Kawakata, H., Igarashi, T., Dresen, G., Ogasawara, H., and JAGUARS, 2009, Observation of Numerous Aftershocks of an MW 1.9 Earthquake with an AE Network Installed in a Deep Gold Mine in South Africa: Earth, Planets and Space, v. 61, p. e49–e52.

Yeck, W.L., Hayes, G.P., McNamara, D.E., Rubinstein, J.L., Barnhart, W.D., Earle, P.S., and Benz, H.M., 2017, Oklahoma Experiences Largest Earthquake During Ongoing Regional Wastewater Injection Hazard Mitigation Efforts: Geophysical Research Letters, v. 44, p. 711-717, DOI: 10.1002/2016GL071685.

Yuan, F., and Prakash, V., 2008, Slip Weakening in Rocks and Analog Materials at Co-Seismic Slip Rates: Journal of the Mechanics and Physics of Solids, v. 56, p. 542-560.

Zoback, M.D., and Zoback., M.L., 1991, Tectonic Stress Field of North America and Relative Plate Motions, *in* D.B. Slemmons, E.R. Engdahl, M.D. Zoback, and M.D. Blackwell, eds., Neotectonics of North America: Boulder, Colorado, Geological Society of America, p. 339-366.

Zoback, M.L., 1992, Stress Field Constraints on Intraplate Seismicity in Eastern North America: Journal of Geophysical Research, v. 97, n. B8, p. 11,761-11,782.

# Appendix A: Collaborative Contributions in Journal Publications

Along with the main projects discussed in my dissertation, I also contributed efforts in other projects by other researchers. Selected contributions are presented here in the form of abstracts with listed contributions for peer-reviewed journals, where I am not the first author, and a reference list for presented abstracts in scientific meetings.

## *Induced Seismicity in Central Oklahoma*

Chen, X., Haffener, J., Goebel, T., Meng, X., Peng, Z., and Chang, J.C., submitted to Journal of Geophysical Research, Temporal correlation between seismic moment and injection volume for an induced earthquake sequence in central Oklahoma.

### *Abstract*

The rapidly increased earthquake rate in the central United States has been linked with wastewater injection. While the overall understanding appears clear at large scales, the interaction between injection and faulting at smaller scales within individual sequences is still not clear. For an earthquake sequence in central Oklahoma, we conduct finer scale analysis of the spatiotemporal evolution of seismicity, and find temporal correlation be-tween earthquake rate, seismic moment, and injection rates from wells in close proximity. The fault started with low seismicity rate, likely from far-field pressure propagation from disposal wells located within 15 km from the sequence. The injection of a well in close proximity led to rapid activation of the entire fault zone as evidenced by low b-value and expansion of rupture area following diffusive migration. Its injection volume multiplied by shear modulus agrees well with the cumulative seismic moment of the sequence, suggesting that the total moment release is strongly influenced by fluid volume. The maximum seismic moment gradually increases with time, culminating in

the largest earthquake (M3.8) towards the end of the sequence. The scaling factor between maximum seismic moment and injection volume is about one order of magnitude lower than the shear modulus, suggesting the maximum magnitude is likely bounded by the size of the asperity, which is consistent with the truncated Gutenberg-Richter distribution observed from matched-filter detected catalog. Overall, the detailed observations suggest that it is possible to resolve relationships between individual sequences and wells.

### *Contribution*

My contributions include data acquisition, discussions with the lead author, and manuscript editing.

## *Fluid Injection, Earthquake, and Fault Interactions in Pawnee, Oklahoma*

Chen, X., Nakata, N., Pennington, C., Haffener, J., Chang, J.C., He, X., Zhan, Z., Ni, S., and Walter, J.I., 2017, The Pawnee Earthquake as a Result of Interplay Among Injection, Faults and Foreshocks: Scientific Reports, v. 7, DOI: 10.1038/s41598-017-04992-z.

### *Abstract*

The Pawnee M5.8 earthquake is the largest event in Oklahoma instrument recorded history. It occurred near the edge of active seismic zones, similar to other M5+ earthquakes since 2011. It ruptured a previously unmapped fault and triggered aftershocks along a complex conjugate fault system. With a high-resolution earthquake catalog, we observe propagating foreshocks leading to the mainshock within 0.5 km distance, suggesting existence of precursory aseismic slip. At approximately 100 days before the mainshock, two $M \geq 3.5$ earthquakes occurred along a mapped fault that is

conjugate to the mainshock fault. At about 40 days before, two earthquakes clusters started, with one M3 earthquake occurred two days before the mainshock. The three $M \geq 3$ foreshocks all produced positive Coulomb stress at the mainshock hypocenter. These foreshock activities within the conjugate fault system are near-instantaneously responding to variations in injection rates at 95% confidence. The short time delay between injection and seismicity differs from both the hypothetical expected time scale of diffusion process and the long time delay observed in this region prior to 2016, suggesting a possible role of elastic stress transfer and critical stress state of the fault. Our results suggest that the Pawnee earthquake is a result of interplay among injection, tectonic faults, and foreshocks.

### *Contribution*

My major contribution was a cross-section across the Pawnee area that comprised well information, geology, and seismicity data. The cross-section shows the sedimentary unit thicknesses and depth to basement, and several well locations with lithologic boundaries and interpreted sonic logs. Other contributions include providing data, discussions with the other authors, and manuscript editing.

### *Potentially Induced Earthquakes are Indistinguishable from Tectonic Earthquakes*

Walter, J.I., Chang, J.C., and Dotray, P.J., 2017, Foreshock seismicity suggests gradual stress increase in the months prior to the 3 September 2016 Mw 5.8 Pawnee earthquake: Seismological Research Letters, v. 88, p. 1032-1039, DOI: 10.1785/0220170007.

### *Abstract*

The 3 September 2016 MW 5.8 Pawnee earthquake was the largest earthquake in Oklahoma history. To determine the relationship with nearby seismic activity and whether there were any precursory foreshocks to the event, we analyze a dataset comprising regional seismometers throughout Oklahoma, including the Oklahoma Geological Survey statewide network. We use a matched-filter technique to identify potential missing earthquakes before and after the mainshock. This technique utilizes cataloged waveforms as templates that, when correlated against continuous waveforms, are able to identify repeating or nearby earthquakes. As shown in other studies, the aftershocks roughly fall along an east-southeast-trending linear belt that illuminates a previously unknown fault. We utilize the augmented seismicity catalog to draw two main conclusions. From standard statistical seismological methods, we deduce that the b-value decreased prior to the Pawnee mainshock; previous work suggests that b-value and differential stress are anticorrelated. The b-value result suggests the differential stress along the fault that eventually ruptured was gradually increasing in the few months leading up to the mainshock. During the aftershock period, we infer an Omori-Utsu p-value close to 1, typical for most tectonic events. Although the prolonged seismicity in the months leading up to the event may be a hallmark of induced earthquakes and may help decipher induced earthquakes from natural earthquakes, the rate of aftershocks is indistinguishable from natural tectonic earthquakes though deficient in larger aftershocks.

### *Contribution*

My contributions include data acquisition, discussions with the lead author, and manuscript editing.

### *Slip-Model of the Pawnee M5.8 Earthquake from Geodetic Observations*

Fielding, E.J., Sangha, S.S., Bekaert, D.P.S., Samsonov, S.V., and Chang, J.C., 2017, Surface deformation of north-central Oklahoma before, during, and after the 2016 Mw 5.8 Pawnee Earthquake from SAR interferometry time series: Seismological Research Letters, v. 88, p. 971-982, DOI: 10.1785/0220170010.

### ***Abstract***

The 3 September 2016 MW 5.8 Pawnee earthquake shook a large area of north-central Oklahoma and was the largest instrumentally recorded earthquake in the state. We processed Synthetic Aperture Radar (SAR) from the Copernicus Sentinel-1A and Sentinel-1B and Canadian RADARSAT-2 satellites with interferometric SAR analysis for the area of north-central Oklahoma that surrounds Pawnee. The interferograms do not show phase discontinuities that would indicate surface ruptures during the earthquake. Individual interferograms have substantial atmospheric noise caused by variations in radar propagation delays due to tropospheric water vapor, so we performed a time-series analysis of the Sentinel-1 stack to obtain a more accurate estimate of the ground deformation in the coseismic time interval and the time variation of deformation before and after the earthquake. The time-series fit for a step function at the time of the Pawnee shows about 3 cm peak-to-peak amplitude of the coseismic surface deformation in the radar line of sight with a spatial pattern that is consistent with fault slip on a plane trending east-southeast. This fault, which we call the Sooner Lake fault, is parallel to the west-northwest nodal plane of the U.S. Geological Survey National Earthquake Information Center moment tensor solution. We model the fault plane by fitting hypoDD-relocated aftershocks aligned in the same trend. Our preferred slip model on

this assumed fault plane, allowing only strike-slip motion, has no slip shallower than 2.3 km depth, an area of moderate slip extending 7 km along strike between 2.3 and 4.5 km depth (which could be due to aftershocks and afterslip), and larger slip between 4.5 and 14 km depth extending about 12 km along strike. The large slip below the 4.5 km depth of our relocated hypocenter indicates that the coseismic rupture propagated down-dip. The time-series results do not show significant deformation before or after the earthquake above the high atmospheric noise level within about 40 km of the earthquake rupture.

### ***Contribution***

My major contributions were writing the seismicity section, creating the seismicity maps, acquiring and processing data concerning the 3 September 2016 Pawnee M5.8 earthquake, and discussing the slip propagation of the main shock. I provided fault locations, raw location data, as well as the double difference relocations from the HypoDD algorithm (Waldhauser, 2001). Our colloquial discussions on fault-slip propagation gave insight to a plausible litmus test in delineating between an anthropogenic or tectonic earthquakes.

### *Earthquake Propagation from Slip-Pulse Models*

Liao, Z., Chang, J.C., and Reches, Z., 2014, Fault strength evolution during high velocity friction experiments with slip-pulse and constant-velocity loading: Earth and Planetary Science Letters, v. 406, p. 93-101, DOI: 10.1016/j.epsl.2014.09.010.

### ***Abstract***

Seismic analyses show that slip during large earthquakes evolves in a slip-pulse mode that is characterized by abrupt, intense acceleration followed by moderate deceleration.

We experimentally analyze the friction evolution under slip-pulse proxy of a large earthquake, and compare it with the evolution at loading modes of constant-velocity and changing-velocity. The experiments were conducted on room-dry, solid granite samples at slip-velocities of 0.0006–1m/s, and normal stress of 1–11.5MPa. The analysis demonstrates that (1) the strength evolution and constitutive parameters of the granite fault strongly depend on the loading mode, and (2) the slip-pulse mode is energy efficient relatively to the constant-velocity mode as manifested by faster, more intense weakening and 50–90% lower energy dissipation. The results suggest that the frictional strength determined in slip-pulse experiments, is more relevant to simulations of earthquake rupture than frictional strength determined in constant-velocity experiments. Further, for a finite amount of crustal elastic energy, the efficiency of slip-pulse would amplify earthquake instability.

#### ***Contribution***

My contributions include data acquisition, discussions with the co-authors, and manuscript editing. I wrote the data acquisition and processing software for these experiments.

### *Fault-Surface Evolution with Respect to Fault-Wear*

Boneh, Y., Chang, J.C., Lockner, D.A., and Reches, Z., 2014, Evolution of wear and friction along experimental faults: Pure and Applied Geophysics, v. 171, p. 3125-3141, DOI: 10.1007/s00024-014-0801-3.

#### ***Abstract***

We investigate the evolution of wear and friction along experimental faults composed of solid rock blocks. This evolution is analyzed through shear experiments along five

rock types, and the experiments were conducted in a rotary apparatus at slip velocities of 0.002–0.97 m/s, slip distances from a few millimeters to tens of meters, and normal stress of 0.25–6.9 MPa. The wear and friction measurements and fault surface observations revealed three evolution phases: A) An initial stage (slip distances <50 mm) of wear by failure of isolated asperities associated with roughening of the fault surface; B) a running-in stage of slip distances of 1–3 m with intense wear-rate, failure of many asperities, and simultaneous reduction of the friction coefficient and wear rate; and C) a steady-state stage that initiates when the fault surface is covered by a gouge layer, and during which both wear-rate and friction coefficient maintain quasi-constant, low levels. While these evolution stages are clearly recognizable for experimental faults made from bare rock blocks, our analysis suggests that natural faults ‘‘bypass’’ the first two stages and slip at gouge-controlled steady-state conditions.

### ***Contribution***

My contributions include data acquisition, discussions with the co-authors, and manuscript editing. I wrote the data acquisition and processing software for these experiments.